Many-Electron Effects in EXAFS

A thesis submitted for the degree of

Doctor of Philosophy

at the University of Leicester

by

Mervyn Roy

Department of Physics and Astronomy

University of Leicester

August 1999

ProQuest LLC
789 East Eisenhower Parkway
P.O. Box 1346
Ann Arbor, MI 48106-1346

Many-Electron Effects in EXAFS

by

Mervyn Roy

Abstract

Extended X-ray absorption fine structure (EXAFS) spectroscopy is an experimental technique useful in the study of non-crystalline materials. EXAFS is analysed by comparing experimental to theoretical spectra. Many-electron effects in EXAFS are important, however, EXAFS theory has been developed using a single electron formalism with many-body effects included via empirical factors. Multiple electron excitations reduce the EXAFS amplitude and hence affect the determination of coordination numbers. At present, intrinsic amplitude reduction effects are modelled by a constant factor whilst extrinsic effects are modelled using an imaginary scattering potential or mean free path term.

This thesis is concerned with the many electron effects in EXAFS. Expressions are developed with which the EXAFS amplitude may be studied independently in the presence of a complex scattering potential. The Hedin-Lundqvist [9] potential, which is most commonly used in EXAFS analysis, is found to overestimate the extrinsic losses but fortuitously gives good agreement to the total losses to the EXAFS. It is concluded that an intrinsic reduction factor should not be used when data fitting with this potential. The Beni, Lee and Platzman [17] correlation potential is also investigated and found to be unsuitable for EXAFS calculations.

The intrinsic amplitude reduction factor is calculated in the high energy limit for all elements and found to give good agreement with experiment. Calculations with both tight binding and atomic initial state wavefunctions show that chemical effects are unimportant when determining the intrinsic amplitude reduction factor.

Time-dependent perturbation theory and a model form for the core hole - photoelectron system are used to calculate the multiple electron excitations following a photoabsorption. Screened and unscreened forms of the potential are investigated. The results agree well with experiment and may be used to approximate the amplitude losses to the EXAFS without the need for *ad hoc* parameters or complex scattering potentials.

Contents

List of Figures

Acknowledgements

I would like to express my thanks to the members of the theory group at Leicester for making my time here so enjoyable, and to my family for their support throughout my education. Special thanks are due to Doctor Steve Gurman for his excellent supervision and guidance throughout the course of this work.

Chapter 1

Introduction

Over the past century, many methods have been developed to enable us to probe the structure of condensed matter on a microscopic scale. One such method is X-ray absorption spectroscopy. In this technique the X-ray absorption coefficient is measured as a function of X-ray energy. Immediately above an X-ray absorption edge and extending up to a few thousand volts beyond the edge, fine structure is observed in the X-ray absorption coefficient. This extended X-ray absorption fine structure, or EXAFS, can provide information on atomic arrangements, bond lengths and coordination numbers in much the same way as techniques such as X-ray diffraction, LEED and RHEED.

Although EXAFS was first observed in the early 1930's by Kronig [1], it was not until the seminal work of Sayers, Stern and Lytle in 1971 that the fine structure was shown to contain useful structural information [2]. In the intervening 50 years the phenomenon had largely been ignored due to two major problems. First, because there was a distinct lack of agreement between theory and experiment and second, because of the sheer difficulty involved in performing EXAFS experiments. With the low intensity X-ray sources available at the time EXAFS experiments could take days to complete. This, however, was to change with the advent of the synchrotron. These high flux, continuous energy X-ray

sources cut the time needed for the collection of an EXAFS data set to mere minutes enabling EXAFS data to be taken quickly and plentifully.

In addition to the advances in experiment, the early 1970's saw a corresponding improvement in the theory. First, in 1974, Stern [3] produced a semi-phenomenological expression for the EXAFS which adequately described the fine structure and showed it could be used to obtain structural information. Then, in 1975 Lee and Pendry [4] fully described the EXAFS in terms of spherical electron waves. Since this time EXAFS has been used to investigate the structure of numerous novel compounds, most notably in the fields of biochemistry and catalysis.

EXAFS is caused by the backscattering from surrounding atoms of the photoelectron emitted by an absorbing atom following the irradiation of a sample by an X-ray beam. Measurement of this fine structure can provide information on atomic species, arrangements, and bonding mechanisms. Although the amount of information obtained from the absorption fine structure may be small compared to, for example, a typical X-ray diffraction experiment, EXAFS does have some advantages over such conventional methods. As atoms absorb X-rays at characteristic energies, EXAFS can be used to probe selectively the structure around a particular atomic site. Because of its chemical specificity, the EXAFS technique is ideally suited to the study of materials where the atoms of interest form only a small proportion of the sample. This is frequently the case in dilute organic samples, the obvious example being the metalloproteins. EXAFS does not depend on any long range order in the sample. It is a local effect, and as such, can be extremely useful in the study of amorphous materials where other structural techniques are not readily applicable.

The theory of EXAFS is based on the interaction between the X-ray photon and the electrons in the sample. Unfortunately, because of the strong electron-electron

interaction, this is necessarily a many-body theory and thus can become very complicated. To date, it has been developed largely in a one electron formalism with many-body effects described by semi-empirical modifying parameters and effective scattering potentials. It is with the many-body effects that this thesis is mainly concerned.

Throughout this thesis we use atomic units, $\hbar = m = e = 1$, with energy measured in Hartrees ($\approx 27.21eV$) and r measured in Bohr radii ($\approx 0.529\mathring{A}$). This is purely for convenience and to make the notation less complex. In the presentation of the data, however, we have sometimes used other units, for example electron volts, where we felt it would aid the readers understanding.

1.1 The X-ray Absorption Coefficient

The simplest EXAFS experiments are performed in transmission mode. A sample is illuminated by a monochromated X-ray beam and the difference in intensity between the incident and transmitted X-ray beam is measured as a function of energy.

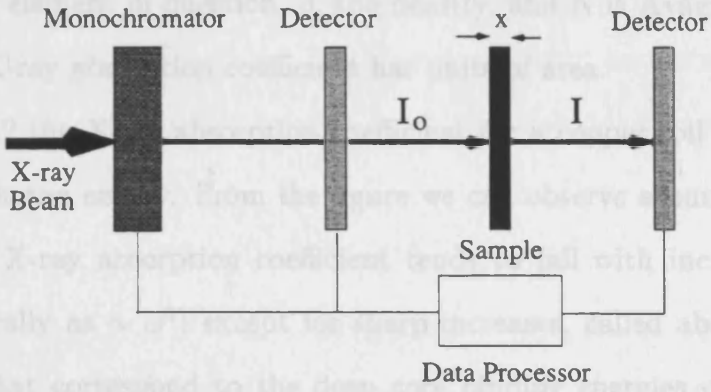

Figure 1.1: Schematic view of the experimental arrangement of a typical EXAFS experiment.

The linear X-ray absorption coefficient is defined in terms of the transmitted (I) and incident intensities (I_o) by, $\mu_{lin}(\omega) = log(I_o/I)/x$, for a homogeneous

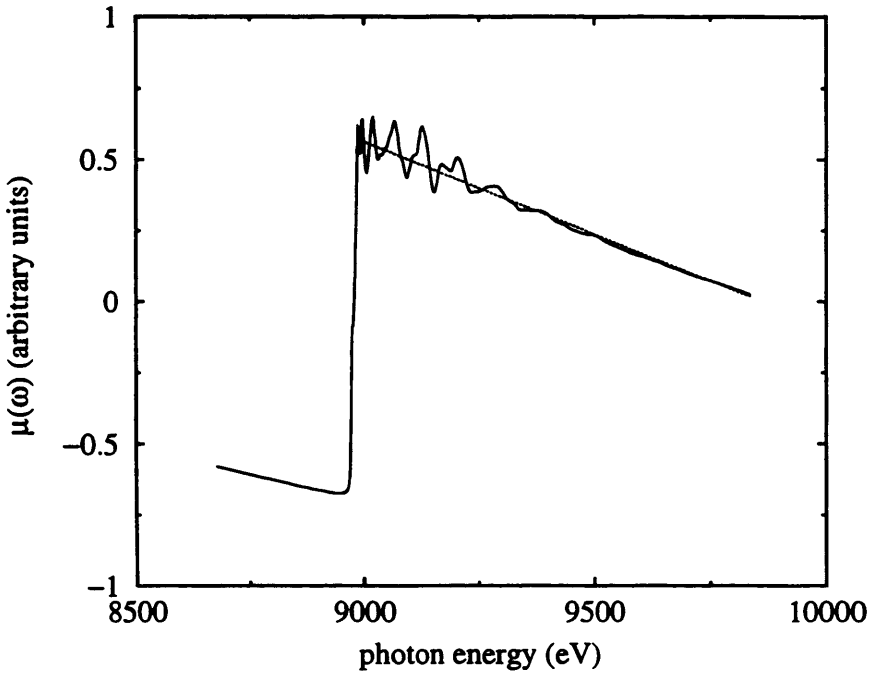

Figure 1.2: The X-ray absorption coefficient for copper. The solid line gives the experimentally measured X-ray absorption, the dotted line shows the smooth atomic absorption factor, μ_o.

sample of thickness, x. It is usually the atomic X-ray absorption coefficient that is considered. This is related to μ_{lin} by, $\mu(\omega) = M\mu_{lin}/(\rho N)$. M is the atomic weight of the element in question, ρ, the density, and N is Avagadro's number. The atomic X-ray absorption coefficient has units of area.

In figure 1.2 the X-ray absorption coefficient for a copper foil is plotted as a function of photon energy. From the figure we can observe a number of general trends. The X-ray absorption coefficient tends to fall with increasing photon energy (generally as $\sim \omega^3$) except for sharp increases, called absorption edges, at energies that correspond to the deep core binding energies of the elements that make up the sample. Past the edge, up to about a thousand eV above the core binding energies we can see oscillations superimposed on the general smooth decrease of the X-ray absorption coefficient. These oscillations are the EXAFS. They are present wherever the absorbing atom is surrounded by a number of

other atoms, for example in molecules or condensed matter.

The X-ray absorption coefficient is usually written as the sum of two contributions, a part varying smoothly with energy corresponding physically to the absorption coefficient of an isolated atom and an additional part containing all of the fine structure,

$$\mu(\omega) = \mu_o(\omega)\,[1 + \chi(\omega)]\,, \tag{1.1}$$

where μ_o is the X-ray absorption coefficient of an isolated atom and χ is the EXAFS function which contains the information on the fine structure.

In the energy range probed by EXAFS experiments, typically 1-40keV, the X-ray attenuation processes are dominated by photoelectric absorption. A photon of energy ω is absorbed by an atom giving up its energy to a single electron from a deep core orbital. Away from the absorption edge the electron is excited into a continuum state of energy, $\omega_k = \omega - |\omega_o| = \frac{1}{2}k^2 + E_f$, where ω_o is the binding energy of the deep core orbital, k is the photoelectron wavenumber and E_f is the thermodynamic Fermi energy of the material. Of course, multiple electron excitations are also possible. These, so called, shake-up and shake-off processes will be discussed further in section 1.3.1. For the moment, assuming only a single electron is excited, we may write the X-ray absorption coefficient from Fermi's golden rule as,

$$\mu(\omega) \sim |\langle\psi_{\mathbf{k}}(\mathbf{r})|\boldsymbol{\epsilon}\cdot\mathbf{r}|\phi_o(\mathbf{r})\rangle|^2\rho(\omega_k). \tag{1.2}$$

$\rho(\omega_k)$ is the density of final states. Typically this is approximated as the smoothly varying free electron density of states. In equation (1.2) $(\boldsymbol{\epsilon}\cdot\mathbf{r})$ describes the effect of the electric field of the X-ray photon within the dipole approximation. In the dipole approximation the X-ray wavelength is assumed to be small compared to the radius of the initial state, ϕ_o, with which it interacts. This is a good approximation except for very large atomic numbers. As both the perturbation

and the initial state do not vary with energy the only source of the oscillations observed in the absorption coefficient is the photoelectron final state $\psi_{\mathbf{k}}(\mathbf{r})$. Hence the EXAFS is a final state effect.

Although, experimentally, we measure the X-ray absorption, the theory of the EXAFS has almost nothing to do with the interaction of radiation and matter. The coupling with the electromagnetic field generally only enters the theory via the dipole interaction above. Instead, the physics most relevant to the EXAFS is that of electron scattering. Conceptually the EXAFS problem is the same as that encountered in LEED or RHEED, the scattering of some propagating electron state by the atoms in the sample. The only difference between the EXAFS and the other electron diffraction problems is that the source of the EXAFS photoelectron lies within the atoms themselves.

1.2 The EXAFS

It has long been known that the physical origin of the EXAFS is due to a final state interference effect. When an atom absorbs an X-ray photon a photoelectron and a hole in a deep core state are produced. In the absence of neighbouring atoms the wavefunction of the ejected photoelectron is a purely outgoing spherical wave. In condensed matter however, the photoelectron may be backscattered by the neighbouring atoms. It is the resulting interference between the original outgoing wave and the backscattered wave that gives rise to the oscillatory structure observed in the X-ray absorption coefficient.

Interpretation, but not detailed curve fitting, of EXAFS data may be based on a standard equation first obtained by Stern [3]. This equation has since become known as the plane wave approximation to the EXAFS and provides a robust parameterisation of the more complex forms for the fine structure used for most

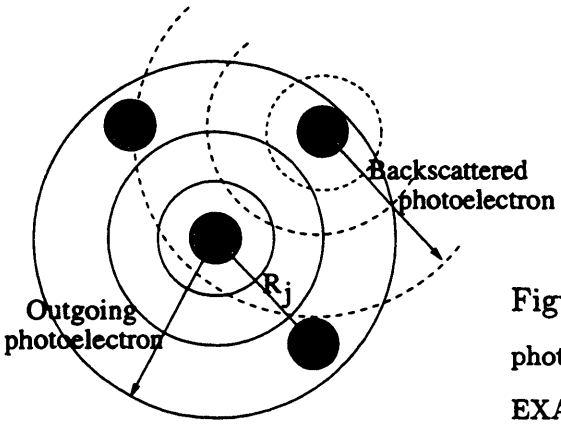

Figure 1.3: Schematic of the photoelectron wave producing the EXAFS.

data analysis [4],

$$\chi(k) = \sum_j s_o^2 e^{-2r_j/\lambda} \frac{N_j |f_j(k,\pi)|}{kr_j^2} e^{-2k^2\sigma_j^2} \sin(2kr_j + 2\delta_l(k,r) + \psi_j). \qquad (1.3)$$

Equation (1.3) describes the extended X-ray absorption fine structure due to scattering by shells of atoms. A typical shell consists of N_j neighbours located at a distance R_j from the absorbing atom. $f_j(k,\pi)$ is the backscattering amplitude from each of the N_j atoms of the jth type. The argument of the sine term contains the effective change of phase of the photoelectron as it travels to the scattering atom and back. The main contribution to the phase-shift is the $2kr_j$ from the interatomic distance travelled, the $2\delta_l$ is the phase-shift due to the excited central atom potential, whilst ψ_j is the phase of the backscattering factor. The EXAFS phase can be measured very accurately. It is the phase which controls the determination of the interatomic distance, r_j, and hence EXAFS is a good method for evaluating this quantity, typically obtaining results to the $\pm 0.02\mathring{A}$ level.

The amplitude of the EXAFS is, however, less well defined. It varies with N_j, the number of near neighbour atoms, but also with static and thermal disorder and because of many-electron processes. These effects are less well understood and typically EXAFS amplitudes, and hence coordination numbers, can be determined no more accurately than by $\pm 10\%$. In the plane wave

approximation the amplitude effects are described by a number of semi-empirical parameters. The Debye-Waller factor, $\exp(-2k^2\sigma_j^2)$, allows for static and thermal disorder effects, σ_j^2 being the mean square variation in atomic distance. The reduction factors, $\exp(-2r_j/\lambda)$, and $s_o^2(k)$ account for many body processes which contribute to the X-ray absorption coefficient but not to the fine structure leading to an apparent decrease in the EXAFS amplitudes. $\exp(-2r_j/\lambda)$, and $s_o^2(k)$ model the losses in the EXAFS due to photoelectron mean free path effects and many electron excitations at the absorbing atom respectively. These will be discussed in more detail in the following section.

1.3 Many-Body Effects

Equation (1.3) and its more accurate analogous forms, used in actual data analysis, suffer from the problem that they are derived within the single electron approximation. In reality, however, the EXAFS problem is inherently a many-body one. The system consists of many electrons all of which interact via the coulomb potential. When an atom absorbs an X-ray photon a photoelectron and a hole in a deep core state are produced. The core hole - photoelectron system corresponds to a time-dependent change in potential which is, in general, extremely complex. It will obviously affect the behaviour of the other electrons in the atom, the so called passive electrons. However, the response of the passive electrons to the core hole - photoelectron system will in turn affect the original photoelectron via the strong electron-electron interaction, and so on. Consequently the photoabsorption can cause transitions between any of the many-electron states ignored in a purely single electron calculation. Many channels exist for the excitation of the electrons which are absent from a one electron treatment. Unfortunately it is impossible to model this complicated process exactly and self-

consistently. Instead, many-electron effects are generally approximated using additions to the effective single electron scattering potentials.

The many-body problem can be summarised by two effects. First, the coulomb interactions between electrons alter the effective one electron potential seen by the photoelectron. Second, the passive electrons in the atom may be excited because of the change in potential caused by the creation of the core hole and photoelectron.

In the ground state the photoelectron scattering potential may be modelled using an effective exchange and correlation potential, the self-energy. This is discussed in more detail in chapters 3,4, and 5. However, there is some confusion as to how best to model the actual potential seen by the photoelectron as the passive electrons respond self-consistently to its presence. Rehr *et al* [5] suggest that there are two options for approximating this potential. It may be derived from an atomic configuration with the passive electrons in their initial states or from the partially or fully relaxed final state.

EXAFS calculations generally use the atomic final state to specify the potential. In the high energy limit the unrelaxed Z approximation is generally considered appropriate, in which the atomic configuration is taken to be that of the Z atom without a contribution from the core orbital from which the photoelectron is ionised. For lower energy photoelectrons the passive electrons have time to respond (on a time scale of $\sim 1/\omega_o$) to the presence of the core hole before the photoelectron has completed its journey to the scattering atom and back. In this case the photoelectron perceives the so called Z+1 fully relaxed atomic configuration where the passive electron wavefunctions are taken from the neutral Z+1 atom. Although physical arguments from the response times of the passives exist for both cases neither is, in any sense, an exact approximation. They are simply used, because, from data analysis, they can be shown to work adequately

for the calculation of the EXAFS. Fortunately the two methods also give almost equivalent phase-shifts [6].

The first of the choices for the passive electron configuration is based on the atomic ground state. This is the choice made when calculating the self-energy from the local density approximation and comes from perturbation theory in which the excited states are expanded in terms of the ground state. As we deal in the main with perturbation theory in this thesis this is the choice we make for the electronic configurations when determining the atomic potential. When considering the photoelectron this approximation is more accurate in the high energy limit.

1.3.1 Inelastic Effects

Inelastic processes involve the interaction between the photoelectron and the other electrons in the sample, both on the central atom and on the scattering atoms. These processes are therefore completely neglected in the purely one electron result for the X-ray absorption coefficient (eqn.(1.2)) and can only be added to the EXAFS expression as *ad hoc* empirical factors designed to make the theory and experiment agree.

The effect of inelastic processes is to diminish the EXAFS. Interference between the outgoing and incoming photoelectron waves can only take place if both waves are at the same energy. If the photoelectron has been inelastically scattered at any time on its journey out to a scattering atom and back it will not contribute to the EXAFS. Inelastic effects will, however, obviously contribute to the total absorption coefficient. The X-ray absorption coefficient obtained via both single and multiple electron calculations must remain approximately the same (see chapter 7) as both calculations satisfy the same sum rule [7]. This means that the overall result for μ does not change when we take many-electron effects into

account. Thus, because the number of absorption events which contribute to the EXAFS is diminished whilst the number of total absorption events remains the same, the magnitude of the EXAFS function must be decreased (see eqn.(1.1)).

Inelastic effects are generally split into two types of process. Those in which the photoelectron is inelastically scattered as it propagates between the central and scattering atoms, known as extrinsic events, and those involving the creation of the core hole, known as intrinsic events.

Extrinsic Process

The extrinsic effects are modelled in equation (1.3) by the mean free path term, $\exp(-2R_j/\lambda)$. As the photoelectron propagates to and from the scattering atom it may excite electron hole pairs or cause collective excitations, the plasmons. These processes are the same as those observed when an external electron beam propagates through a solid and have therefore been studied in LEED and RHEED theory. The losses lead to a decay of the final state, electrons are effectively removed from the elastically scattered beam giving rise to a diminution in the EXAFS signal. This is phenomenologically modelled using the mean free path term. The energy dependence of the extrinsic losses is, however, important and is not included correctly in the simple, semi-empirical, mean free path expression. Typically, in EXAFS calculations the mean free path length is approximated by $\lambda = k/V_{PI}$ where V_{PI} is a constant imaginary part to the potential of approximately $4eV$. This is the canonical figure taken from LEED calculations [8]. Using a constant imaginary part to the potential we obtain an unphysical mean free path length of zero as the photoelectron energy becomes small. Instead the extrinsic losses can be better modelled via the imaginary part of an energy-dependent scattering potential, the self-energy. Such a potential gives rise to complex phase-shifts in equation (1.3) and therefore reduces the amplitudes

automatically without the need for the additional mean free path term. In EXAFS calculations the self-energy is most commonly approximated using the Hedin-Lundqvist potential [9]. This potential is obtained from uniform electron gas relations and was first applied to EXAFS calculations by Lee and Beni [10] using the local density approximation.

Intrinsic Losses

The intrinsic effects are those arising from the creation of the core hole. The photoexcitation of a core electron results in a change of the atomic potential experienced by the remaining passive electrons. This change in potential means that the passives, too, may be excited, removing energy from the photoelectron. If the passive electrons are excited into the continuum the process is known as shake-off. In this case the possible range of secondary and hence final photoelectron energies is continuous and any interference between the photoelectron waves will tend to cancel. Events in which two or more electrons are excited into the continuum will therefore not contribute to the EXAFS. This effect is modelled using the amplitude reduction factor, s_o^2, in equation (1.3). s_o^2 is the probability that each of the passive electrons remains in its initial state and is generally taken to be a constant, although this factor, too, is actually energy-dependent.

Events are also possible where passive electrons are shaken into bound excited states. These shake-up processes produce photoelectrons of definite energy which will cause oscillations in the X-ray absorption coefficient, although of a slightly different frequency than the primary channel EXAFS (the EXAFS obtained when no secondary electrons are excited). However, the shake-up probability is small compared to that of shake-off events [11, 12] and is therefore usually ignored [13]. Generally the shake transitions involve the weakly bound initial states. The energies of the shake-up transitions will therefore tend to be small and hence the

photoelectron energy will not differ from that of the elastically scattered primary photoelectron by more than a few volts. Thus, experimentally one cannot resolve the two contributions to the EXAFS and, in practice, the shake-up channels cause no diminution to the primary channel EXAFS.

The core hole also has a finite lifetime. Eventually the passive electrons will rearrange themselves so as to fill the deep core state from whence the photoelectron came. This process, however, takes place on time scales greater than that of the photoelectron transit time. It simply places an upper bound on the EXAFS photoelectron lifetime as interference cannot occur if the outgoing and in-going photoelectron waves experience different potentials. From X-ray emission linewidths the core hole lifetime can be measured fairly accurately. Typically it is found to be of the order of 10^{-15} seconds corresponding to an inverse energy of approximately 10^{-4} of the edge energy. This finite lifetime effect can be added to the EXAFS expression (eqn.(1.3)) by effectively reducing the mean free path length. Such corrections are added automatically in data analysis programs such as EXCURV98 [14] and therefore will not be considered in the rest of this thesis.

1.4 Synopsis of the Thesis

The uncertainties in existing EXAFS theory are almost all due to the neglect of many-body effects. Historically, the approach to many-body effects in EXAFS has been a strange one. The theory has been developed either via an entirely formal approach (see for example, Bardyszewski and Hedin [15]) or through an *ad-hoc* empirical approach using fitting parameters such as the ones described above. Little work, however, has been performed in the area in between. Approximations to the self-energy, which describes extrinsic processes, have been calculated which are applicable to EXAFS calculations. However, these approximations are

currently based on free electron gas models and the local density approximation [10]. Their accuracy for EXAFS calculations has not been properly determined and they could certainly be improved to achieve a more accurate determination of the effective mean free path.

The formal, many-body approach of Bardyszewski and Hedin [15] may be exact but, in such work, little attention is paid to the practicalities of computation and data analysis. For a method to be of use to the EXAFS community it must be applicable to all elements. It must also be fast enough to run so that data analysis, where the EXAFS has to be calculated many times for many different sets of parameters, may proceed in real time.

The approach of the experimentalists, on the other hand, has been to devise approximations that work well enough and then to leave well alone. For example, in LEED analysis the use of a constant imaginary part to the potential was long considered to be completely adequate [8]. In RHEED calculations also, a very simple form of damping is commonly used, typically with the imaginary part of the potential described as a constant fraction of the real part [16]. Even in EXAFS calculations a constant imaginary part of the potential (and hence a mean free path proportional to k) and a constant s_o^2 were considered to be good enough for many years.

In this thesis we try to do better than the empirical expressions described above whilst still retaining the ease of computation and the calculability for all elements to make our methods of use. The goal, above all, is to try to reduce the number of free fitting parameters in the EXAFS equations.

In chapter 2 we develop the theory behind the X-ray absorption coefficient and the EXAFS. We also derive expressions with which we may examine the effect of an effective, complex scattering potential on the amplitude of the EXAFS independently.

Chapter 3 is concerned with the many-body theory behind such a potential. Many-body physics is heavily reliant on the inverse dielectric function. In this chapter we calculate numerical results for this function using an atomic theory and compare them to the approximate forms for the inverse dielectric function used in most present calculations.

In chapter 4 we investigate one of the free electron gas models for the complex self-energy that is commonly used in modern EXAFS data analysis. The EXAFS amplitudes obtained using the Hedin Lundqvist potential [9, 10] are examined in detail using the expressions derived in chapter 2.

Chapter 5 is concerned with a more complex approach to the calculation of an energy-dependent scattering potential. We extend a method first proposed by Beni, Lee and Platzman [17] to calculate the self-energy using an atomic formalism. This formalism is intuitively more appealing than the local density model examined in chapter 4. In this chapter we examine its suitability for EXAFS calculations.

In chapter 6 we examine the intrinsic effects in more detail. In this chapter we calculate the probability of secondary electron excitation following the photoabsorption event. This is related to the amplitude reduction factor, s_o^2, of equation (1.3) and is compared to experiment. The calculation is performed under the sudden approximation [18] using Slaters rules [19] to model the effect of the core hole. We also investigate the chemical dependence of the amplitude reduction factor using tight binding wavefunctions.

In chapter 7 we model the core hole - photoelectron system in more detail using time-dependent perturbation theory. This chapter is based on a method proposed by Thomas [20] to describe the time dependence of the core hole - photoelectron potential in terms of a model function. We extend Thomas' model to correctly describe shake-off processes using the experimentally found high energy excitation

probabilities, then perform the calculation using a dynamically screened core hole and no fitting parameters. The results of both calculations are compared to experiment and their applicability to real EXAFS calculations discussed.

Finally, chapter 8 summarises and concludes the work of this thesis. We also make some suggestions for further work.

Chapter 2

The X-ray Absorption Fine Structure

In this chapter we develop the theory underlying the X-ray absorption fine structure and the X-ray absorption coefficient. We also derive expressions describing the effect of an imaginary part of the potential in terms of a perturbation series. As discussed in Chapter 1, an imaginary potential may be used to describe inelastic scattering events which reduce the strength of the elastically scattered photoelectron beam and hence the EXAFS.

Since the proliferation of EXAFS experiments in the early 1970's there have been major improvements in the understanding and theoretical development of the phenomena. In 1974 the first approximate short range form of the EXAFS was developed by Stern [3]. In 1975 this was succeeded by an exact form of the theory due to Lee and Pendry [4] who treated the electron scattering problem, at the heart of EXAFS, using photoelectron wavefunctions. In the same year another exact form of the theory was developed by Ashley and Doniach [21] using a Green function formalism. The two theories are, however, equivalent. Both model the outgoing photoelectron exactly using spherical waves and, in both theories, it is found that the inclusion of single scattering events is adequate in most cases. Multiple scattering is only important at low energies close to the absorption edge and for certain configurations of atoms, generally when one scattering atom is

directly shadowed by another. In the high energy limit the spherical waves used by Lee and Pendry can be approximated by plane waves and we return to the original theory of Stern. The drawback with the exact theory of Lee and Pendry is that it is mathematically complex and time consuming.

In the early 1980's Gurman *et al* [22, 23] discovered that the theory could be greatly simplified by averaging over the angles of the inter-atomic vectors relative to the direction of the photoelectron beam. This is, of course, exact for both amorphous and polycrystalline samples. The so called fast curved wave theory greatly reduced the computer time needed for EXAFS data analysis and is used in the standard Daresbury data analysis program EXCURV98 [14].

All the theories mentioned are effectively single electron theories. Many-body effects are introduced by the inclusion of an additional effective scattering potential. In 1975 Lee and Beni [10] developed an effective, energy-dependent, exchange and correlation potential which corrected for systematic errors of up to $\pm 4\%$ in the calculated inter-atomic distances. The errors were caused because the full interaction potential falls with increasing electron energy whereas the simple model potentials used before Lee and Beni did not exhibit this energy dependence. The potential used by Lee and Beni is complex, with the imaginary part designed to model the extrinsic inelastic electron-electron scattering. The imaginary part of the potential reduces the amplitude of the EXAFS as discussed in Chapter 1. However, there is some confusion as to exactly how much the amplitude is reduced by the inclusion of the imaginary potential.

In this chapter we develop expressions for the absorption coefficient and the plane wave approximation to the EXAFS (eqn.(1.3)) by considering the photoelectron flux. We are ultimately interested in the amplitudes of the EXAFS produced by the imaginary part of the potential. We could, in principle, study the amplitude by using a program such as EXCURV98 [14] to calculate and compare

the EXAFS in the presence and the absence of the complex potential. A complex potential makes the phase-shifts in equation (1.3) complex leading to changes in phase and magnitude of the calculated EXAFS signal. However, for ease of computation and so that we may study the amplitude effects independently, we choose to treat the effects of the imaginary part of the potential as a small perturbation. We then obtain expressions for the EXAFS and the elastically scattered flux in which the effect of the imaginary potential is simply given as a multiplying factor on the amplitude. To our knowledge this is the first instance where such expressions have been derived.

The chapter is split into three sections. In the first we outline some of the background results underlying most of the theory in the rest of the thesis. We give a brief description of the muffin tin potential and list the standard results for the Hartree Green function and the scattering wavefunctions. We then outline the calculation of the radial solutions to the Schrödinger equation and specify the initial atomic states used.

In the second section we calculate the photoelectron flux and hence the X-ray absorption coefficient following the irradiation of an isolated atom by a beam of X-ray photons. The calculation is performed both in the presence and the absence of an imaginary potential.

In the final section we extend the theory for the isolated atom to include a number of scattering atoms. This then gives the EXAFS. We evaluate an expression to first order in the imaginary part of the potential for the EXAFS amplitudes.

2.1 Background

2.1.1 The Muffin Tin Potential

All calculations are performed within the muffin tin approximation of Loucks [24]. In this approximation the actual potential inside a solid is taken to be spherically symmetric inside spheres centred on each atomic site. In the central portion of the spheres the muffin tin potential is assumed to be atomic in character. In the outer regions, however, the atomic nature of the potentials is modified somewhat by the overlap from neighbouring atoms. Outside the muffin tin spheres the potential is made constant. We assume the atomic potentials to be of the Hartree form with the exchange and correlation approximated by some one body potential, $V_{XC}(r)$. Typically we take the exchange and correlation potential to be the Slater $X\alpha$ free electron exchange or the real part of the Hedin-Lundqvist potential. These forms are discussed further in Chapters 3 and 4. Thus we have the potential seen by an electron,

$$V(r) = \frac{-Z}{r} + V_h(r) + V_{XC}(r). \tag{2.1}$$

The first term is due to the nucleus whilst $V_h(r)$ is the electronic contribution obtained from Poisson's equation,

$$\nabla^2 V_h(r) = -8\pi n(r). \tag{2.2}$$

where $n(r)$ is the radially varying atomic charge density.

2.1.2 The Green Function

Within the muffin tin approximation of Loucks [24] we may use the following standard results for the photoelectron Green functions in the continuum [25]. We obtain different results for the Green function depending on whether r and r' are

inside or outside of the muffin tin spheres,

$$\begin{aligned} G_o(\mathbf{r},\mathbf{r}',\omega) &= -\imath k \sum_{lm} h_l^{(1)}(kr) e^{\imath\delta_l} \left(e^{\imath\delta_l} h_l^{(1)}(kr') + e^{-\imath\delta_l} h_l^{(2)}(kr') \right) Y_{lm}^*(\hat{r}) Y_{lm}(\hat{r}') \\ & \qquad\qquad r > r' > r_{mt} \\ &= -\imath k \sum_{lm} h_l^{(1)}(kr) e^{\imath\delta_l} R_l(kr') Y_{lm}^*(\hat{r}) Y_{lm}(\hat{r}') \\ & \qquad\qquad r > r_{mt} > r' \\ &= -\imath k \sum_{lm} R_l(kr') \frac{1}{2} \left(R_l(kr) - \imath X_l(kr) \right) Y_{lm}^*(\hat{r}) Y_{lm}(\hat{r}') \\ & \qquad\qquad r_{mt} > r > r'. \end{aligned} \tag{2.3}$$

$R_l(kr)$ and $X_l(kr)$ are the regular and irregular scattering solutions to the Schrödinger equation in the presence of the atomic potential whilst the free space wavefunctions have been defined in terms of the spherical Hankel functions, $h_l^{(1)}(kr)$ and $h_l^{(2)}(kr)$. $\omega = \frac{1}{2}k^2$ and we have taken the continuum scattering state wavefunctions to be,

$$\psi(\mathbf{k},\mathbf{r}) = \sum_{lm} 2\pi\imath^l e^{\imath\delta_l} \left(e^{\imath\delta_l} h_l^{(1)}(kr) - e^{-\imath\delta_l} h_l^{(2)}(kr) \right) Y_{lm}(\hat{r}) Y_{lm}^*(\hat{k}) \qquad r > r_{mt} \tag{2.4}$$

$$\psi(\mathbf{k},\mathbf{r}) = \sum_{lm} 2\pi\imath^l e^{\imath\delta_l} R_l(kr) Y_{lm}(\hat{r}) Y_{lm}^*(\hat{k}) \qquad r < r_{mt}. \tag{2.5}$$

where δ_l are the partial wave phase-shifts.

2.1.3 The Regular Solution

The scattering final states, $R_l(r)$, are calculated by numerically integrating out the Schrödinger equation from $r = 0$ to the edge of the muffin tin radius. The radial Schrödinger equation can be written as,

$$\left\{ \frac{d^2}{dr^2} + \frac{2}{r}\frac{d}{dr} - \frac{l(l+1)}{r^2} - 2(V - E) \right\} \xi_l(r) = 0. \tag{2.6}$$

The regular solutions to the Schrödinger equation, $R_l(r)$ are the solutions to the above equation which go as r^l near to the origin.

In the course of this thesis we will need to calculate the final states for angular momenta of up to $l = 20$. At high values of the angular momentum quantum number the centrifugal barrier term, $l(l+1)/r^2$, in equation (2.6) dominates and pushes the final state away from the origin. R_l varies as r^l near to $r = 0$, so, near to the origin, R_l becomes very small. This leads to inaccuracies in the initial conditions used to start the integration and hence numerical problems in the calculated final states.

In order to make the numerical integration stable for large values of l we must solve the Schrödinger equation for $\psi_l(r) = r^{-(l-1)}R_l(r)$ rather than for $R_l(r)$ directly,

$$\frac{d^2\psi_l}{dr^2} + \frac{2l}{r}\frac{d\psi_l}{dr} - 2(V-E)\psi_l = 0. \tag{2.7}$$

Rewriting the standard Schrödinger equation for $\psi_l(r)$ as two coupled first order differential equations we have,

$$\frac{d\psi(r)}{dr} = z(r) - \frac{2l}{r}\psi(r) \tag{2.8}$$

and,

$$\frac{dz(r)}{dr} = 2(V(r)-E)\psi(r), \tag{2.9}$$

Equations (2.8) and (2.9) are solved using a standard Runga Kutta routine [8]. Near to the origin we can expand ψ_l and $V(r)$ as power series. This allows us to set the initial conditions with which to start the integration,

$$\begin{aligned} \psi(r) &= r\left(1 - \frac{Z}{l+1}r + \frac{Z^2 - (l+1)(V_o+E)}{(2l+3)(l+1)}r^2 + \ldots\right) \\ z(r) &= (2l+1) - 2Zr + \frac{Z^2 - (l+1)(V_o+E)}{(l+1)}r^2, \end{aligned} \tag{2.10}$$

where, Z is the atomic number and close to the origin the atomic potential is written as,

$$V(r) = -\frac{Z}{r} - V_o + \ldots \tag{2.11}$$

Finally, at the boundary of the muffin tins, the radial functions are matched to free space continuum wavefunctions of the form,

$$R_l(r) = 2\left(\cos\delta_l j_l(kr) + \sin\delta_l n_l(kr)\right). \tag{2.12}$$

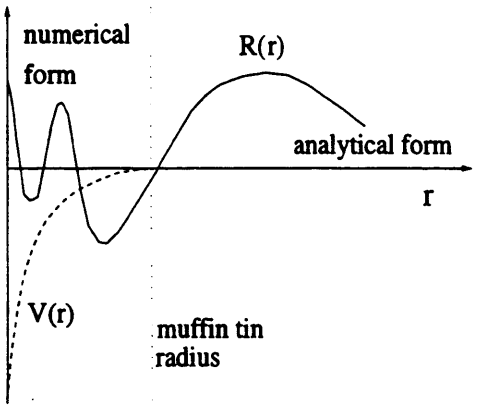

Figure 2.1: Schematic representation of the continuum solution to the radial Schrödinger equation. The solid line shows the radial solution, the dashed line the atomic potential and the dotted line the extent of the atomic muffin tin.

2.1.4 The Irregular Solution

Outside the range of the atomic potential the regular solution is given by a phase-shifted spherical Bessel function. The irregular solution, on the other hand, is a phase-shifted spherical Neumann function. By first calculating the regular solution to the Schrödinger equation we can find the phase-shifts, δ_l. Knowing the phase-shifts, the irregular solution may be specified completely outside of the muffin tin sphere. We may then numerically integrate inwards to solve for the irregular solution in all regions of space.

The irregular function, X_l, is a solution to equation (2.6) which goes as $1/r^{l+1}$ near to $r = 0$. When calculating the irregular solutions numerically we solve for $\psi_l = r^{l+2}X_l$ rather than for X_l directly to avoid the numerical divergences at the origin,

$$\frac{d^2\psi_l}{dr^2} - \frac{2(l+1)}{r}\frac{d\psi_l}{dr} + \left(\frac{2(l+1)}{r^2} - 2(V-E)\right)\psi_l. \tag{2.13}$$

Again, we separate this second order differential equation into a set of coupled first order differential equations,

$$\frac{d\psi(r)}{dr} = z(r) + \frac{2(l+1)}{r}\psi(r) \tag{2.14}$$

and,

$$\frac{dz(r)}{dr} = 2(V(r) - E)\psi(r). \tag{2.15}$$

These equations may be solved numerically using, for example, the NAG routine D02PCF.

2.1.5 The Initial States

We take the bound atomic states, $\phi_{l_o}(\mathbf{r})$, from tabulations of Roothaan-Hartree-Fock atomic functions by Clementi and Roetti [26] and by A D and R S McLean [27].

The initial state binding energies, ω_o, are taken from experimental tables where available [28] or from the theoretical predictions of Clementi and Roetti otherwise. As spin orbit coupling is not included in any other way apart from in the binding energies we take each of the $(2l_o + 1)$ m_o sub levels to be of identical form. However, we do scale the contributions of each of the m_o states according to the ratio of the statistical weights of the sub levels. Thus, for example, the $2p_{3/2}$ is taken to contribute twice the strength of the $2p_{1/2}$ initial state to the relevant matrix elements.

2.2 The Isolated Atom

2.2.1 A Real Scattering Potential

To evaluate the photoelectron flux we must first use standard perturbation theory to calculate the photoelectron wave function. We begin by treating an isolated

atomic system in which an X-ray photon, of frequency ω, interacts with a single, well defined, initial state. We may then write the perturbed wavefunction as,

$$\psi = \phi_o(\mathbf{r}) + G_o(\mathbf{r}, \mathbf{r}', \omega - |\omega_o|)H'(\mathbf{r}')\phi_o(\mathbf{r}'). \tag{2.16}$$

$\phi_o(\mathbf{r})$ is the electronic initial state of energy ω_o and $G_o(\mathbf{r}, \mathbf{r}', \omega - |\omega_o|)$ is the Hartree Green function for the system which is zero if $\omega < \omega_o$. We have assumed that the perturbation has been switched on adiabatically and is given, under the dipole approximation, by,

$$H'(\mathbf{r}') = E_o r \sum_p Y_{1p}(\hat{r}) Y^*_{1p}(\hat{\epsilon}), \tag{2.17}$$

where E_o is the strength of the electromagnetic field of the X-ray beam and the Y_{lm}'s are spherical harmonics.

Using the explicit forms for the Green function (eqn.(2.3)) we can immediately examine the form of the photoelectron wavefunction using equation (2.16). As expected, the photoelectron wavefunction will have the form of a phase-shifted, flux carrying, outgoing spherical wave, with an amplitude modified by the perturbation matrix element, $\langle R_l | H' | \phi_o \rangle$. We are interested in the photoelectron flux and hence the photoelectron wavefunctions far from the absorbing atom. This simplifies matters because, at large r, we may ignore the first term in equation (2.16) as the initial state, $|\phi_o(\mathbf{r})\rangle$, will always be highly localised. Thus,

$$\begin{aligned} \psi &= \int G_o(\mathbf{r}, \mathbf{r}', \omega - |\omega_o|) H'(\mathbf{r}') \phi_{l_o}(r') Y_{l_o m_o}(\hat{r}') d\mathbf{r}', \\ &= -\sum_{l,m,p} \frac{2\pi\imath k}{3} E_o h_l^{(1)}(kr) e^{\imath\delta_l} Y_{lm}(\hat{r}) \langle Y_{1p} | Y_{lm} | Y_{l_o m_o} \rangle \langle R_l | r | \phi_{l_o} \rangle \end{aligned} \tag{2.18}$$

Where $k = \sqrt{2(\omega - |\omega_o|)}$ and we have written the initial state as the product of a radial function, $\phi_{l_o}(r')$, and a spherical harmonic, $Y_{l_o m_o}(\hat{r})$. Using this result, the photoelectron flux through a sphere of radius r centred on the absorbing atom may be calculated from the standard expression

$$S = \frac{1}{2\imath} \int \left(\psi^* \frac{d\psi}{dr} - \psi \frac{d\psi^*}{dr} \right) r^2 d\hat{r}. \tag{2.19}$$

Then, substituting for the wavefunction from equation (2.18) we find that,

$$S = \frac{k^2 E_o^2}{4\imath} \sum_l \left(h_l^{(2)} \frac{dh_l^{(1)}}{dr} - h_l^{(1)} \frac{dh_l^{(2)}}{dr} \right) r^2 |\langle R_l | r | \phi_{l_o} \rangle|^2 \times \sum_{m,p,q} \frac{16\pi^2}{9} Y_{1p}(\hat{\epsilon}) Y_{1q}^*(\hat{\epsilon}) \int Y_{lm} Y_{l_o m_o} Y_{1p} d\hat{r} \int Y_{lm} Y_{l_o m_o} Y_{1q} d\hat{r}. \quad (2.20)$$

To obtain the contribution to the flux from a given initial state of angular momentum l_o we must sum over the degenerate m_o sub levels of the initial state, multiplying by 2 to account for spin degeneracy. By summing over m_o it is also possible to simplify the above equation using a result from Brink and Satchler [29]. The integrals over spherical harmonics may be written in terms of the Wigner-3j coefficients,

$$\int Y_{lm} Y_{Lp} Y_{l_o m_o} d\hat{r} = \left(\frac{(2l+1)(2L+1)(2l+1)}{4\pi} \right)^{\frac{1}{2}} \begin{pmatrix} l & L & l_o \\ m & p & m_o \end{pmatrix} \begin{pmatrix} l & L & l_o \\ 0 & 0 & 0 \end{pmatrix}. \quad (2.21)$$

In equation (2.20) we have two integrals over the spherical harmonics. Thus, noting that the Wigner-3j coefficients may be cyclically permuted, we can apply one of the orthogonality relations of Brink and Satchler [29],

$$\sum_{m_o m} \begin{pmatrix} l & L & l_o \\ m & p & m_o \end{pmatrix} \begin{pmatrix} l & L' & l_o \\ m & q & m_o \end{pmatrix} = \frac{1}{(2L+1)} \delta_{LL'} \delta_{pq}. \quad (2.22)$$

In equation (2.20) $L = L' = 1$. Then, using the addition theorem [30] to write $\sum_{m=-1}^{1} Y_{1M}(\hat{q}) Y_{1M}^*(\hat{q}) = 3/(4\pi)$, we have that,

$$S = \frac{k^2 E_o^2}{8\imath} \sum_l \left(h_l^{(2)} \frac{dh_l^{(1)}}{dr} - h_l^{(1)} \frac{dh_l^{(2)}}{dr} \right) r^2 |\langle R_l | r | \phi_{l_o} \rangle|^2 \begin{pmatrix} l & 1 & l_o \\ 0 & 0 & 0 \end{pmatrix}^2. \quad (2.23)$$

The Wigner-3j coefficient in equation (2.23) is only non zero if $l = l_o \pm 1$. Also, we may rewrite the Wronskian of the spherical Hankel functions using a relation from Abramowitz and Stegun [31],

$$h_l^{(2)} \frac{dh_l^{(1)}}{dr} - h_l^{(1)} \frac{dh_l^{(2)}}{dr} = \frac{2\imath}{kr^2}. \quad (2.24)$$

Then, equation (2.23) for the photoelectron flux becomes,

$$S = \frac{k}{6}(E_o)^2 \sum_l A(l, l_o)|\langle R_l|r|\phi_{l_o}\rangle|^2, \tag{2.25}$$

where the angle factor $A(l, lo)$ is defined as,

$$\begin{aligned} A(l, l_o) &= l_o + 1 && l = l_o + 1 \\ &= l_o && l = l_o - 1 \\ &= 0 && l \neq l_o \pm 1. \end{aligned} \tag{2.26}$$

This result for the flux through a sphere centred on the absorbing atom is also equal to the rate of photon absorption and as such may be easily related to the total X-ray absorption coefficient, $\mu_o(\omega)$. The X-ray absorption coefficient is defined as the rate of absorption of photon energy divided by the rate of energy transport in the X-ray beam, $\mu = 8\pi\omega S/cE_o^2$. In deriving equation (2.25) we have assumed a fully occupied n_o, l_o orbital. To obtain the contribution from a partially occupied initial state we must multiply by the number of electrons in the state $n_{(n_o,l_o)}$ divided by $2(2l_o + 1)$. We must then sum over all the occupied initial states to obtain the total contribution to the X-ray absorption coefficient,

$$\mu_o(\omega) = \frac{2\pi k\omega}{3c} \sum_{n_o,l_o} \frac{n_{(n_o,l_o)}}{2l_o + 1} \sum_l A(l, l_o)|\langle R_l|r|\phi_{l_o}\rangle|^2. \tag{2.27}$$

This simple formula gives the standard result for the X-ray absorption coefficient of an isolated atom under the dipole approximation [32]. Energy conservation is contained in the wavenumber of the final state, $k = \sqrt{2(\omega - |\omega_o|)}$ whilst the sum over initial states gives each absorption edge in turn as ω becomes larger than $|\omega_o|$.

2.2.2 A Complex Scattering Potential

1st Order Calculation

In the presence of an entirely real scattering potential equation (2.25) gives the photoelectron flux through the elastic scattering channel. When inelastic scattering events are introduced via an imaginary part to the exchange and correlation potential, $V_{XC}(r)$, result (2.25) can be viewed as the total flux through all open scattering channels. The magnitude of the photoelectron flux through the elastic channel (the only photoelectrons which contribute to the EXAFS) may then be examined by treating the imaginary part of the potential as a perturbation on the Green function. The complex exchange and correlation potential is written as the sum of its real and imaginary parts,

$$V_{XC}(\omega, r) = V_R(\omega, r) - \imath V_I(\omega, r). \tag{2.28}$$

In calculating the perturbed G we take the radial wavefunctions $R_l(kr)$ to be solutions of the Schrödinger equation in the presence of the real part of the exchange and correlation potential so that in equation (2.1) we must replace V_{XC} by its real part, $V_R(\omega, r)$. Then, writing the photoelectron Green function in terms of a perturbation series to first order in the imaginary part of the potential, V_I, we have that,

$$G_1(\mathbf{r}, \mathbf{r}') = G_o(\mathbf{r}, \mathbf{r}') - \imath G_o(\mathbf{r}, \mathbf{r}_1) V_I(r_1) G_o(\mathbf{r}_1, \mathbf{r}'), \tag{2.29}$$

where the ω labels have been suppressed and we have taken it as given that the Green function and the exchange and correlation potential are evaluated at an energy of $\omega - |\omega_o|$. Substituting the perturbation expansion for $G_o(\mathbf{r}, \mathbf{r}')$, into equation (2.16) we may write the photoelectron wavefunction in the presence of the complex potential at large r as,

$$\psi = \Big\{ \int G_o(\mathbf{r},\mathbf{r}') H'(\mathbf{r}') \phi_{l_o}(r') Y_{l_o m_o}(\hat{r}') d\mathbf{r}' \\ -\imath \int G_o(\mathbf{r},\mathbf{r}_1) V_I(r_1) G_o(\mathbf{r}_1,\mathbf{r}') H'(\mathbf{r}') \phi_{l_o}(r') Y_{l_o m_o}(\hat{r}') d\mathbf{r}_1 d\mathbf{r}' \Big\}, \qquad (2.30)$$

where the Green function $G_o(\mathbf{r},\mathbf{r}')$ has $r' < r_{mt}$ and $r > r_{mt}$ whilst $G_o(\mathbf{r}_1,\mathbf{r}')$ has both r_1 and r' inside the muffin tin. We assume that $r_1 > r'$ as the initial state, $|\phi_{l_o}\rangle$ will always be highly localised whilst the imaginary potential, V_I is zero toward the centre of the atom. This means that the double integral in equation (2.30) will only be significant in the regions where $r_1 > r'$. Also, within the muffin tin approximation, V_I is spherically symmetric so that the angular integrals over the directions of $\mathbf{r}_1$ simply reduce to the orthogonality integrals for the spherical harmonics.

Taking the appropriate relations between $\mathbf{r}$, $\mathbf{r}'$ and $\mathbf{r}_1$ we can write the perturbed Green function (eqn.(2.29)) as,

$$G_1(\mathbf{r},\mathbf{r}') = -\imath k \sum_{l,m} e^{\imath\delta_l} h_l^{(1)}(kr) Y_{lm}^*(\hat{r}) R_l(kr') Y_{lm}(\hat{r}') \times \\ \Big\{ 1 - \frac{1}{2} \langle R_l | V_I | R_l - i X_l \rangle \Big\}. \qquad (2.31)$$

The perturbed Green function has the same functional form as G_o, it is merely multiplied by a factor $1 - \frac{1}{2}\langle R_l|V_I|R_l - iX_l\rangle$. We can use result (2.31) to calculate a perturbed wavefunction. This may then be substituted into equation (2.19) to obtain a result for the photoelectron flux through the elastic scattering channel. The integrals are the same as in the previous section, thus, again summing over the degenerate m_o sub levels of the initial state we find that, to first order in V_I, the elastically scattered flux becomes,

$$S = \frac{kE_o^2}{6} \sum_{n_o,l_o} \frac{n_{(n_o,l_o)}}{2(2l_o+1)} \sum_l A(l,l_o) |\langle R_l|r|\phi_{l_o}\rangle|^2 (1 - k\langle R_l|V_I|R_l\rangle). \qquad (2.32)$$

As expected the photoelectron flux through the elastic channel in the presence of the complex potential is less than the total flux through all open channels given

by equation (2.25). Also, the irregular solution to the Schrödinger equation does not contribute to 1st order in V_I. Equation (2.32) is easily related to the elastic contribution to the X-ray absorption coefficient. From equation (2.32) the loss of elastically scattered photoelectron flux as the photoelectron propagates out through the central atom potential is obviously given by,

$$A_l = 1 - k\langle R_l|V_I|R_l\rangle, \tag{2.33}$$

to first order in the imaginary part of the potential. The amplitude of each contribution to the elastically scattered flux and hence the elastic contribution to the X-ray absorption coefficient is obviously edge dependent. It also depends on the angular momentum of the photoelectron final state, with the $l = l_o + 1$ and $l = l_o - 1$ having different values. For K-edges of course we need only consider the $l = 1$ final state.

2nd Order Calculation

We can also calculate the elastic photoelectron flux for an isolated atom to second order in V_I. To 2nd order the perturbed Green function is given by,

$$\begin{aligned} G_2(\mathbf{r},\mathbf{r}') = G_o(\mathbf{r},\mathbf{r}') &- iG_o(\mathbf{r},\mathbf{r}_1)V_I(r_1)G_o(\mathbf{r}_1,\mathbf{r}') \\ &+ G_o(\mathbf{r},\mathbf{r}_1)V_I(r_1)G_o(\mathbf{r}_1,\mathbf{r}_2)V_I(r_2)G_o(\mathbf{r}_2,\mathbf{r}'). \end{aligned} \tag{2.34}$$

To obtain the relevant photoelectron wavefunction far from the scattering atom we need to set $r > r' > r_{mt}$. Also V_I only exists inside the muffin tin, so r_1 and r_2 must be less than r_{mt}. Finally the initial states will again be highly localised as we are dealing with X-ray absorption by the deep core orbitals, for example the $1s$ orbital for K-edge absorption. Then, as V_I is zero close to the nucleus we can again take $r_1 > r'$. Thus, the perturbed Green function will still have the same

functional form as G_o,

$$G_2(\mathbf{r},\mathbf{r}') = -\imath k \sum_{l,m} e^{\imath\delta_l} h_l^{(1)}(kr) Y_{lm}^*(\hat{r}) R_l(kr') Y_{lm}(\hat{r}') \Big\{ 1 - \frac{1}{2}\langle R_l|V_I|R_l - iX_l\rangle + \frac{k^2}{4}\left(\int R_l(r_1)V_I(r_1)F(r_1,r_2)V(r_2)\big[R_l(r_2) - \imath X_l(r_2)\big] r_1^2 r_2^2 dr_1 dr_2 \right) \Big\}. \tag{2.35}$$

Where $F(r_1, r_2)$ is simply the radial part of the unperturbed Green function and has different forms depending on whether r_1 or r_2 is the larger. We can split the double integral above into an integral over r_2 between 0 and r_1 and an integral over r_2 between r_1 and r_{mt} all within the integral over r_1 between 0 and r_{mt}. Then $F(r_1, r_2)$ can be written explicitly in each of the two integrals. Also we can replace $\int_o^{r_1} dr_2$ by $\int_o^{r_{mt}} dr_2 - \int_{r_1}^{r_{mt}} dr_2$. Then, collecting together like terms we find that the second order part of G_2 is given by,

$$\frac{k^2}{4}\Big\{ |\langle R_l|V_I|R_l\rangle|^2 + \int_o^{r_{mt}} \int_{r_1}^{r_{mt}} r_1^2 r_2^2 \big(R_l(r_1)V_I X_l(r_1) R_l(r_2) V_I X_l(r_2) - R_l(r_1)V_I R_l(r_1) X_l(r_2) V_I X_l(r_2) \big) dr_1 dr_2 - |\langle R_l|V_I|X_l\rangle|^2 + C\imath \Big\}. \tag{2.36}$$

The imaginary terms that are second order in V_I, denoted by $C\imath$ in equation (2.36), will not contribute to the flux to 1st or 2nd order. As G_2 has the same functional form as G_o we may easily evaluate the elastically scattered photoelectron flux to second order in V_I. The flux is the same as in equation (2.25), it is simply multiplied by an additional l dependent term,

$$A_l = 1 - k|\langle R_l|V_I|R_l\rangle| + \frac{3}{4}k^2|\langle R_l|V_I|R_l\rangle|^2 - \frac{1}{4}k^2|\langle R_l|V_I|X_l\rangle|^2 - \frac{1}{2}k^2 \int_o^{r_{mt}} \int_r^{r_{mt}} r^2 r'^2 \big(R_l(r)V_I R_l(r) X_l(r') V_I X_l(r') + R_l(r)V_I X_l(r) R_l(r') V_I X_l(r') \big) dr dr'. \tag{2.37}$$

Again, for a K-edge, only $l = 1$ values are allowed and thus the amplitude is a simple multiplicative factor.

The equation above gives the amplitude of the elastically scattered flux to second order in the imaginary part of the potential. We can see that this will be little different from the 1st order calculation of the amplitude (eqn.(2.33)). The integrals over $R_l V_I X_l$ will be small because, as we shall see in Chapter 4, V_I is approximately constant through most of the muffin tin sphere whilst R_l and X_l are orthogonal. To a first approximation we can estimate the strength of the double integral over $R_l(r)V_I R_l(r)X_l(r')V_I X_l(r')$ to be about the same as the square of the radial matrix element, $|\langle R_l|V_I|R_l\rangle|^2$. This is because R_l and X_l have similar magnitudes in the region toward the edge of the muffin tin sphere where V_I exists. There will therefore be some cancellation between these terms leaving the total result for the amplitude to be modified from the 1st order result simply by a factor of $\sim \frac{1}{4}k^2|\langle R_l|V_I|R_l\rangle|^2$.

2.3 The EXAFS

2.3.1 A Real Scattering Potential

To obtain a result including the fine structure we must introduce scattering atoms into the theory. For simplicity's sake we consider a single shell of j scattering atoms at a distance r_j from the central atom. As each atom contributes linearly to the EXAFS we may examine each scatterer individually then sum over all the scattering atoms in the shell to obtain the total EXAFS.

The effect of each additional scattering potential is to perturb the central atom Green function, G_o. We model this perturbation to all orders in the scattering potential by expanding G_o to first order in the T-matrix of the scattering atom,

$$G_s(\mathbf{r},\mathbf{r}') = G_o(\mathbf{r},\mathbf{r}') + G_o(\mathbf{r},\mathbf{r}_1)T_j(\mathbf{r}_1,\mathbf{r}_2)G_o(\mathbf{r}_2,\mathbf{r}'). \qquad (2.38)$$

To obtain the total scattering Green function from a shell of scattering atoms we simply sum the second term above over all the j atoms in the shell.

We will use G_s to again examine the photoelectron flux far from the central atom, this time in the presence of the scattering atoms. Thus $r > r_1$ and $r' < r_2$. In the muffin tin approximation $T_j(\mathbf{r}_1, \mathbf{r}_2)$ only exists inside the muffin tin of the jth scattering atom. To evaluate the integrals involving the T-matrix it is therefore advantageous to change variables to a coordinate system centred on this atom. We choose $\mathbf{r}_1 = \mathbf{r}_j + \mathbf{x}$ and $\mathbf{r}_2 = \mathbf{r}_j + \mathbf{y}$. We may then expand the wavefunctions involved in the central atom Green function in terms of zero potential wavefunctions centred on the scattering atom using a formula from Pendry [8],

$$\begin{aligned} h_l^1(R+x)Y_{lm}(R\hat{+}x) &= \sum_{uv} B_{lmuv} j_u(kx) Y_{uv}(\hat{x}), \\ h_l^2(R+x)Y_{lm}(R\hat{+}x) &= \sum_{uv} B^{(2)}_{lmuv} j_u(kx) Y_{uv}(\hat{x}). \end{aligned} \tag{2.39}$$

The $j_l(kr)$'s are spherical Bessel functions and the expansion matrices, B_{lmuv}, are given by,

$$\begin{aligned} B_{lmuv} &= \sum_{st} 4\pi \imath^{l-u-s} h_s^1(kR) Y_{st}^*(\hat{R}) \int Y_{lm} Y_{st} Y_{uv}^* d\hat{r}, \\ B^{(2)}_{lmuv} &= \sum_{st} 4\pi \imath^{l-u-s} h_s^2(kR) Y_{st}^*(\hat{R}) \int Y_{lm} Y_{st} Y_{uv}^* d\hat{r}. \end{aligned} \tag{2.40}$$

Using these results the relevant Green functions may be written as,

$$\begin{aligned} G_o(\mathbf{r}, \mathbf{r}_1) &= -\imath k \sum_{lm} e^{\imath\delta_l} h_l^1(kr) Y_{lm}(\hat{r}) Y_{lm}^*(r_j \hat{+} x) \times \\ &\qquad \left(e^{\imath\delta_l} h_l^1(k(r_j + x)) + e^{-\imath\delta_l} h_l^2(k(r_j + x)) \right) \\ &= -\imath k \sum_{lm} e^{\imath\delta_l} h_l^1(kr) Y_{lm}(\hat{r}) \sum_{uv} j_u(kx) \left(e^{\imath\delta_l} B_{lmuv} + e^{\imath\delta_l} B^{(2)}_{lmuv} \right) Y_{uv}(\hat{x}), \end{aligned} \tag{2.41}$$

and,

$$G(\mathbf{r}_2, \mathbf{r}') = -\imath k \sum_{lm} e^{\imath\delta_l} \sum_{uv} B_{lmuv} j_u(ky) Y_{uv}(\hat{y}) R_l(kr') Y_{lm}^*(\hat{r'}). \tag{2.42}$$

If we now expand the T-matrix in an angular momentum sum,

$$T(\mathbf{r}_1, \mathbf{r}_2) = \sum_{lm} t_{lm}(x, y) Y_{lm}(\hat{x}) Y^*_{lm}(\hat{y}), \tag{2.43}$$

we can immediately perform the implied integrations over **x** and **y** in equation (2.38) using results from standard electron scattering theory. The integrals over $\hat{x}$ and $\hat{y}$ are simply the orthogonality relations for the spherical harmonics, and, using results from Messiah [30] we can write the integral over the T-matrix as,

$$\int_o^{r_{mt}} j_l(kx) t_{lm}(x, y) j_l(ky) x^2 y^2 dx dy = \frac{1}{4\imath k} \left[1 - e^{2\imath\delta_l}\right]. \tag{2.44}$$

Then,

$$\begin{aligned} GTG &= -\imath k \sum_{lm} \sum_{LM} \sum_{uv} h_l^1(kr) e^{\imath\delta_l} R_L(kr') Y_{lm}(\hat{r}) Y^*_{LM}(\hat{r}) \frac{1}{4} \left[e^{2\imath\delta_u} - 1\right] \\ &\quad \times \left\{ B^{(2)*}_{lmuv} B_{LMuv} e^{\imath(\delta_l + \delta_L)} + B^*_{lmuv} B_{LMuv} e^{\imath(\delta_l - \delta_L)} \right\}. \end{aligned} \tag{2.45}$$

Equation (2.45) may be used to develop the exact curved wave theory of EXAFS first derived by Gurman *et al* [22, 23]. To simplify the algebra however, we shall make the so called plane wave approximation. In this approximation we assume that the atomic separation, r_j, is large and replace the spherical Hankel functions in equation (2.40) with their asymptotic forms. Then, using the standard relations from Brink and Satchler [29] that,

$$Y_{a\alpha}(\hat{R}) Y_{b\beta}(\hat{R}) = \sum_c Y_{c\gamma}(\hat{R}) \int Y_{a\alpha} Y_{b\beta} Y^*_{c\gamma} d\hat{r}, \tag{2.46}$$

and,

$$Y_{lm}(-\hat{R}) = (-1)^l Y_{lm}(\hat{R}), \tag{2.47}$$

we can write the expansion coefficients in equation (2.40) as,

$$\begin{aligned} B_{lmuv} &= 4\pi \imath^{l-u-1} \frac{1}{kr_j} e^{\imath k r_j} Y_{lm}(-\hat{R}) Y_{uv}(-\hat{R}) \\ B^{(2)}_{lmuv} &= 4\pi \imath^{l-u+1} \frac{1}{kr_j} e^{-\imath k r_j} Y_{lm}(\hat{R}) Y_{uv}(\hat{R}). \end{aligned} \tag{2.48}$$

We can substitute these results into equation (2.45) for GTG. Then, summing over all the j scattering atoms in the single shell considered and averaging over the angular positions of this single shell of scattering atoms we find that the perturbed Green function again has the same functional form as $G_o(\mathbf{r},\mathbf{r}')$,

$$G+GTG = -ik\sum_l h_l^1(kr)R_l(kr')e^{i\delta_l}Y_{lm}^*(\hat{r})Y_{lm}(\hat{r'})\left\{1-\sum_j \frac{i(-1)^l}{2kr_j^2}e^{2i(kr_j+\delta_l)}f_j(k,\pi)\right\}$$
$$= \sum_l h_l^1(kr)R_l(kr')e^{i\delta_l}Y_{lm}^*(\hat{r})Y_{lm}(\hat{r'})(1-Z_l), \qquad (2.49)$$

where Z_l is obviously the second term in the curly brackets and we have introduced a result for the backscattering factor,

$$f_j(k,\pi) = -\frac{2\pi}{ik}\sum_{uv}(1-e^{2i\delta_l})Y_{uv}(\hat{R})Y_{uv}^*(-\hat{R}) = |f_j(k,\pi)|e^{i\psi}. \qquad (2.50)$$

We have also ignored a contribution from the forward scattering factor, $f_j(k,0)$, which is second order in the EXAFS.

Using equation (2.49) for $G+GTG$ we may evaluate the photoelectron wavefunction and hence the photoelectron flux far from the central atom. To first order in $1/(kr_j^2)$ we find,

$$S = \frac{kE_o^2}{6}\sum_l A(l,l_o)|\langle R_l|r|\phi_{l_o}\rangle|^2\Big(1+2Re(Z_l)\Big). \qquad (2.51)$$

This expression for the photoelectron flux may again be converted into a result for the X-ray absorption coefficient. Then, substituting for Z_l and for the atomic absorption coefficient from equation (2.27), we obtain the usual result for $\mu(\omega)$,

$$\mu(\omega) = \mu_o(\omega)\left\{1+\sum_j \frac{(-1)^l}{kr_j^2}|f_j(k,\pi)|sin(2kr_j+2\delta_l+\psi)\right\}. \qquad (2.52)$$

The EXAFS function, $\chi(k)$, is defined by $\mu = \mu_o(1+\chi)$ from equation (1.1). Thus, in the plane wave approximation, the EXAFS is simply given by the second term in the curly brackets in equation (2.52), $\chi = 2Re(Z_l)$. This result is equivalent to equation (1.3).

2.3.2 A Complex Scattering Potential

In principle we could obtain a result for the EXAFS in the presence of an imaginary potential by perturbing the Green function and the T-matrix in the same way as in section 2.2.2. This method however, quickly becomes very complex and cumbersome. Instead we choose to examine the effect of the imaginary potential on the phase-shifts.

We perturb the Green function $G_o(\mathbf{r},\mathbf{r}')$ using equation (2.29). The perturbed Green function always has the same functional form as G_o whether or not $\mathbf{r}$ and $\mathbf{r}'$ are inside or outside the muffin tin. Using the same arguments as in section 2.2.2 we can see that, for $\mathbf{r}$ and $\mathbf{r}'$ outside the muffin tin the Green function will simply be multiplied by a factor $(1-\frac{1}{2}k\langle R_l|V_I|R_l\rangle)$ whilst with either $\mathbf{r}$ or $\mathbf{r}'$ or both inside the muffin tin the perturbed Green function can be written as $G_o(1-\frac{1}{2}k\langle R_l|V_I|R_l-\imath X_l\rangle)$. We shall see later that the $\imath\langle R_l|V_I|X_l\rangle$ term may be ignored. However, for the moment including this term, we may rewrite equation (2.31) for the perturbed Green function as,

$$G_1(\mathbf{r},\mathbf{r}') = -\imath k\sum_{l,m} e^{\imath\delta_l'} h_l^{(1)}(kr)Y_{lm}^*(\hat{r})R_l(kr')Y_{lm}(\hat{r}'), \tag{2.53}$$

where we have subsumed the factor $(1-\frac{k}{2}\langle R_l|V_I|R_l-\imath X_l\rangle)$ into the phase-shifts making δ_l complex. In equation (2.53) δ_l' is the perturbed phase-shift. To first order,

$$\delta_l' \approx \delta_l - \frac{1}{2}\langle R_l|V_I|R_l-\imath X_l\rangle. \tag{2.54}$$

This is of course an approximate form for the perturbed phase-shifts, however, using this form we can reproduce equation (2.33) for the loss of flux from an isolated atom. We therefore believe that this approximation is a good one.

Using result (2.54) for the perturbed phase-shifts we may easily calculate the EXAFS in the presence of the imaginary potential by following the same

derivation as in the previous section. From equation (2.51) we can see the effect on the EXAFS of perturbing the phase-shifts. We can also calculate the elastic contribution to the absorption coefficient. Writing the perturbed backscattering factor as $f_j'(k,\pi)$ we have,

$$\mu_{el} = \mu_o(1 - k\langle R_l|V_I|R_l\rangle)\left\{1 + 2Re\sum_j \frac{i(-1)^l}{2kr_j^2} e^{2\imath(kr_j+\delta_l')} f_j'(k,\pi)\right\}. \tag{2.55}$$

Then, because the total absorption must be the same regardless of whether or not there is an imaginary part to the potential we may write the total X-ray absorption coefficient as,

$$\mu_{tot} = \mu = \mu_{el}(1-\chi) + \mu_{inel}, \tag{2.56}$$

which gives the EXAFS as,

$$\chi = (1 - 2k\langle R_l|V_I|R_l\rangle)\frac{(-1)^l}{kr_j^2} sin(2kr_j + 2\delta_l + \psi)|f_j'(\pi)|. \tag{2.57}$$

The perturbed backscattering factor may be written as,

$$f_j'(k,\pi) = \frac{\imath}{2k}\sum_L (-1)^L(2L+1)\left(1 - (1 - k\langle R_L|V_I|R_L\rangle)e^{\imath(\delta_L - \langle R_L|V_I|X_L\rangle)}\right). \tag{2.58}$$

The irregular solution to the Schrödinger equation only appears in the exponential in the above equation. It merely alters the phase of the backscattering factor, $f_j'(k,\pi)$. However, compared to the phase-shifts, the radial matrix element $\langle R_L|V_I|X_L\rangle$ is always small. In Chapter 4 we shall see that V_I is approximately constant over much of the region of the atom. Thus, because R_L and X_L are orthogonal the matrix element $\langle R_L|V_I|X_L\rangle$ must be small. In Chapter 4 we compare $\langle R_L|V_I|X_L\rangle$ to the phase-shifts δ_L and show that, in comparison to the phase-shifts, the radial matrix element, $\langle R_L|V_I|X_L\rangle$, may be ignored.

Thus, in the presence of an imaginary part to the potential the EXAFS amplitude is given to first order in V_I by,

$$A_l = 1 - 2k\langle R_l|V_I|R_l\rangle \left|\frac{f_j'(\pi)}{f_j(\pi)}\right|. \tag{2.59}$$

This expression may be used to calculate the amplitude of the EXAFS in the presence of an imaginary potential designed to account for the inelastic electron-electron scatterings. In Chapter 4 we use the above equation to examine the magnitude of the EXAFS when the Hedin-Lundqvist [9] potential is used to model the many-electron effects of exchange and correlation. Equation (2.59) may also be obtained by perturbing the scattering wavefunctions (eqn.(2.5)) rather than the photoelectron wavefunction [33].

2.4 Conclusion

In this Chapter we have developed expressions for the X-ray absorption coefficient and the EXAFS by considering the photoelectron flux produced by irradiating an atom with a beam of X-ray photons. We have examined the effect on the amplitude of the EXAFS and the elastically scattered flux of introducing an effective imaginary part of the potential to describe inelastic electron-electron scatterings. The results derived here will be used in Chapters 4 and 5 to evaluate the X-ray absorption coefficient and the losses to the elastic photoelectron flux caused by various types of imaginary potential.

Chapter 3

The Self-Energy and the Dielectric Function

In this chapter we investigate some of the theory underlying the approximation of many-electron effects in EXAFS. We begin with a short review of some of the approximations used in many-body physics. We then discuss the role of screening and outline the derivation of the non-local self energy operator. We also derive expressions for the Hartree inverse dielectric function, the quantity which defines the screening. Numerical results for the local inverse dielectric function are calculated for both a free electron gas and an atomic system. The results of the atomic calculation are then equated to the single electron X-ray absorption coefficient.

3.1 Many-Body Physics

Many-body interactions play an important role in electron-electron scattering problems such as EXAFS. Historically a great deal of effort has been put into solving the Hamiltonian for a many-electron system,

$$H = \sum_i \left[-\frac{1}{2}\nabla^2(\mathbf{r}_i) + V(\mathbf{r}_i) \right] + \frac{1}{2}\sum_{i \neq j} \frac{1}{|\mathbf{r}_i - \mathbf{r}_j|}. \tag{3.1}$$

For a small number of electrons it is possible to obtain a very accurate representation of the ground state wavefunction using the configuration

interaction method [34]. However, the computational effort scales exponentially with the size of the system [35]. Also, for excited states the computational effort becomes large even for small systems. Thus, using the CI method for EXAFS calculations is impractical. Instead we must approximate the ground and excited state wavefunctions in some other fashion.

Approximate theories are usually concerned with finding a good single particle approximation for the coulomb term. The earliest of these theories is the Hartree approximation in which the coulomb term is replaced by an average local coulomb potential from all the electrons. The Hartree potential is known to give reasonable results due to a cancellation between exchange and correlation but is not accurate enough for many applications.

An extension of the Hartree approximation, which takes into account the fermionic nature of the electrons, is the Hartree-Fock theory where, in addition to the local coulomb potential, there is a non-local exchange potential which reflects the Pauli exclusion principle. The Hartree-Fock approximation works quite well for atoms and insulating solids but is poor in conducting solids due to the neglect of electron correlations. In the Hartree-Fock approximation only electrons of equivalent spins are forbidden from occupying the same state. In reality, however, the coulomb interaction between electrons will keep even electrons of opposite spins apart. The correlations keep electrons away from each other, creating a screening hole around each electron which significantly reduces the interaction with the other electrons. Thus, electron-electron correlations and screening are important factors in the many-body problem.

The Slater $X\alpha$ potential [36] was perhaps the first to make an allowance for these effects. In this theory the exchange is approximated by the free electron exchange calculated with a radially varying atomic charge density. Correlation effects are then included empirically by scaling the potential with the variable

parameter α. The Slater $X\alpha$ potential is known to give good results for the ground state but works less well for excited states.

A more accurate way of approximating the coulomb interaction term is through a non-local energy-dependent potential, the electron self-energy. The self-energy is a quantity which can be derived systematically from many-body perturbation theory and which contains the effects of the exchange and correlations. The different single particle theories amount to approximating the self energy in different ways. In its local form, the self-energy simply becomes an effective scattering potential which can be used in the single electron formalism of existing EXAFS theory. The self energy is, in general complex, with the imaginary part describing the inelastic scattering of electrons.

3.2 Screening

The concept of screening is an important one in many-body physics. In a many-electron system a given electron will not, in general, respond directly to an applied external field. Instead the density fluctuations induced by such a field cause an additional potential which tends to screen out some of the effects of the total field. It is to the total field, the sum of the external and induced potentials, that the electrons respond. In classical physics the relationship between the total field and a static external field may be expressed in terms of a dielectric constant,

$$V_{tot} = \frac{V_{ext}}{\epsilon}. \tag{3.2}$$

In many-body physics we generalise the idea of the dielectric constant and write the relation between the total and applied fields in terms of an inverse dielectric function, or response function,

$$V_{tot}(\mathbf{r}_1, \omega) = \int \epsilon^{-1}(\mathbf{r}_1, \mathbf{r}_2, \omega) V_{ext}(\mathbf{r}_2, \omega) d\mathbf{r}_2, \tag{3.3}$$

where, in general, the applied field may be energy-dependent and the response of the system non-local.

The inverse dielectric function serves as a single unifying concept for many of the properties of an interacting system of electrons. Not only does it give the response of the system to an external field but it also contains information on both the single particle and collective modes of the energy-dependent density-fluctuation spectrum. The inverse dielectric function is also important when it comes to calculating such quantities as the self-energy which are obtained by summing over all the possible coulomb interactions. The screening reduces the effect of the coulomb interaction at long range ensuring that the series of terms involving the interaction converge more rapidly.

In this chapter we work under the random phase approximation, also known as the linearised time-dependent Hartree approximation. This simply means that we assume the electrons to respond to the total field, the sum of the applied and induced potentials, as non interacting particles. Each electron feels a certain coulomb potential from a given electron, this potential will be screened in some fashion due to the fluctuations in electronic density caused by the original potential, giving a new average field. We then assume each of the remaining electrons to behave as non interacting particles responding to the new average potential.

3.3 The Self-Energy

To account for the interaction between a given electron and the rest of the electrons in the system we must generalise the notion of a local potential and introduce a non-local time, or energy, dependent potential. This non-local potential, known as the self-energy, contains the exchange and correlation

effects. It is, in general, complex with the imaginary part describing the inelastic scattering between single particle states.

The full Green function for an arbitrary many-electron system may be written in terms of the non-local, energy-dependent potential, $\Sigma(\mathbf{r}_1, \mathbf{r}_2, \omega)$ [9],

$$(\omega - H(\mathbf{r}_1) - V(\mathbf{r}_1))G(\mathbf{r}_1, \mathbf{r}_2, \omega) - \int \Sigma(\mathbf{r}_1, \mathbf{r}_3, \omega)G(\mathbf{r}_3, \mathbf{r}_2, \omega)d\mathbf{r}_3 = \delta(\mathbf{r}_1, \mathbf{r}_2). \quad (3.4)$$

Where, $V(\mathbf{r})$ is the total average potential in the system. This is the sum of the Hartree potential plus any external field. The Hartree and Hartree-Fock approximations for $G(\mathbf{r}_1, \mathbf{r}_2, \omega)$ are obtained from the above equation by specifying that Σ be energy independent. To obtain the Hartree approximation in equation (3.4) we simply set $\Sigma = 0$. Similarly, the Hartree-Fock approximation is obtained by making the choice $\Sigma(\mathbf{r}_1, \mathbf{r}_2) = \frac{i}{2\pi} v(\mathbf{r}_1, \mathbf{r}_2) \int G(\mathbf{r}_1, \mathbf{r}_2, \omega) e^{i\delta\omega} d\omega$.

The self-energy is generally evaluated iteratively from a set of well known integral equations, the Hedin equations [37]. $\Sigma(\mathbf{r}_1, \mathbf{r}_2, \omega)$ can be written in terms of a power series involving the unscreened coulomb interaction, $v(\mathbf{r}_1, \mathbf{r}_2)$ or in a more rapidly converging series in terms of the dynamically screened interaction,

$$W_o(\mathbf{r}_1, \mathbf{r}_2, \omega) = \int \epsilon^{-1}(\mathbf{r}_1, \mathbf{r}_2, \omega) v(\mathbf{r}_3, \mathbf{r}_2) d\mathbf{r}_3. \quad (3.5)$$

W_o is defined in terms of the inverse dielectric function and the unscreened coulomb interaction, $v(\mathbf{r}_1, \mathbf{r}_2) = |\mathbf{r}_1 - \mathbf{r}_2|^{-1}$. Mathematically, using the screened interaction corresponds to summing a selective set of terms in the expansion of Σ in the unscreened interaction to infinite order. Physically we are saying that each electron will not respond to any external potential but rather to the total potential in the system, the sum of the external field and any induced potential due to the response of the system.

A result for the self-energy in the lowest order of the screened interaction is given by Inkson [38]. This is known as the GW approximation for the self-energy and is the simplest working approximation beyond Hartree-Fock that takes

screening into account,

$$\Sigma(\mathbf{r}_1, \mathbf{r}_2, t_1 - t_2) = \imath W_o(\mathbf{r}_1, \mathbf{r}_2, t_1 - t_2) G_o(\mathbf{r}_1, \mathbf{r}_2, t_1 - t_2). \tag{3.6}$$

Where $G_o(\mathbf{r}_1, \mathbf{r}_2, t_1 - t_2)$ is the Hartree Green function, the solution to equation (3.4) with the self-energy set to zero. To obtain relation (3.6) in a more convenient form we must Fourier transform it into energy space. We use the following definition for the Fourier transform,

$$f(\mathbf{r}, t) = \frac{1}{(2\pi)^4} \int d\mathbf{q} d\omega e^{\imath \mathbf{q}\cdot\mathbf{r}} e^{\imath\omega t} f(\mathbf{q}, \omega). \tag{3.7}$$

Thus,

$$\begin{aligned} \Sigma(\mathbf{r}_1, \mathbf{r}_2, \omega) &= \int e^{-\imath\omega(t_1 - t_2)} \Sigma(\mathbf{r}_1, \mathbf{r}_2, t_1 - t_2) d(t_1 - t_2) \\ &= \frac{\imath}{2\pi} \int W_o(\mathbf{r}_1, \mathbf{r}_2, \omega') G_o(\mathbf{r}_1, \mathbf{r}_2, \omega - \omega') d\omega'. \end{aligned} \tag{3.8}$$

From equation (3.5) we may write W_o in Fourier transform,

$$W_o(\mathbf{q}_1, \mathbf{q}_2, \omega) = \epsilon^{-1}(\mathbf{q}_1, \mathbf{q}_2, \omega) v_{\mathbf{q}_2}, \tag{3.9}$$

where $v_{\mathbf{q}} = \frac{4\pi}{|\mathbf{q}|^2}$ and we have used the general result that,

$$\int e^{\imath(\mathbf{q}_1 - \mathbf{q}_2)\cdot\mathbf{r}} d\mathbf{r} = (2\pi)^3 \delta(\mathbf{q}_1 - \mathbf{q}_2). \tag{3.10}$$

Then, substituting for $W_o(\mathbf{q}_1, \mathbf{q}_2, \omega)$ into equation (3.8) for the self-energy we find that,

$$\Sigma(\mathbf{r}_1, \mathbf{r}_2, \omega) = \frac{\imath}{(2\pi)^7} \int \epsilon^{-1}(\mathbf{q}_1, \mathbf{q}_2, \omega') v_{\mathbf{q}_2} G_o(\mathbf{r}_1, \mathbf{r}_2, \omega - \omega') e^{\imath\mathbf{q}_1\cdot\mathbf{r}_1} e^{\imath\mathbf{q}_2\cdot\mathbf{r}_2} d\mathbf{q}_1 d\mathbf{q}_2 d\omega'. \tag{3.11}$$

To proceed further, explicit forms for the Hartree Green function and the inverse dielectric function must be used. The Green function is defined in terms of the solutions to the single electron Schrödinger equation, ϕ_m,

$$G_o(\mathbf{r}_1, \mathbf{r}_2, \omega - \omega') = \sum_m \frac{\phi_m(\mathbf{r}_1)\phi_m^*(\mathbf{r}_2)}{\omega - \omega' - E_m + \imath\delta sign(E_m)}, \tag{3.12}$$

where $sign(E_m) = -1$ if $E_m < 0$ and the one electron states are occupied, whilst $sign(E_m) = 1$ if $E_m > 0$ and the one electron states are unoccupied.

In deriving a result for the self-energy we must use the time ordered response function [9]. This is slightly different to the causal dielectric function encountered in perturbation theory in that the two poles in $\epsilon^{-1}(\mathbf{q}_1, \mathbf{q}_2, \omega)$ are in different half planes. We discuss the inverse dielectric function in more detail in the following section. For the moment we simply quote it as,

$$\epsilon^{-1}(\mathbf{q}_1, \mathbf{q}_2, \omega) = \delta(\mathbf{q}_1 - \mathbf{q}_2) + v_{\mathbf{q}_1} \sum_n \rho_{no}(\mathbf{q}_1)\rho^*_{no}(\mathbf{q}_2) \left\{ \frac{1}{\omega - \omega_{no} + \imath\delta} - \frac{1}{\omega + \omega_{no} - \imath\delta} \right\} \quad (3.13)$$

where $\rho_{no}(\mathbf{q})$ is the matrix element of the density operator between the exact ground state and a many-body excited state of the system and ω_{no} is the difference in energy between the system in the ground state and in the 'n'th excited state.

Using the definitions of $G_o(\mathbf{r}_1, \mathbf{r}_2, \omega - \omega')$ and $\epsilon^{-1}(\mathbf{q}_1, \mathbf{q}_2, \omega)$ we can immediately perform the ω' integral in equation (3.11) using contours. Following Inkson [38] we add a convergence factor of $e^{-\imath\omega'\delta}$ to the integral and close contours in the lower half of the complex plane. We then obtain a contribution to the self energy from the pole in the inverse dielectric function at $\omega' = \omega_{no} - \imath\delta$ and from the pole in the Green function at $\omega' = \omega - E_m - \imath\delta$. The pole in the Green function only contributes if $\phi_m(\mathbf{r})$ is an occupied state with $E_m < 0$. Then,

$$\begin{aligned} \Sigma(\mathbf{r}_1, \mathbf{r}_2, \omega) &= \frac{-1}{(2\pi)^6} \int e^{\imath\mathbf{q}_1\cdot\mathbf{r}_1} e^{\imath\mathbf{q}_2\cdot\mathbf{r}_2} v_{\mathbf{q}_2} \left\{ \sum_m^{occ} \phi_m(\mathbf{r}_1)\phi^*_m(\mathbf{r}_2)\epsilon^{-1}(\mathbf{q}_1, \mathbf{q}_2, \omega - E_m) \right. \\ &+ \left. v_{\mathbf{q}_1} \sum_n G_o(\mathbf{r}_1, \mathbf{r}_2, \omega - \omega_{no})\rho_{no}(\mathbf{q}_1)\rho^*_{no}(\mathbf{q}_2) \right\} d\mathbf{q}_1 d\mathbf{q}_2. \end{aligned} \quad (3.14)$$

The terms obtained from the contribution of the two poles each have a different physical meaning.

The pole in the Green function gives rise to the dynamically screened exchange term. This reduces to the Hartree-Fock exchange if we take the screened

interaction to be simply the bare coulomb term, $W_o(\mathbf{r}_1, \mathbf{r}_2) = v(\mathbf{r}_1, \mathbf{r}_2)$. The screened exchange term is much better behaved than the normal Hartree-Fock exchange which is known to give unphysical results for the density of states in solids.

The pole in $\epsilon^{-1}(\mathbf{q}, \omega)$ produces a term which can be associated with the coulomb hole and which describes the electron-electron correlation. Classically the coulomb hole has a simple physical interpretation. Electrons will correlate their motion so as to screen out the electric field at large distances. In a uniform electron gas each electron will be surrounded by a hole in the electronic density which contains an equal and opposite charge. Thus at large distances the coulombic effects of each electron with its surrounding hole are negligible.

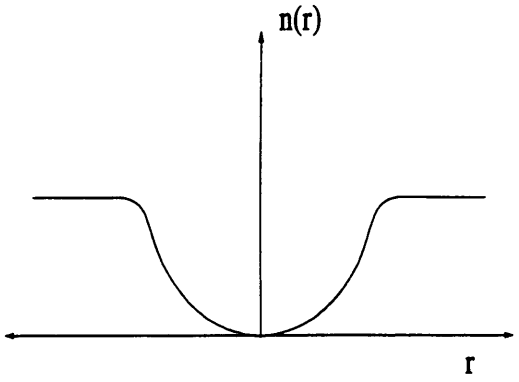

Figure 3.1: Schematic representation of the coulomb-induced hole in the electronic density ($n(\mathbf{r})$). Reproduced from figure 1.3 of Inkson [38].

Equation (3.14) is a general result for the self-energy to the lowest order in the dynamically screened interaction, $W_o(\mathbf{r}_1, \mathbf{r}_2, \omega)$. To make this result easily applicable to EXAFS theory it is advantageous to write Σ in a local rather than non-local form. We shall do this in the following two chapters in which we investigate two different approximations for the exchange and correlation potential.

3.4 The Inverse Dielectric Function

The result for $\Sigma(\mathbf{r}_1, \mathbf{r}_2, \omega)$ obviously depends on the exact form chosen for the screening. In this section we shall examine two forms in particular for the inverse dielectric function. We derive expressions for the response function within the Hartree approximation and calculate numerical results for the local inverse dielectric function in an atomic system and for a uniform electron gas. The calculation of the inverse dielectric function in a free electron gas is standard and can be found in, for example, March and Jones [39], and Pines [40]. We outline the standard derivation then apply the free electron gas relations within a local density formalism to calculate the response function for systems of varying charge density. This is the form of the inverse dielectric function used in the Hedin-Lundqvist calculation of the self-energy in Chapter 4.

To our knowledge a calculation of $\epsilon^{-1}(\mathbf{q}, \omega)$ using atomic wavefunctions has not been performed, although an atomic dielectric function is used, at least implicitly, in the work on complex potentials by Beni, Lee and Platzman [17].

Results for the dielectric function, especially those pertaining to a uniform electron gas, are usually evaluated using perturbation theory (see for example, Ziman [41], Pines [40], Nozieres [42]). This approach gives rise to the causal or retarded response function. However, when evaluating the self-energy we must use the time ordered inverse dielectric function [9]. Both response functions are equal for positive energies but the time ordered function is an even function of the energy whilst the retarded dielectric function has an even real part and an odd imaginary part.

Hedin and Lundqvist [9] define the time ordered inverse dielectric function in terms of a response function, $R(\mathbf{r}_1, \mathbf{r}_2, \omega)$,

$$\epsilon^{-1}(\mathbf{r}_1, \mathbf{r}_2, \omega) = \delta(\mathbf{r}_1 - \mathbf{r}_2) + \int d\mathbf{r}_3 v(\mathbf{r}_1, \mathbf{r}_3) R(\mathbf{r}_3, \mathbf{r}_2, \omega). \tag{3.15}$$

The response function is given by,

$$R(\mathbf{r_3}, \mathbf{r_2}, \omega) = \sum_n \rho_{no}(\mathbf{r}_1)\rho^*_{no}(\mathbf{r}_2)\left[\frac{1}{\omega - \omega_{no} + \imath\delta} - \frac{1}{\omega + \omega_{no} - \imath\delta}\right], \tag{3.16}$$

where,

$$\rho_{no}(\mathbf{r}) = \langle \Phi_o^N(\mathbf{r}_a..\mathbf{r}_N)|\boldsymbol{\rho}(\mathbf{r})|\Psi_n^N(\mathbf{r}_a...\mathbf{r}_N)\rangle. \tag{3.17}$$

$|\Phi_o^N(\mathbf{r}_a..\mathbf{r}_N)\rangle$ and $|\Psi_n^N(\mathbf{r}_a...\mathbf{r}_N)\rangle$ are the exact N-body ground and excited states for the system whilst $\omega_{no} = \omega_n - \omega_o$ is the difference between the excited and ground state energies. $\boldsymbol{\rho}(\mathbf{r})$ is the density operator. If we assume the electrons to be point particles then the density operator may be simply written as,

$$\boldsymbol{\rho}(\mathbf{r}) = \sum_i \delta(\mathbf{r} - \mathbf{r}_i), \tag{3.18}$$

or, in Fourier transform as,

$$\boldsymbol{\rho}(\mathbf{q}) = \sum_i e^{-\imath\mathbf{q}\cdot\mathbf{r}_i}, \tag{3.19}$$

where the sum over i runs over all the electronic coordinates.

In section 3.3 we used a result for the inverse dielectric function in q and ω space. Equation (3.13) is simply obtained by substituting for the response function into equation (3.15) and Fourier transforming. Equation (3.13) is a general result for the time ordered response function. In order to calculate it numerically we must make some simplifying approximations. First, we assume the exact ground state and excited state wavefunctions to be Hartree products of single electron orbitals,

$$\begin{aligned} |\Phi_o^N\rangle &= \prod_{i=1}^{N} |\phi_i(\mathbf{r}_i)\rangle \\ |\Psi_n^N\rangle &= |\psi_n(\mathbf{r}_j)\rangle \prod_{i\neq j}^{N} |\phi_i(\mathbf{r}_j)\rangle, \end{aligned} \tag{3.20}$$

where the $|\phi_j(\mathbf{r}_j)\rangle$'s are bound single electron orbitals and $|\psi_n(\mathbf{r}_j)\rangle$ is an excited single electron state. In the Hartree approximation, the only many-body excited states which can be reached are those with at most a single electron in an excited

state. Also, in the Hartree approximation, each electron is identifiable, thus, choosing the electron to be excited to have a particular radial coordinate, $\mathbf{r}_j$, and noting that the initial and final state wavefunctions are orthogonal we may write the matrix element of the density operator as,

$$\begin{aligned}\rho_{no}(\mathbf{q}) &= \langle\Phi_o(\mathbf{r}_a..\mathbf{r}_N)|\sum_i e^{\imath\mathbf{q}\cdot\mathbf{r}_i}|\Psi_n(\mathbf{r}_a...\mathbf{r}_N)\rangle \\ &= \langle\phi_o(\mathbf{r})|\rho_{\mathbf{q}}|\psi_n(\mathbf{r})\rangle, \end{aligned} \tag{3.21}$$

where $\rho_{\mathbf{q}} = exp(-\imath\mathbf{q}\cdot\mathbf{r})$.

Thus, substituting this result into equation (3.13) for the inverse dielectric function we find that the Hartree inverse dielectric function is given by,

$$\begin{aligned}\epsilon^{-1}(\mathbf{q}_1,\mathbf{q}_2,\omega) &= \delta(\mathbf{q}_1-\mathbf{q}_2)+v_{\mathbf{q}_1}\sum_n\langle\phi_o(\mathbf{r})|\rho_{\mathbf{q}_1}|\psi_n(\mathbf{r})\rangle\langle\psi_n(\mathbf{r})|\rho^*_{\mathbf{q}_2}|\phi_o(\mathbf{r}))\rangle \\ &\quad\times\left\{\frac{1}{\omega-\omega_{no}+\imath\delta}-\frac{1}{\omega+\omega_{no}-\imath\delta}\right\}. \end{aligned} \tag{3.22}$$

3.4.1 The Local Inverse Dielectric Function

Most calculations assume the inverse dielectric function to be local. This is equivalent to simply ignoring the off diagonal elements in $\epsilon^{-1}(\mathbf{q}_1,\mathbf{q}_2,\omega)$. In a uniform electron gas this approximation is, of course, exact, as the system is translationally invariant.

Taking the diagonal elements of equation (3.22), the local inverse dielectric function is found to be,

$$\epsilon^{-1}(\mathbf{q},\omega) = 1+v_{\mathbf{q}}\sum_n|\langle\psi_n(\mathbf{r})|\rho^*_{\mathbf{q}}|\phi_o(\mathbf{r})\rangle|^2\left\{\frac{1}{\omega-\omega_{no}+\imath\delta}-\frac{1}{\omega+\omega_{no}-\imath\delta}\right\}. \tag{3.23}$$

It is instructive to examine the real and imaginary parts of the above equation separately. With the help of the formal identity,

$$\lim_{\delta\to0}\frac{1}{x\pm\imath\delta} = P\left(\frac{1}{x}\right)\mp\imath\pi\delta(x), \tag{3.24}$$

we find that the real and the imaginary parts of the inverse dielectric function are given by,

$$Re\,\epsilon^{-1}(\mathbf{q},\omega) = 1 + v_{\mathbf{q}} \sum_n |\langle\psi_n|\rho^*_{\mathbf{q}}|\phi_o\rangle|^2 \left\{\frac{2\omega_{no}}{\omega^2 - \omega_{no}^2}\right\}, \tag{3.25}$$

$$Im\,\epsilon^{-1}(\mathbf{q},\omega) = -\pi v_{\mathbf{q}} \sum_n |\langle\psi_n|\rho^*_{\mathbf{q}}|\phi_o\rangle|^2 \left\{\delta(\omega - \omega_{no}) - \delta(\omega + \omega_{no})\right\}. \tag{3.26}$$

The real part of $\epsilon^{-1}(\mathbf{q},\omega)$ describes polarisation processes in phase with the external field whilst the imaginary part represents the out of phase part and is related to the transfer of energy between parts of the system.

Equations (3.25) and (3.26) can be used to calculate the Hartree inverse dielectric function in a number of different systems. We shall begin by outlining the derivation in a free electron gas.

3.4.2 Free Electron Gas Calculation of $\epsilon^{-1}(q,\omega)$

In the uniform electron gas the electronic wavefunctions are simply plane waves,

$$\begin{aligned} |\phi_o(r)\rangle &= \exp(\imath\mathbf{k}\cdot\mathbf{r}), \\ |\psi_n(r)\rangle &= \exp(\imath\boldsymbol{\kappa}\cdot\mathbf{r}). \end{aligned} \tag{3.27}$$

Substituting these states into the result for the local inverse dielectric function we obtain the result that,

$$\begin{aligned} \epsilon^{-1}(\mathbf{q}\,\omega) = 1 + v_{\mathbf{q}} \sum_{\boldsymbol{\kappa}} \left| \int e^{-\imath\boldsymbol{\kappa}\cdot\mathbf{r}} \exp(\imath\mathbf{q}\cdot\mathbf{r}) e^{\imath\mathbf{k}\cdot\mathbf{r}} d\mathbf{r} \right|^2 \\ \times \left\{ \frac{1}{\omega - \omega_{\boldsymbol{\kappa}} + \omega_{\mathbf{k}} + \imath\delta} - \frac{1}{\omega + \omega_{\boldsymbol{\kappa}} - \omega_{\mathbf{k}} - \imath\delta} \right\}. \end{aligned} \tag{3.28}$$

The radial integral gives a delta function, $\delta(\mathbf{q}+\mathbf{k}-\boldsymbol{\kappa})$, which removes the sum over final states, $\boldsymbol{\kappa}$. Equation (3.28) is the contribution to the inverse dielectric function from a single initial state only. The total inverse dielectric function is

obtained by summing over all the occupied plane wave initial states in the uniform electron gas. We ensure that no unoccupied states are included by multiplying the summation term by the Fermi occupation function, $n_{\mathbf{k}}$,

$$\epsilon^{-1}(\mathbf{q}\,\omega) = 1 + v_{\mathbf{q}} \sum_{\mathbf{k}} n_{\mathbf{k}} \left\{ \frac{1}{\omega + \omega_{\mathbf{k}} - \omega_{\mathbf{k}+\mathbf{q}} + i\delta} - \frac{1}{\omega + \omega_{\mathbf{k}+\mathbf{q}} - \omega_{\mathbf{k}} + i\delta} \right\}. \quad (3.29)$$

To obtain the standard Lindhard form from equation (3.29) we must change summation variables in the first term on the right hand side. We initially replace $\mathbf{k}$ by $\mathbf{k}' = \mathbf{k}+\mathbf{q}$, then switching between $\mathbf{k}$' and -$\mathbf{k}$' in the infinite summation and remembering that the occupation number and state energies must be independent of the sign of the wave vector we can write,

$$\epsilon^{-1}(\mathbf{q}\,\omega) = 1 + v_{\mathbf{q}} \sum_{\mathbf{k}} \frac{n_{\mathbf{k}+\mathbf{q}} - n_{\mathbf{k}}}{\omega + \omega_{\mathbf{k}+\mathbf{q}} - \omega_{\mathbf{k}} + i\delta}. \quad (3.30)$$

This result is equivalent to the first order expansion of the Lindhard result for $\epsilon(q,\omega)$ [9]. In equation (3.30) $\epsilon^{-1}(\mathbf{q}\,\omega)$ is identically equal to one unless $|\mathbf{k}| > \mathbf{k}_f$ and $|\mathbf{k}+\mathbf{q}| < \mathbf{k}_f$ or $|\mathbf{k}| < \mathbf{k}_f$ and $|\mathbf{k}+\mathbf{q}| < \mathbf{k}_f$. Contributions to the summation term only arise from excitations across the Fermi surface.

In equations (3.30) and (3.29) the sum of $\mathbf{k}$ may be replaced by an integral $d\mathbf{k}/(2\pi)^3$. The integral in equation (3.29) is actually easiest to perform and may be evaluated analytically to produce a result first obtained by Lindhard [43]. The Lindhard form is, however, too complex to be of use in most practical situations and is therefore usually approximated in some form or other.

One commonly used approximation is the single plasmon pole (SPP) form of Hedin and Lundqvist [9],

$$\epsilon^{-1}(\mathbf{q},\omega) = 1 + \frac{\omega_p^2}{2\omega_q} \left[\frac{1}{\omega - \omega_q + i\delta} - \frac{1}{\omega + \omega_q - i\delta} \right]. \quad (3.31)$$

In equation (3.31) ω_p is the plasma frequency, given by $\omega_p^2 = 4\pi n$ where the electron density $n = k_f^3/3\pi^2$ in a uniform electron gas. The plasma oscillation

frequency at a wave vector **q** is denoted by ω_q. This can be obtained from the real part of the Lindhard expression (eqn.(3.29)). In the high frequency limit we can expand the real part of equation (3.29) to second order in $(\omega_{\mathbf{k+q}} - \omega_q)^2/\omega^2$. This gives an expression which may be integrated and compared to the real part of the SPP form for ϵ^{-1} to obtain an expression for ω_q. Hedin and Lundqvist [9] use a q dependent plasmon frequency with a slightly different numerical coefficient for the q^2 term than that obtained from the Lindhard formula,

$$\omega_q^2 = \omega_p^2 + \frac{1}{3}q^2{k_f}^2 + \frac{1}{4}q^4, \tag{3.32}$$

At large q, ω_q approaches the free particle limit of $\frac{1}{2}q^2$ whilst, in the small wavelength limit, ω_q reduces to ω_p so that equation (3.31) reproduces the familiar Drude relation for the optical dielectric function,

$$\epsilon^{-1}(0\,\omega) = 1 + \frac{\omega_p^2}{\omega^2 - \omega_p^2}. \tag{3.33}$$

The imaginary part of the SPP inverse dielectric function for positive frequencies is modelled using a single delta function. This gives a sharp plasmon like absorption for all **q** but contains no contribution from particle-hole excitations. The single plasmon pole form does, however, satisfy the same sum rule [9] as the Lindhard inverse dielectric function. Thus, in the single plasmon pole approximation we have assumed that all the weight in $Im\epsilon^{-1}$ resides in the plasmon excitations. This is strictly true in the long wavelength limit. Also, in the small **q** limit, the real part of the SPP response function and the full Lindhard dielectric function are almost identical although at shorter wavelengths the two forms begin to diverge.

3.4.3 LDA of an Average Single Plasmon Pole $\epsilon^{-1}(q,\omega)$.

In the local density approximation (LDA) it is assumed that an atomic system may be described solely in terms of its electronic density. Each volume element

of the atom is taken to respond to the total field as if it were part of an infinite uniform electron gas of the same density. In this way we may apply homogeneous electron gas relations locally simply by replacing the constant charge density, n, with a radially varying function $n(r)$. Thus, within the LDA, we can calculate $\epsilon^{-1}(q,\omega)$ as a function of r for a particular atom, provided we know how the charge density varies radially within that atom.

In the local density approximation both the plasma frequency, ω_p, and ω_q are functions of r. We invoke the usual muffin tin approximation in which the charge density is taken to be spherically symmetric. Thus, after spherically averaging both the local plasma frequency and the charge density, we find we can write the ω_p in terms of the radial atomic wavefunctions, $\phi_i(r)$, $\omega_p^2(r) = \sum_i |\phi_i(r)|^2$. Using this result we can calculate an inverse SPP dielectric function which is dependent on q, r and ω. Averaging this function over r will then produce an LDA calculation of $\epsilon^{-1}(q,\omega)$ directly comparable to the atomic calculation and to experiment.

For the imaginary part of $\epsilon^{-1}(q,\omega)$ we have,

$$\begin{aligned} Im\,\epsilon^{-1}(q,\omega) &= \int d\mathbf{r} Im\,\epsilon^{-1}(q,\omega,r) \\ &= \int 4\pi r^2 dr \frac{\pi\omega_p^2(r)}{2\omega_q(r)} \delta\left(\omega - \omega_q(r)\right), \end{aligned} \tag{3.34}$$

where we have substituted for $Im\,\epsilon^{-1}(q,\omega r)$ using the imaginary part of equation (3.31) for positive frequencies and normalised to unit volume. Then, rewriting the delta function using a standard result from Messiah [30],

$$\delta\left(\omega - \omega_q(r)\right) = \left[\frac{d\omega_q(r)}{dr}\right]^{-1} \delta(r - r_q), \tag{3.35}$$

it follows that,

$$Im\,\epsilon^{-1}(q,\omega) = 2\pi^2 \int r^2 \frac{\omega_p^2(r)}{\omega} \left[\frac{d\omega_q(r)}{dr}\right]^{-1} \delta(r - r_q) dr, \tag{3.36}$$

where r_q is the radius at which the q dependent plasma frequency is equal to the frequency of the perturbation, ω. Equation (3.36) gives an expression describing $\epsilon^{-1}(q,\omega)$ in a system of varying atomic density obtained obtained using the free electron gas relations and the LDA. Using an atomic charge density to describe ω_p we can directly compare equation (3.36) to a more sophisticated atomic calculation and to experiment.

3.4.4 Atomic Calculation of $\epsilon^{-1}(q,\omega)$

The Imaginary Part

We wish to calculate the imaginary part of the inverse dielectric function for an atomic system which we assume to be initially in the ground state. In this case the energy difference between final and initial states, ω_{no}, will always be positive and hence the second of the delta functions in equation (3.26) will give no contribution to $Im\,\epsilon^{-1}(\mathbf{q}\omega)$. It is also well known that continuum transitions are much more likely than those into bound states [12], thus, in the sum over excited states, $|\psi_n\rangle$, we concentrate only on propagating states in the continuum. This enables us to replace the sum over final states by an integral over the free electron density of states in the usual fashion. We may rewrite equation (3.26) as,

$$Im\,\epsilon^{-1}(\mathbf{q},\omega) = -\frac{\pi v_{\mathbf{q}}}{(2\pi)^3}\int d\mathbf{k}|\langle\psi(\mathbf{k},\mathbf{r})|\rho^*_{\mathbf{q}}|\phi_o(\mathbf{r})\rangle|^2\delta\left(\omega - |\omega_o| - \frac{1}{2}k^2\right). \quad (3.37)$$

Equation (3.37) gives the contribution to the imaginary part of the dielectric function from a single initial state. The total imaginary part of the dielectric function for a particular atomic system is therefore obtained by summing the right hand side of equation (3.37) over all the occupied initial states.

As in the previous chapter, we write the continuum final states as a sum of phase-shifted radial solutions to the Schrödinger equation multiplied by the

relevant spherical harmonics (eqn.(2.5)). This enables us to perform the angular part of the **k** integral in equation (3.37) immediately,

$$Im\,\epsilon^{-1}(\mathbf{q},\omega) = \frac{1}{2}\sum_{i,l_f,m_f,} \int |\langle R_{l_f} Y_{l_f m_f}(\hat{r})|\rho^*_{\mathbf{q}}|\phi_i(\mathbf{r})\rangle|^2 \frac{v_{\mathbf{q}}}{k}\delta(k'-k)k'^2 dk'. \quad (3.38)$$

In writing the above equation we have taken advantage of the orthogonality relation of the spherical harmonics and have again used a standard result from Messiah [30] to correctly evaluate the strength of the delta function,

$$\delta\left(\omega - |\omega_o| - \frac{1}{2}k'^2\right) = -\frac{1}{k}\delta(k'-k), \quad (3.39)$$

where, $k = \sqrt{2(\omega - |\omega_o|)}$. Then

$$Im\,\epsilon^{-1}(\mathbf{q},\omega) = \frac{1}{2}v_{\mathbf{q}}k \sum_{i,l_f,m_f} |\langle R_{l_f} Y_{l_f m_f}|\rho^*_{\mathbf{q}}|\phi_i\rangle|^2. \quad (3.40)$$

To evaluate the matrix element in equation (3.40) we must now consider the explicit forms of the initial state, $|\phi_i(r)\rangle$, and the density operator, $\rho^*_{\mathbf{q}}$.

It is well known that a bound atomic orbital may be written as the product of a radial wavefunction and a spherical harmonic. We can also expand the density operator, $\rho^*_{\mathbf{q}}$, in terms of spherical harmonics using a standard result from Pendry [8]. From equation (3.19) we have,

$$\rho^*_{\mathbf{q}} = \exp(\imath\mathbf{q}\cdot\mathbf{r}) = \sum_{LM} 4\pi\imath^L j_L(qr)Y_{LM}(\hat{q})Y^*_{LM}(\hat{r}). \quad (3.41)$$

In this formulation it is more natural to rewrite the sum over occupied atomic orbitals as a sum over n_o, l_o and m_o quantum numbers. Then, multiplying by a factor of 2 to account for spin degeneracy, it follows that $Im\,\epsilon^{-1}(\mathbf{q}\,\omega)$ is given by,

$$\begin{aligned} Im\,\epsilon^{-1}(\mathbf{q},\omega) \;=\; & \frac{64\pi^3 k}{q^2}\sum_{n_o}\sum_{l_o m_o}\sum_{l_f m_f}\sum_{LM}\sum_{L'M'} \imath^{(L-L')}\langle R_{l_f}(r)|j_L(qr)|\phi_{l_o}(r)\rangle \times \\ & \langle\phi_{l_o}(r)|j_{L'}(qr)|R_{l_f}(r)\rangle\langle Y_{l_f m_f}|Y^*_{LM}|Y_{l_o m_o}\rangle\langle Y_{l_o m_o}|Y_{L'M'}|Y_{l_f m_f}\rangle \times \\ & Y_{LM}(\hat{q})Y^*_{L'M'}(\hat{q}). \end{aligned} \quad (3.42)$$

Again we can simplify the above equation by using a relation from Brink and Satchler [29] to write the integrals over the spherical harmonics in terms of Wigner-3j coefficients (eqn.(2.21)). Then noting that the Wigner-3j's may be cyclically permuted we can apply the orthogonality relation, equation (2.22). Finally the addition theorem [30] may be used to rid equation (3.42) of the $Y_{LM}(\hat{q})'s$. Then, as expected, we find the imaginary part of the dielectric function to be independent of the direction of polarisation of the perturbation.

$$Im\,\epsilon^{-1}(q,\omega) = \frac{4\pi k}{q^2}\sum_{n_o}\sum_{l_o,L,l_f}|\langle R_{l_f}(r)|j_L(qr)|\phi_{l_o}(r)\rangle|^2 \times (2l_f+1)(2L+1)(2l_o+1)\begin{pmatrix} l_f & L & l_o \\ 0 & 0 & 0 \end{pmatrix}^2 . \quad (3.43)$$

This is the contribution to $Im\,\epsilon(q,\omega)$ from a single atom consisting of fully occupied states only. To calculate the actual atomic imaginary part of $\epsilon^{-1}(q,\omega)$ we must multiply equation (3.43) by the number of electrons in each atomic orbital, $n_{(n_o,l_o)}$, divided by the number of electrons in a full atomic orbital, $2(2l_o+1)$. Then,

$$Im\,\epsilon^{-1}(q,\omega) = \frac{2\pi k}{q^2}\sum_{n_o}\sum_{l_o,L,l_f} n_{(n_o,l_o)}\left|\int r^2 R_{l_f}(r) j_L(qr)\phi_{l_o}(r)dr\right|^2 \times (2l_f+1)(2L+1)\begin{pmatrix} l_f & L & l_o \\ 0 & 0 & 0 \end{pmatrix}^2 . \quad (3.44)$$

As L increases the first maximum in the Bessel function in equation (3.44) moves further out from the centre of the atom consequently reducing the magnitude of the radial matrix element at high angular momenta. The Wigner 3-j coefficients also tend to decrease as L increases [29]. Numerically we therefore find that the L sum can be converged using a maximum angular momentum of 20 at the energies investigated. We set the condition of convergence to be that

the contribution from two subsequent angular momentum states be less than 1% of the total contribution to $Im\epsilon^{-1}(q,\omega)$.

The real part

Once the imaginary part of $\epsilon^{-1}(q\,\omega)$ has been evaluated it is a simple matter to calculate the real part using the Kramers-Kronig relation,

$$Re\,\epsilon^{-1}(q,\omega) = 1 + \frac{1}{\pi}\int_{-\omega_o}^{\infty} d\omega_{ko} Im\,\epsilon_i^{-1}(q,\omega_{ko}) \left\{ \frac{2\omega_{ko}}{\omega^2 - \omega_{ko}^2} \right\}, \tag{3.45}$$

where $\omega_{ko} = \frac{1}{2}k^2 + |\omega_o|$.

3.4.5 The X-ray Absorption Coefficient

Small q Limit Of $\epsilon^{-1}(\mathbf{q}\,\omega)$

At low q the frequency and wavevector dependent dielectric function may be related to the X-ray absorption coefficient, $\mu_o(\omega)$. In the small q limit the density operator may be expanded in a power series. Then, on use of the addition theorem, $\rho_{\mathbf{q}}^*$ becomes,

$$\begin{aligned} \rho_{\mathbf{q}}^* &= \exp(\imath\mathbf{q}\cdot\mathbf{r}) \approx 1 + \imath qr\cos\alpha = 1 + \imath qr P_1(\cos\alpha) \\ &= 1 + \imath qr\frac{4\pi}{3}\sum_{M=-1}^{1} Y_{1M}(\hat{q})Y_{1M}^*(\hat{r}). \end{aligned} \tag{3.46}$$

Substituting this expression into equation (3.40) for the imaginary part of the dielectric function we can sum over all initial states to obtain the total $Im\,\epsilon^{-1}(q,\omega)$. Then, remembering that the initial and final photoelectron states are orthogonal we find,

$$\lim_{q\to 0} Im\,\epsilon^{-1}(q,\omega) = \frac{2}{3}\pi k \sum_{n_o,l_o,l_f} n_{(n_o l_o)} |\langle R_{l_f}|r|\phi_{l_o}\rangle|^2 (2l_f+1) \begin{pmatrix} l_f & 1 & l_o \\ 0 & 0 & 0 \end{pmatrix}^2 . \tag{3.47}$$

We have again used the orthogonality relations of the Wigner-3j coefficients and the addition theorem for spherical harmonics. As in Chapter 2, the Wigner-3j

coefficient in equation (3.47) is only non zero if $l_f = l_o \pm 1$. Thus, writing out the 3j coefficients explicitly we find that the imaginary part of the dielectric function is given by,

$$Im\,\epsilon^{-1}(0,\omega) = \frac{2}{3}\pi k \sum_{n_o,l_o} \frac{n_{(n_o l_o)}}{2l_o+1} \left\{ |\langle R_{l_o+1}|r|\phi_{l_o}\rangle|^2 (l_o+1) + |\langle R_{l_o-1}|r|\phi_{l_o}\rangle|^2 l_o \right\}. \tag{3.48}$$

The $q = 0$ imaginary part of the dielectric function found within an atomic calculation is related to $\mu(\omega)$ by,

$$\mu_o(\omega) = \frac{\omega}{c} Im\,\epsilon^{-1}(0\,\omega), \tag{3.49}$$

where c is the speed of light in vacuo. Thus substituting for $Im\,\epsilon^{-1}(0\,\omega)$ from equation (3.48) we obtain a result for the absorption coefficient identical to equation (2.27).

3.5 Results

We are now at a stage where the various forms for the inverse dielectric function may be evaluated numerically. In this chapter we approximate the atomic potential with the sum of the Hartree potential and the Slater $X\alpha$ exchange. In equation (2.1) we approximate $V_{XC}(r)$ with $V_{X\alpha}(r)$ where [36],

$$V_{X\alpha} = -\frac{3}{2}\alpha \left(\frac{3n(r)}{\pi}\right)^{\frac{1}{3}}. \tag{3.50}$$

In the calculation of the dielectric function we deal with free atoms only. We do this by extending the muffin tin radii to much larger values than those encountered in the solid, typically around 25 atomic units. As we are treating free atoms we can take the values of the variable parameter, α, in the free electron Slater exchange potential from the tabulation of Schwarz [44].

3.5.1 The Small q Limit

The X-ray Absorption Coefficient

Using the various approximations discussed above we can calculate the X-ray absorption coefficient in the atomic theory of equation (3.49), accurately and efficiently over a wide range of energies and for all atoms in the periodic table. In figures 3.2, and 3.3, we show a value for $\mu(\omega)$ obtained from the inverse imaginary part of the dielectric function plotted against energy. The absorption coefficient does not show the complexity expected from a full band structure calculation but compares well to the tabulated results of Veigele [45]. Veigele's tabulations consist of experimental data above X-ray energies of 1keV and theoretical results calculated using a computationally intensive Hartree-Fock theory below this energy.

In figure 3.4 we compare results for the gold M edges which are known to show an unusually slow onset. The calculation follows the shape of the experimentally measured absorption coefficient [46] reasonably well but slightly overestimates the speed of the cut in of the M-edge absorption. To compare with the M-edge data from Owens *et al* directly we have normalised the calculated results to the experimental results at 3 keV.

Comparison With Free Electron Calculation

Figures 3.2 and 3.3 also show a result for $\mu(\omega)$ calculated from the single plasmon pole dielectric function within the local density approximation (eqn.(3.36)).

We can see that the average single plasmon pole dielectric function exhibits the same overall energy dependence as the atomic calculation but, as we would expect, lacks the sharp structure of the atomic calculations at the absorption edges. This has a simple physical interpretation: In equation (3.36) there are

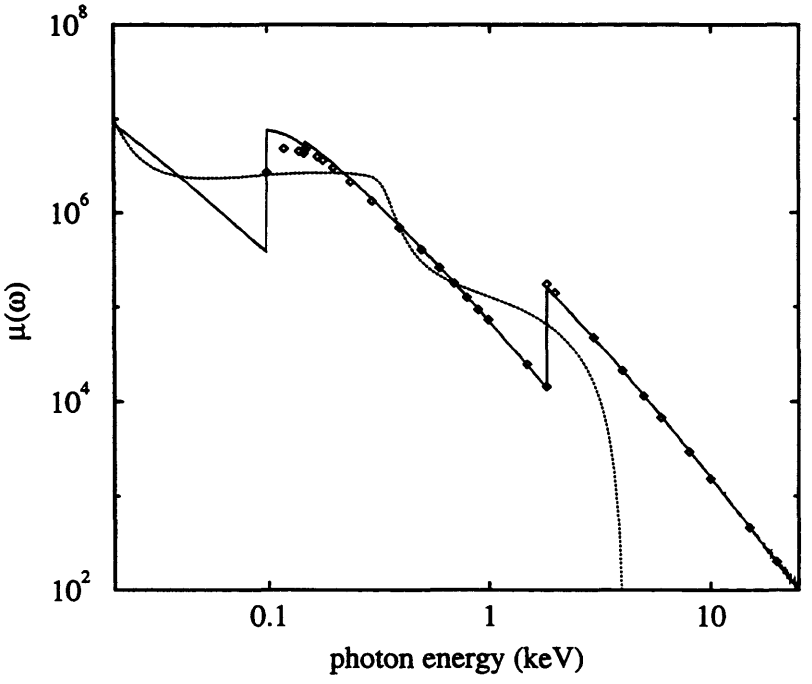

Figure 3.2: $\mu(\omega)$ in Barns per atom plotted against energy in keV for silicon. The solid line shows the result obtained from an atomic calculation, whilst the dotted line gives the result calculated from the average LDA, SPP inverse dielectric function. The diamonds show Veigele's tabulated result [45].

no contributions to the imaginary part of the response function at frequencies corresponding to single particle excitation energies, instead each atom absorbs at frequencies in a shell where ω is equal to the local q dependent plasma frequency.

We observe a sharp high energy cut off in the SPP dielectric function, beyond which the perturbing field cannot excite any response from the electron system. The cut off frequency corresponds to the highest accessible local plasmon, ie. the point of highest electron density of the atom in question.

For free atoms the single plasmon pole dielectric function does not exhibit a low energy cut off for the simple reason that the charge density tends to fall smoothly to zero by the edge of the extremely large muffin tins that are used. The atomic calculation, on the other hand, does fall sharply to zero below a certain energy. At frequencies lower than the binding energy of the most weakly bound state

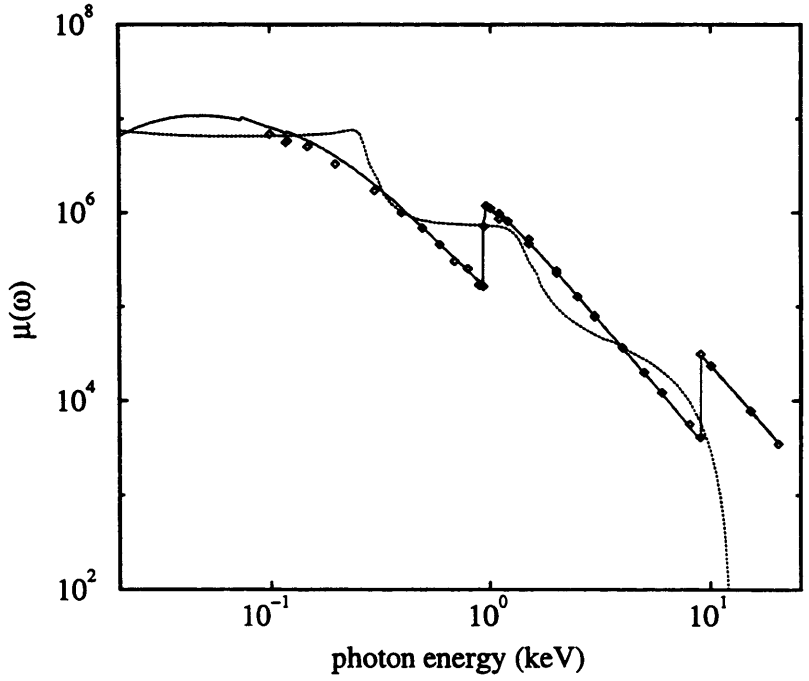

Figure 3.3: $\mu(\omega)$ in Barns per atom plotted against energy in keV for copper. The solid line shows the result obtained from an atomic calculation, whilst the dotted line gives the result calculated from the average LDA, SPP dielectric function. The diamonds show Veigele's tabulated result [45].

there is not enough energy available to excite any electrons into the continuum, and thus, within our approximations, we obtain no contribution to the dielectric function.

Overall, the LDA single plasmon pole inverse dielectric function appears to give a reasonable approximation to the $q = 0$ atomic inverse dielectric function, except at high energies where the single plasmon pole result underestimates the imaginary part of $Im\,\epsilon$, and hence $\mu(\omega)$.

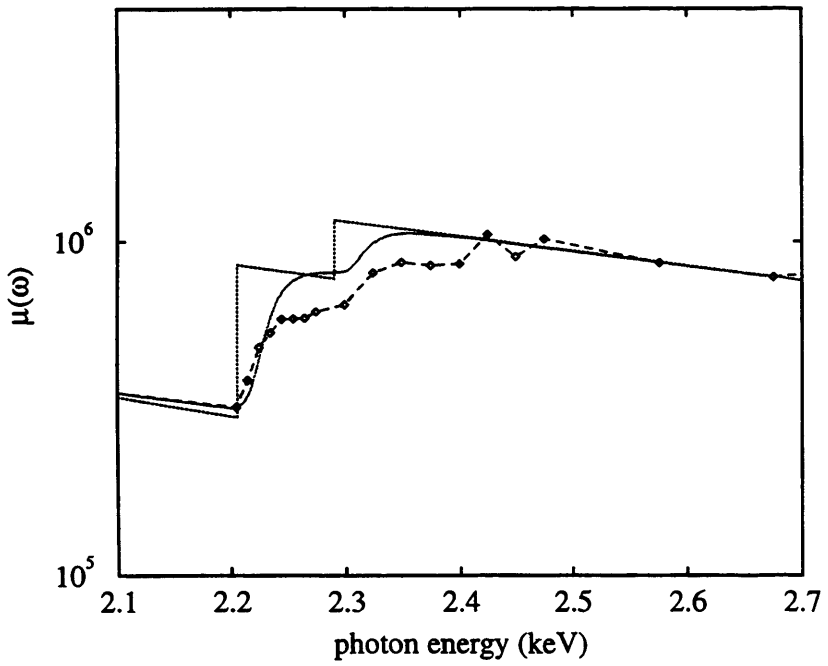

Figure 3.4: $\mu(\omega)$ in Barns per atom plotted against energy in keV for the gold M-edges. The dotted line is Veigele's tabulated result, the diamonds with the dashed line show the experimental data [46] whilst the solid line is the calculated result.

3.5.2 q Dependence

In figure 3.5 $Im\,\epsilon^{-1}(q,\omega)$ is plotted against q at three separate energies: $\omega = 10eV$, $\omega = 100eV$ and $\omega = 400eV$, for silicon. The solid curves show $Im\,\epsilon^{-1}(q,\omega)$ calculated from the average LDA SPP ϵ^{-1}. These exhibit a sharp cut off at a q value where $\frac{1}{3}(qk_f)^2 + \frac{1}{4}q^4 = \omega$. Beyond this q value, the charge density is insufficiently large, anywhere in the atom, for a plasmon to be excited.

The points in figure 3.5 show the equivalent results obtained from an atomic calculation. These curves exhibit a peak in the same place as the free electron gas results, at $\omega \sim \frac{1}{2}q^2$. As we increase ω the peak obviously moves out to a higher q. As both the free electron gas calculation and the atomic calculation satisfy the same sum rule the areas under the two sets of curves must be equivalent.

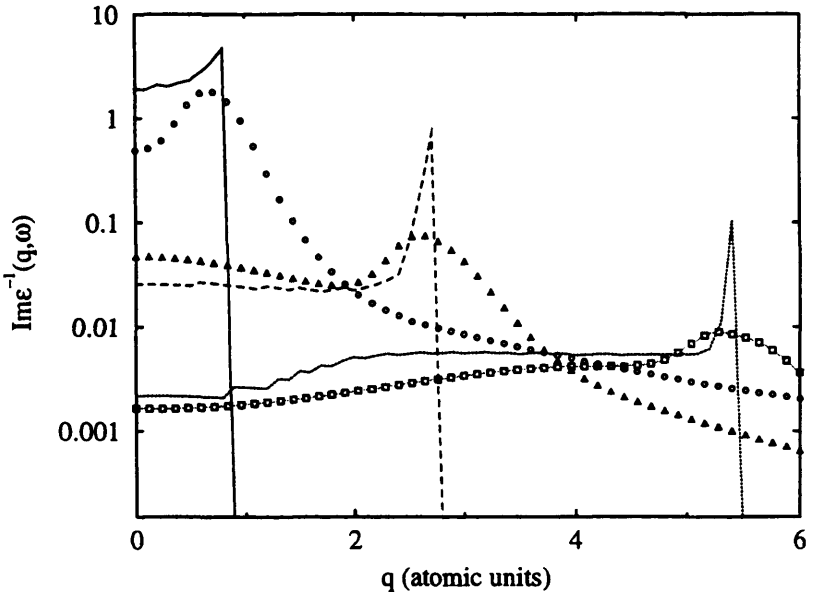

Figure 3.5: $Im\,\epsilon^{-1}(q,\omega)$ against q at fixed energy for silicon. The solid lines are calculated using the average LDA, SPP inverse dielectric function. The points are the results of the atomic calculation. The solid line and the circles are calculated at $\omega = 10eV$, the dashed line and the triangles at $\omega = 100eV$ and the dotted line and the squares at $\omega = 400eV$.

The presence of a peak in $Im\,\epsilon^{-1}(q,\omega)$ can be deduced if we consider the contribution to the inverse dielectric function from each initial state separately. In figure 3.6 we show the contribution to $Im\,\epsilon^{-1}(q,\omega)$ from the copper 4s and the copper 3d initial states.

If we take the final states to be entirely free electron like and assume the initial state to possess a spherical symmetry then, in equation (3.44) for the imaginary dielectric function, the relevant matrix element reduces to,

$$\int r^2 \phi_{l_o}(r) j_{l_f}(kr) j_{l_f}(qr) dr. \tag{3.51}$$

As the initial states will look something like the Slater form of $r^n \exp(-\alpha r)$ [19], equation (3.51) will obviously have a sharp maximum at $q = k$ where the periods of the two spherical Bessel functions match. This effect can be seen in

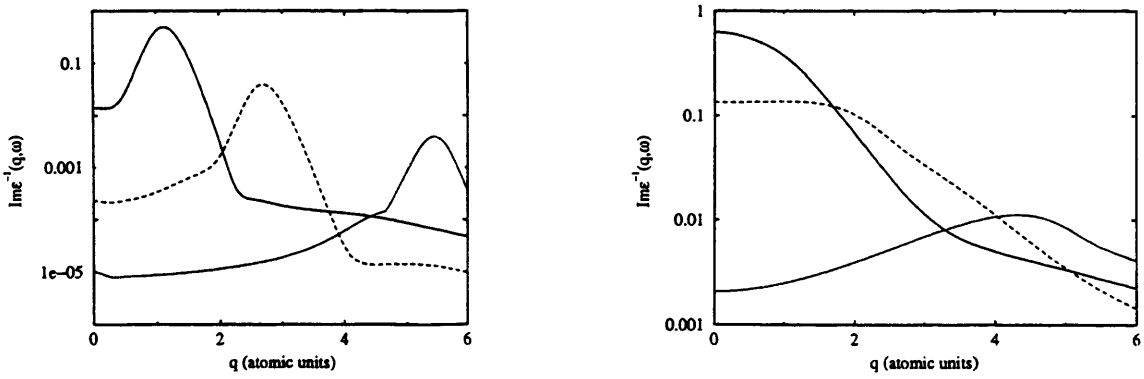

Figure 3.6: The contribution to the imaginary part of an atomic inverse dielectric function from a single initial state plotted as a function of q at fixed energy. The solid line is at $\omega = 20eV$, the dashed line at $\omega = 100eV$ and the dotted line at $\omega = 400eV$. The curve on the left shows the contribution from the copper 4s orbital, the curve on the right is the contribution from the copper 3d orbital.

the left hand curve of figure 3.6 where the contributions to $Im\,\epsilon^{-1}(q,\omega)$ from an copper 4s state are plotted against q at various final state energies. We can see that the maxima occur almost exactly at $q = \sqrt{2E}$, at $q = 1.2, q = 2.7$ and $q = 5.4$ atomic units for $E = 20eV$, $E = 100eV$ and $E = 400eV$.

The high peak contribution to the total imaginary part of the dielectric function is greater for the more weakly bound initial states. The muffin tin potential is weaker at the outer regions of the muffin tin spheres and so it is in this area where the final state becomes most free electron like and hence where there is the greatest possibility of the final state and perturbation matching. However, it is only the most weakly bound states that are significantly different from zero in these regions. The high q contribution from the more tightly bound states tends to get killed in comparison.

In the right hand curve of figure 3.6 the contribution to $Im\,\epsilon^{-1}(q,\omega)$ from a copper 3d initial state is plotted. The maxima in this function are much less sharp than those seen previously and do not occur exactly at $q = k$. This is because of

the more complex angular dependence of the initial state. To get the same sort of resonance effect we have to match a Bessel function of angular momentum L with the final state of angular momentum $l_f = L \pm l_o$.

3.6 Conclusion

In this chapter we have derived expression for the non-local self energy, $\Sigma(\mathbf{r}_1, \mathbf{r}_2, \omega)$ and for the Hartree inverse dielectric function. In its local form, Σ is equivalent to an effective complex scattering potential, the imaginary part of which may be used to describe losses to the EXAFS. We investigate Σ using two different theories in later chapters.

The self-energy depends on the inverse dielectric function used. We have calculated the local Hartree $Im\,\epsilon^{-1}(q,\omega)$ in an atomic system both directly and via a uniform electron gas calculation using the local density approximation. We have shown that the result of the atomic calculation may be equated to the X-ray absorption coefficient in the limit as q tends to zero. This result will be used in Chapter 7. The results obtained for the X-ray absorption coefficient agree well with experiment and previous tabulated values [45]. The atomic dielectric function is also used in the calculation of the Beni, Lee and Platzman polarisation potential (Chapter 5), although in a non-local form.

The LDA, single plasmon pole $Im\epsilon^{-1}(q,\omega)$ is used in the Hedin-Lundqvist calculation of the self-energy. We have shown that this form of the inverse dielectric function exhibits the same overall energy dependence as the atomic form for $Im\epsilon^{-1}(q,\omega)$ but does not have the same sharp features at the single particle excitation energies. The SPP dielectric function also underestimates the screening at high ω and at high q because of the artificial cut off of $Im\,\epsilon^{-1}$ in this theory, at the point where the charge density in the atom reaches a maximum.

Chapter 4

An Investigation of the Hedin-Lundqvist Exchange and Correlation Potential

In this chapter we investigate the Hedin-Lundqvist [9] (HL) form of the exchange and correlation potential. This potential was first applied to EXAFS calculations within the local density approximation by Lee and Beni [10] and is the potential most commonly used today, for example in the Daresbury program EXCURV98 [14] and the equivalent American program, FEFF [47].

We begin by outlining the derivation of the HL potential from the general form of the self-energy discussed in Chapter 3. We show the the Slater $X\alpha$ potential [36] and the Dirac-Hara exchange potential [48, 49] can be obtained as special cases of the real part of the HL potential. The imaginary part of the HL potential is also calculated.

The main part of the chapter is concerned with the losses to the EXAFS produced by the HL potential. This potential was designed to model only the extrinsic losses to the photoelectron beam, making no provision for the intrinsic losses. When data fitting using this potential one should therefore need to use a value of s_o^2 of about 0.7, equivalent to the values used in the original method of EXAFS analysis (eqn.(1.3)). This is found not to be the case [33]. In this chapter we calculate the losses generated by the HL potential using the theory discussed

in Chapter 2 and compare them to the historically used EXAFS loss factors: the amplitude reduction factor, s_o^2, and a mean free path term, $exp(-2r_j V_{PI}/k)$ (see Chapter 1).

4.1 Calculation of the Potential

4.1.1 The Self-Energy

We start from the random phase approximation for the electron self-energy defined in the previous chapter. Hedin and Lundqvist [9] derive an expression for the self-energy in a uniform electron gas of density n. Lee and Beni [10] then generalise this result to systems of varying charge density, such as atoms and molecules, using the local density approximation (LDA).

It is easiest to apply the uniform electron gas relations to equation (3.11). In the uniform electron gas the electronic wavefunctions are plane waves and all the properties of the system must be translationally invariant. In equation (3.11) the self-energy and G_o are therefore functions of $\mathbf{r}_1 - \mathbf{r}_2$ only. Then, taking the local form of the inverse dielectric function and Fourier transforming we have that,

$$\Sigma(k, w) = \frac{\imath}{(2\pi)^4} \int v_{\mathbf{q}} \epsilon^{-1}(\mathbf{q}, \omega') G_o(\mathbf{k} - \mathbf{q}, \omega - \omega') d\omega' d\mathbf{q}. \tag{4.1}$$

Where $G_o(\mathbf{k}, \omega)$ is the Hartree Green function in Fourier transform,

$$G_o(\mathbf{k}, \omega) = (\omega - E_{\mathbf{k}} + \imath\delta sign(E_{\mathbf{k}} - E_f))^{-1}, \tag{4.2}$$

and E_f is the Fermi energy.

As in Chapter 3, we can perform the integral above using contours. Closing contours in the lower half plane we obtain a contribution from the pole in G_o from occupied states only and a contribution from a pole in the inverse dielectric function. To obtain the Hedin-Lundqvist result for the self-energy we must use

the single plasmon pole form for the inverse dielectric function (eqn.(3.31)). Then,

$$\Sigma(k,\omega) = \frac{-1}{(2\pi)^3}\int d\mathbf{q}\left\{n_{\mathbf{k}-\mathbf{q}}v_{\mathbf{q}}\epsilon^{-1}(\mathbf{q},\omega - E_{\mathbf{k}-\mathbf{q}}) - \frac{v_{\mathbf{q}}\omega_p^2}{2\omega_q}G_o(\mathbf{k}-\mathbf{q},\omega-\omega_q)\right\}, \tag{4.3}$$

Where $n_{\mathbf{k}-\mathbf{q}}$ is the occupancy of the state with wavevector $\mathbf{k}-\mathbf{q}$. If we ignore the screening, ie. take $\epsilon^{-1}(q,\omega) = 1$ in equation (4.1), we remove the 2nd term from the equation above and Σ reduces to the Hartree Fock exchange potential in the uniform electron gas,

$$\begin{aligned}\Sigma_{HF}(k) &= \int n_{\mathbf{k}-\mathbf{q}}v_{\mathbf{q}}\mathbf{dq} \\ &= -\frac{k_f}{\pi}\left[1+\frac{k_f^2-k^2}{2kk_f}log\left|\frac{k_f+k}{k_f-k}\right|\right],\end{aligned} \tag{4.4}$$

When applied under the local density approximation, in which the Fermi wavevector becomes position dependent, equation (4.4) gives the Dirac-Hara [48, 49] approximation to the exchange potential. This is another potential which is commonly used in EXAFS calculations. The Dirac-Hara self-energy is known to give good photoelectron phase-shifts [50, 51] but, as it is an entirely real potential, it obviously does not account for inelastic scattering events in the same way as the HL potential. The Dirac-Hara potential is also closely related to the Slater $X\alpha$ exchange (eqn.(3.50)). Taking $k = k_f$ in the above equation we obtain the Kohn-Sham approximation to the $X\alpha$ exchange which is equivalent to setting $\alpha = \frac{2}{3}$ in equation (3.50). We can also obtain an average free electron exchange potential by summing equation (4.4) over all occupied states and then dividing by the total number of electrons,

$$\begin{aligned}V_{X\alpha}(k) &= \frac{2}{(2\pi)^3 n}\int n_{\mathbf{k}}\Sigma_{HF}(k)d\mathbf{k} \\ &= -\frac{3}{2}\left(\frac{k_f}{\pi}\right) = -\frac{3}{2}\left(\frac{3n}{\pi}\right)^{\frac{1}{3}}.\end{aligned} \tag{4.5}$$

The integral has been performed with the help of the computational mathematics software, Maple. n is the number of electrons per unit volume and we have

assumed the system to be non-magnetic and have therefore treated opposite spins equivalently. Equation (4.5) is simply the $X\alpha$ exchange with a value of $\alpha = 1$.

In this chapter we are mostly concerned with the inelastic scatterings of the photoelectron. These are described by the imaginary part of equation (4.3),

$$\begin{aligned} Im\,\Sigma(k,\omega) &= \frac{\omega_p^2}{(4\pi)^2}\int \frac{v_{\mathbf{q}}}{\omega_q}\left[n_{\mathbf{k}-\mathbf{q}}\delta(E_{\mathbf{k}-\mathbf{q}}-\omega-\omega_q)\right. \\ &\quad \left.-(1-n_{\mathbf{k}-\mathbf{q}})\delta(E_{\mathbf{k}-\mathbf{q}}-\omega+\omega_q)\right]d\mathbf{q}. \end{aligned} \tag{4.6}$$

Within the single plasmon pole approximation we can see that we obtain contributions to the imaginary part of the electron self-energy from two types of process. The 2nd term in equation (4.6) describes the absorption of electrons of frequency ω from the system. Electrons with initial energy ω drop into an empty state of wavevector $\mathbf{k}-\mathbf{q}$ resulting in the emission of a plasmon of energy ω_q. The first term in equation (4.6) adds electrons of frequency ω into the system. Electrons initially in a state of energy $E_{\mathbf{k}-\mathbf{q}}$ absorb a plasmon and are excited into the electronic state of frequency ω.

4.1.2 The Exchange and Correlation Potential within the LDA

The relation for the electron self-energy given above applies within an electron gas of uniform density. We may, however, modify this result so that it applies to real, inhomogeneous, materials by using the local density approximation. In this approximation the assumed constant density is replaced by a spatially varying function. As the electronic density, and hence the total potential, vary with r the kinetic energy at the Fermi level, $\frac{1}{2}k_f^2$, must also vary radially so that the thermodynamic Fermi energy, E_f remains constant. Then,

$$\frac{1}{2}k_f^2(r) = V_o(r) + E_f + \Sigma, \tag{4.7}$$

where $V_o(r)$ is the electronic potential and Σ is the electron self-energy. In order to avoid self consistency problems we follow Lee and Beni [10] and assume that the

self-energy is small compared to $V_o(r)$ so that we may neglect Σ in the equation above. The energy of the incident electron, ω, will also vary locally. If we take the electron to have an energy E_i far from the scattering potential then,

$$\begin{aligned} \omega &= \frac{1}{2}k^2(r) = E_i - E_f + \frac{1}{2}k_f^2(r) \\ &= E_i + V_o(r). \end{aligned} \tag{4.8}$$

As both k and ω vary with position in the local density approximation we may write the electron self-energy as a function of r, and E_i, the energy of the electron far from the scattering potential,

$$\Sigma(k,w) \rightarrow \Sigma\left(k(r), \frac{1}{2}k^2(r)\right) \rightarrow V(r, E_i). \tag{4.9}$$

In this case the self-energy reduces to a one body, r-dependent potential, the exchange and correlation potential.

By substituting $\omega - E_{\mathbf{k}-\mathbf{q}}$ as $\omega' = kqx - \frac{1}{2}q^2$ where x is the angle between wavevectors $\mathbf{q}$ and $\mathbf{k}$ we may write the real part of the self-energy from equation (4.3) as,

$$\begin{aligned} V_R(r, E_i) = -\frac{1}{\pi}\int \Bigg\{ & n_{\mathbf{k}-\mathbf{q}}\left[1 + \frac{\omega_p^2}{2\omega_q}\left(\frac{1}{\omega' - \omega_q} - \frac{1}{\omega' + \omega_q}\right)\right] \\ & - \frac{\omega_p^2}{2\omega_q}\frac{1}{\omega' - \omega_q}\Bigg\} dqdx. \end{aligned} \tag{4.10}$$

The Fermi occupation factor, $n_{\mathbf{k}-\mathbf{q}}$ limits the dx integral from x_1 to 1 where,

$$\begin{aligned} x_1 &= 1 && q < q_{min} \\ &= \frac{1}{kq}(E_i + \frac{1}{2}q^2 - E_f) && q_{min} < q < q_{max} \\ &= 1 && q > q_{max}, \end{aligned} \tag{4.11}$$

where $q_{min} = k - k_f$ and $q_{max} = k + k_f$ and x_1 is always greater than -1 provided that $E_i > E_f$. Where $x_1 = 1$ we obtain a zero contribution from the x integral. This effectively limits the range of the q integral from q_{min} to q_{max}.

The x integral above may be performed analytically for all values of q. We can evaluate the q integral analytically in the large q limit if we replace ω_q by its asymptotic value of $\omega_q = \frac{1}{2}q^2$. We therefore choose to split the q integral into two regions. Below q_c we perform the q integral numerically whilst above q_c we approximate ω_q and work analytically. We then obtain the real part of the exchange and correlation potential as,

$$\begin{aligned} V_R(r, E_i) &= -\frac{1}{2\pi}\left\{2I_1 + \omega_p^2\left[I_2 + I_3 + \int_o^{q_c}\frac{dq}{2kq\omega_q}\log\left|\frac{(\frac{1}{2}q^2+\omega_q+kq)^2+\delta^2}{(\frac{1}{2}q^2-\omega_q-kq)^2+\delta^2}\right|\right.\right. \\ &+ \left.\left.\int_o^{q_c}\frac{dq}{2kq\omega_q}\log\left|\frac{(\frac{1}{2}q^2-\omega_q+kqx_1)^2+\delta^2}{(\frac{1}{2}q^2+\omega_q+kqx_1)^2+\delta^2}\right|\right]\right\}. \end{aligned} \tag{4.12}$$

Where δ is an infinitesimal used to avoid numerical divergences in the integrands. We choose the cut-off wavevector q_c to be a multiple of the plasma frequency, ω_p. A value of $\sqrt{100\omega_p}$ appears to give satisfactory results. The results for I_1, I_2 and I_3 are somewhat complex. They are listed in appendix A.

As $r \to 0$ the electronic potential, $V_o(r)$ becomes very large thus, from equations (4.7) and (4.8) we can see that, $k(r)$ must be very large and approximately equal in magnitude to $k_f(r)$. Then, ignoring all the terms proportional to $1/k(r)$ in equation (4.12) we find that the HL result for the exchange and correlation potential looks very similar to the Slater exchange ($X\alpha$) potential close in towards the atomic nucleus,

$$V_R(r, E_i) = -\frac{k_f(r)}{\pi}. \tag{4.13}$$

Equation (4.13) is obviously just the Kohn-Sham approximation to the $X\alpha$ exchange.

We evaluate the imaginary part of the self-energy in a similar fashion starting from equation (4.6). The Fermi occupation function, $n_{\mathbf{k}-\mathbf{q}}$, limits the x integral

from x_1 to 1 whilst the factor $(1 - n_{\mathbf{k-q}})$ limits the integral from -1 to x_1, then,

$$V_I(r, E_i) = \frac{\omega_p^2}{2k} \int \frac{dq}{q\omega_q} \left\{ \int_{x_1}^{1} \delta\left(x - \frac{\frac{1}{2}q^2 - \omega_q}{kq}\right) dx - \int_{-1}^{x_1} \delta\left(x - \frac{\frac{1}{2}q^2 + \omega_q}{kq}\right) dx \right\}. \tag{4.14}$$

For photoelectrons with energy E_i greater than the thermodynamic Fermi energy, E_f only the second term contributes and hence,

$$V_I(r, E_i) = -\frac{\omega_p^2}{2k} \int_o^{q_{max}} \frac{dq}{q\omega_q} \int_{-1}^{x_1} \delta\left(x - \frac{\frac{1}{2}q^2 + \omega_q}{kq}\right) dx. \tag{4.15}$$

The imaginary part of the exchange and correlation potential is only non zero for electrons with energies greater than that needed to excite a local plasmon, $E_i - E_f > \omega_q$. Below this energy the incident electrons are not energetic enough to excite a plasmon and so, in the single plasmon pole approximation, inelastic scattering events are impossible.

Using equations (4.12) and (4.15) we can calculate the real and imaginary parts of the exchange and correlation potential as a function of r. In the next section of this chapter we compare the real parts of the HL potential to the Dirac-Hara potential (equation(4.4)) and the free electron Slater exchange (equation(3.50)). We also investigate the magnitude of the inelastic scattering events modelled by the imaginary part of the self-energy. We use $V_I(r, E_i)$ to calculate the losses to the EXAFS signal accounted for in this formalism and compare these to experimental data.

4.2 Results

In this chapter we wish to investigate the HL potential for materials in the solid state. We therefore take the muffin tin radii to be appropriately small. By doing this we may compare directly with most EXAFS measurements and with previous work. Also the HL potential should be more accurate for systems of high electronic density.

4.2.1 The HL Potential

In the figure below we plot the real and imaginary parts of the HL potential against r for Bromine at various photoelectron energies. These curves can be compared to the original results produced by Lee and Beni [10].

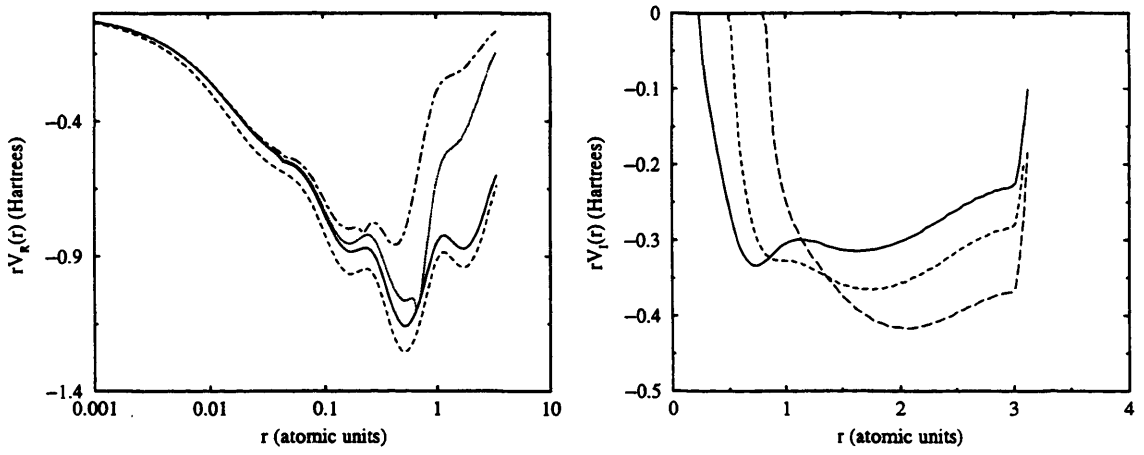

Figure 4.1: The real and imaginary parts of the HL potential plotted against r for Bromine at various energies. The left hand curve shows $rV_R(r)$ at $k = 8$ a.u.s (dot-dash curve), at $k = 4$ a.u.s (dotted curve) and at $k = 0.5$ a.u.s (solid line). The Slater X_α exchange with $\alpha = 0.8$ is shown for comparison (dashed curve). The right hand graph shows $rV_I(r)$ at $k = 7$a.u.s (solid line), $k = 5$ a.u.s (short dashed line) and $k = 3$ a.u.s (long dashed line).

The real part of the exchange and correlation potential decreases with increasing energy. This is reasonable. A fast moving photoelectron will have much less chance of interacting with the bound electrons than a low energy photoelectron. At low energies and at small r the real part of the HL potential looks like the Slater $X\alpha$ exchange as expected. The real and imaginary parts to the potential are discontinuous at the edges of the muffin tin spheres where we have truncated the atomic density.

The imaginary part of the HL potential is zero at small r. In this region of high electronic density the incident photoelectron is insufficiently energetic to excite a plasmon. As soon as the density falls sufficiently for plasmons to be

excited V_I cuts in almost immediately to its maximum value. At larger incident photoelectron energies V_I obviously cuts in at lower radii, however, for large E_i the imaginary part of the potential is generally smaller in the outer regions of the atomic muffin tins.

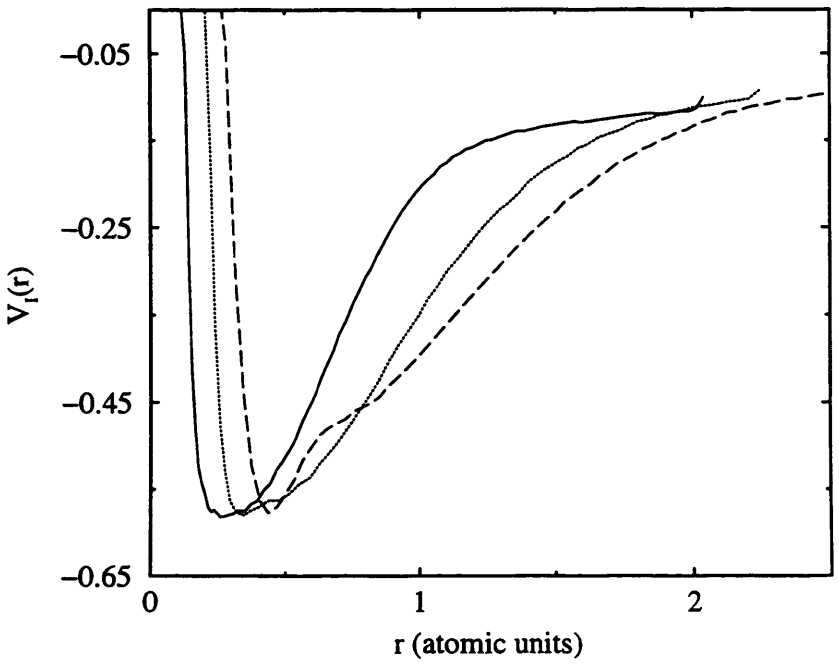

Figure 4.2: The imaginary part of the HL potential in Hartrees, at $k = 8$ atomic units. Calculated for silicon (solid line), copper (dotted line) and silver (dashed line).

Figure 4.2 shows the imaginary part of the HL potential calculated for three elements: silicon, copper and silver. The imaginary part of the HL potential looks very similar for these very different elements. The electron mean free paths for these elements will therefore also be very similar as has long been assumed experimentally. The radius at which the HL potential cuts in moves slightly outward as we go up in atomic number. This is because the electron density is larger close to the nucleus for elements with higher atomic numbers. The corresponding plasmon excitation frequency is therefore higher and so we have to move further out from the centre of the atom before it becomes possible to excite

a plasmon with a photoelectron of given energy.

In figure 4.3 we compare the Slater $X\alpha$ exchange to the real part of the HL potential and the energy-dependent Hara exchange potential calculated for copper. The curve on the left gives the comparison at a photoelectron wavevector of $k = 0.5$ atomic units whilst the graph on the right is at $k = 8$ a.u.s.

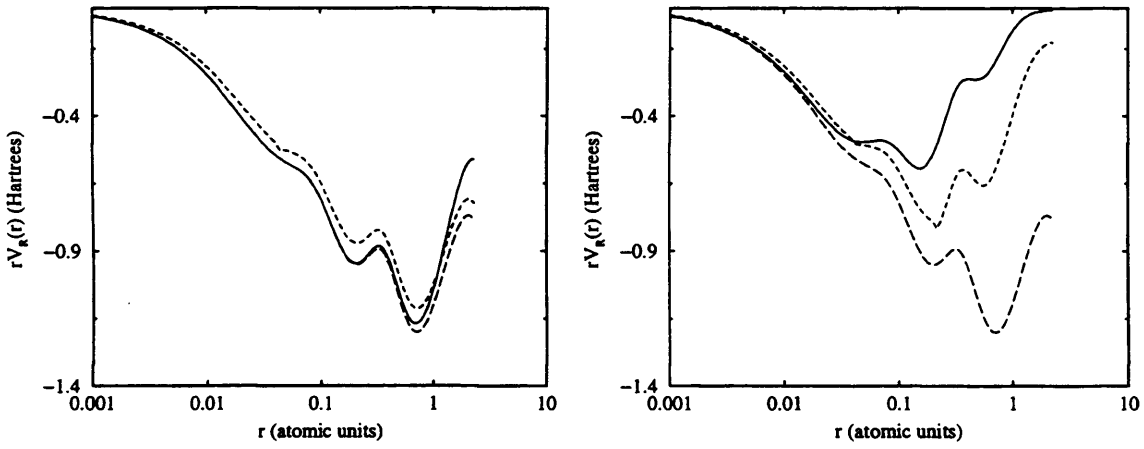

Figure 4.3: Comparison between the Dirac-Hara potential (solid line), the HL potential (short dashed line) and the Slater exchange with $\alpha = 0.8$ (long dashed line) at $k = 0.5$ atomic units (left hand graph) and $k = 8$ atomic units (right hand graph). Calculated for copper.

At low photoelectron energies all three potentials look reasonably similar. As we move to higher energies the Dirac-Hara and HL potentials decrease reflecting the fact that high energy electrons will "see" less of the atomic potential. The Slater $X\alpha$ potential is on the other hand, energy independent. The Dirac-Hara potential falls off faster than real part of the HL potential with energy. In the outer regions of the atom, where the electron density is lower and the screening less important, the Dirac-Hara potential appears too small. We know that the HL potential gives good results for the EXAFS, it is the potential used in both the Daresbury EXAFS code [14] and its American equivalent [47]. However, the Dirac-Hara potential also gives good phase-shifts for EXAFS purposes [50]. In

fact Chou *et al* [51] state that the Dirac-Hara is *better* than the corresponding real part to the HL potential. EXAFS calculations mostly deal with high photoelectron energies. At these energies the scattering from the atomic core dominates and the details of the atomic potential in the low electron density regions at the edges of the muffin tins becomes less important.

4.2.2 The Average Potential

We can calculate the average imaginary part of the HL potential simply from,

$$V_{AVG}(k) = \frac{3}{r_{mt}^3}\int_o^{r_{mt}} V_I(r,k)r^2 dr. \tag{4.16}$$

In figure 4.4 we plot the average imaginary part of the potential against k for copper. The imaginary part of the potential has an average value of approximately 4.6eV over most of the range of energy appropriate to EXAFS data analysis. This is close to the canonical value of $4eV$ generally used to account for the extrinsic losses in LEED calculations for example [8]. The average imaginary part of the HL potential is also very similar for all atoms. This is a consequence of describing the atoms as shells of varying electron density.

Figure 4.4 also shows that the average potential falls off with increasing photon energy above the edge. This can also be deduced from equation (4.15). We only obtain a contribution from the delta function if,

$$\left|\frac{\frac{1}{2}q^2+\omega_q}{kq}\right| < 1. \tag{4.17}$$

Taking the limit of high photoelectron energy so that k becomes very large and $\frac{1}{2}k^2 >> \omega_p$ we find that we will always obtain a contribution from the delta function provided that $q < k$ and $q > \omega_p/k$. Then, at high k,

$$\begin{aligned} V_I &= \frac{\omega_p^2}{2}\int_{\frac{\omega_p}{k}}^{k}\frac{dq}{kw\omega_q} \\ &= \frac{\omega_p}{k}\left[\frac{1}{2}\log\left(\frac{kq_c}{\omega_p}\right)+\frac{\omega_p}{3q_c^2}\right], \end{aligned} \tag{4.18}$$

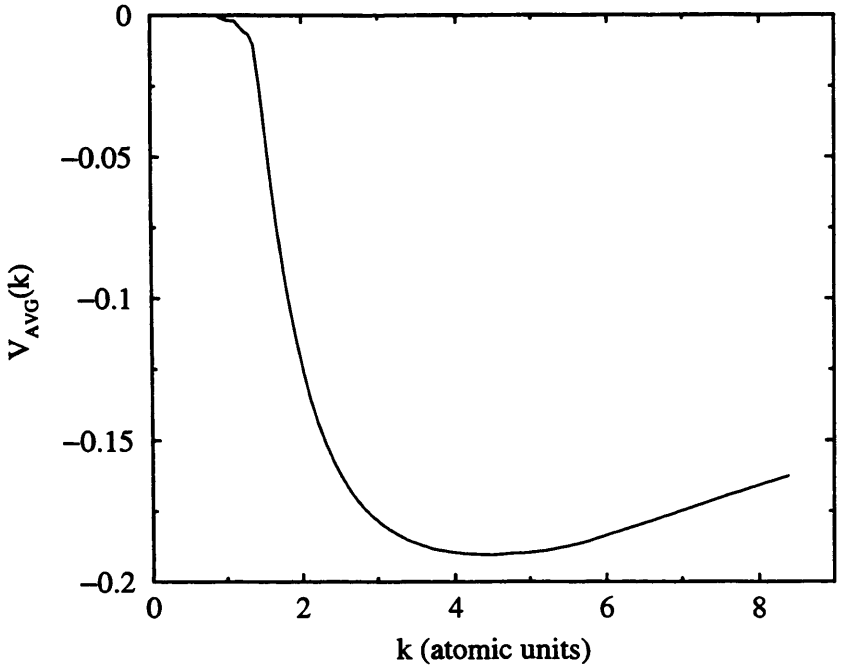

Figure 4.4: The average imaginary part of the HL potential plotted as a function of k for copper.

where, to a first approximation, we have approximated ω_q with its low q limit below q_c and with its high q limit of $\frac{1}{2}q^2$ above q_c. We can see that equation (4.18) for V_I will obviously go to zero as k becomes very large. V_I only models the extrinsic photoelectron scatterings and therefore this is correct.

4.2.3 The Isolated Atom

In Chapter 2 we calculated expressions which described the flux loss from the elastic photoelectron beam as the photoelectron propagated through a single muffin tin. In figure 4.5 we compare the results obtained to first and second order (eqn.(2.33) and eqn.(2.37)). In this figure, and the rest of the chapter we treat events following a K-edge photoionisation. In this way we need only consider the $l_f = 1$ final state.

The second order calculation can be used to give an estimate of the errors

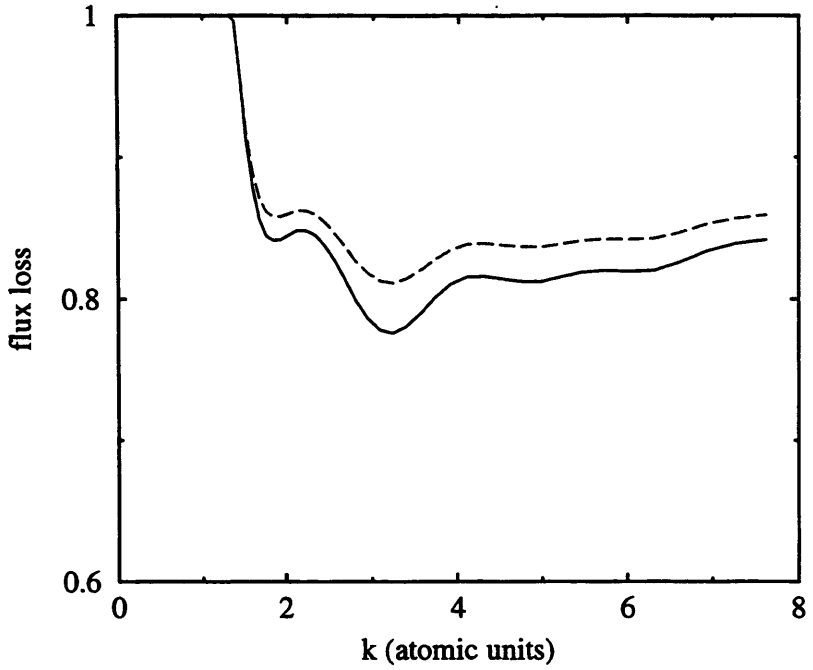

Figure 4.5: The loss of flux from the elastic photoelectron beam from an isolated atom calculated for copper. The solid line shows the result of the 1st order expression (eqn.(2.33)), the dashed line shows the result of the second order expression (eqn.(2.37)).

involved in the first order expression for the EXAFS amplitude which we shall examine in the next section. Over most of the energy range plotted in figure 4.5 the results of the two calculations differ by approximately 2%. To a first approximation we can ignore inelastic events at the scattering atom and write the EXAFS amplitude to first order as being proportional to $1 - 2k\langle R|V_I|R\rangle$. This would give results from the EXAFS amplitudes differing by about 5% between the first and second order calculations. This error is much smaller than the error associated with the amplitude fitting parameters used in EXAFS data analysis. We must also bear in mind that including higher order terms in the second order calculation would bring the curve down toward the first order result because of the opposing signs of the most important terms in each additional order.

In Chapter 2 we stated that the radial matrix element $\langle R_l|V_I|X_l\rangle$ in equation (2.58) was small in comparison to the phase-shifts, δ_l. In figure 4.6 we plot

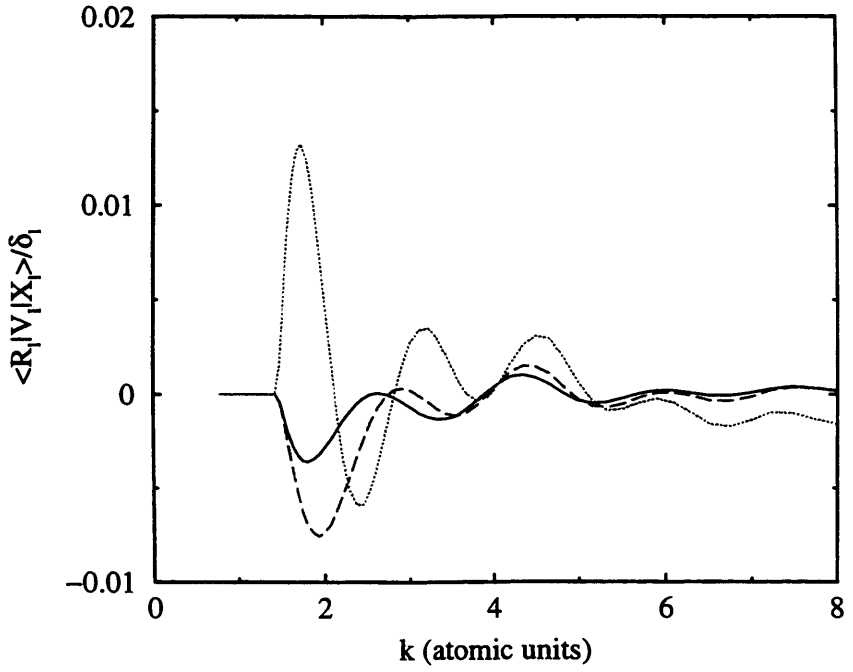

Figure 4.6: The matrix element $\langle R_l|V_I|X_l\rangle$ divided by the phase-shift δ_l at $l = 0$ (solid line), $l = 1$ (dashed line) and $l = 2$ (dotted line).

$\langle R_l|V_I|X_l\rangle/\delta_l$ against energy from $k = 0$ to 9 atomic units. We can see that for most of the energy range investigated $\langle R_l|V_I|X_l\rangle$ is much less than 1% of the phase-shifts. The neglect of this term in the calculation of the EXAFS amplitude (eqn.(2.59)) is therefore valid.

4.2.4 EXAFS Amplitudes

In figure 4.7 we plot the calculated EXAFS amplitude for copper (solid line) alongside the contribution to the EXAFS losses from inelastic processes at the central atom (dashed line) and from the inelastic processes at the scattering atom (dotted line).

To obtain the set of data denoted by diamonds in figure 4.7 we have examined the amplitudes of the EXAFS signals calculated using the HL and $X\alpha$ potentials respectively. EXCURV98 was used to calculate an EXAFS spectra for copper foil

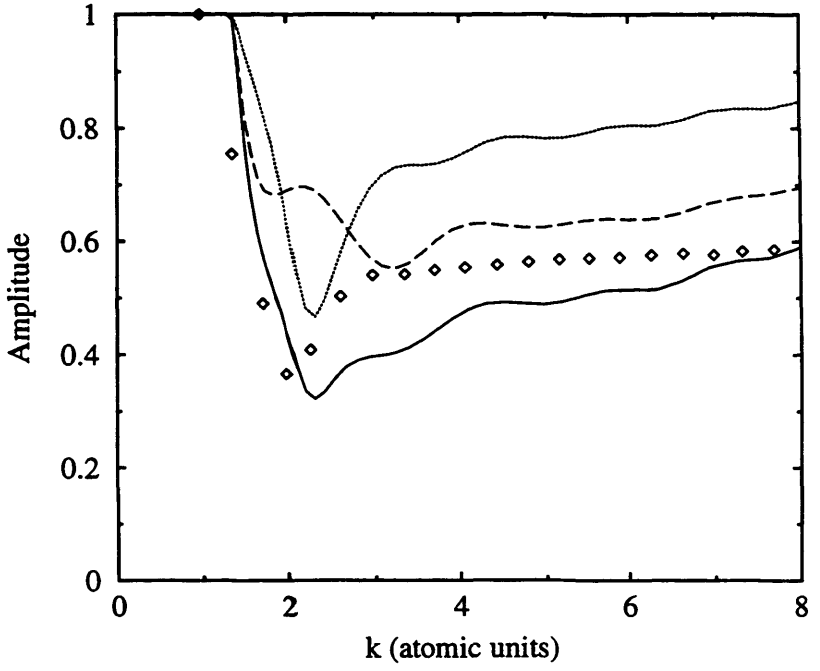

Figure 4.7: Calculated EXAFS amplitude for copper. The solid line shows the total result. The dashed line gives the contribution from the central atom muffin tin whilst the dotted line gives the contribution from the scattering atom. The diamonds are calculated using the Daresbury program EXCURV98.

using the HL potential. We refined the fit using the first shell only so that we could easily obtain the relevant path lengths for the electron mean free path losses. The refined fit gave a nearest neighbour distance of $r_1 = 2.541 \pm 0.006\mathring{A}$, a 1st shell coordination number of $n_1 = 11.3 \pm 1.5$, a Fermi energy of $E_f = -13.2 \pm 0.8$ and a Debye-Waller factor of $a_1 = 0.016 \pm 0.002$. These parameters were then used as input to recalculate the spectra using the real $X\alpha$ potential. The spectra calculated using the $X\alpha$ exchange is much larger than the best fit HL spectra as it includes none of the losses to the photoelectron beam from inelastic scattering.

The ratio of the peak heights can be used as an approximation to the losses given by the imaginary part of the HL potential. This data is shown by the diamonds in figure 4.7. The results from the 1st order calculation and the diamonds differ by an average of $\sim 8\%$ over the whole energy range. This gives

another measure of the uncertainty in the 1st order calculation. It is smaller than the comparable uncertainty in the EXAFS fitting parameters.

In figures 4.8, 4.9, and 4.10 we plot the EXAFS amplitude as a function of photoelectron wavevector in atomic units.

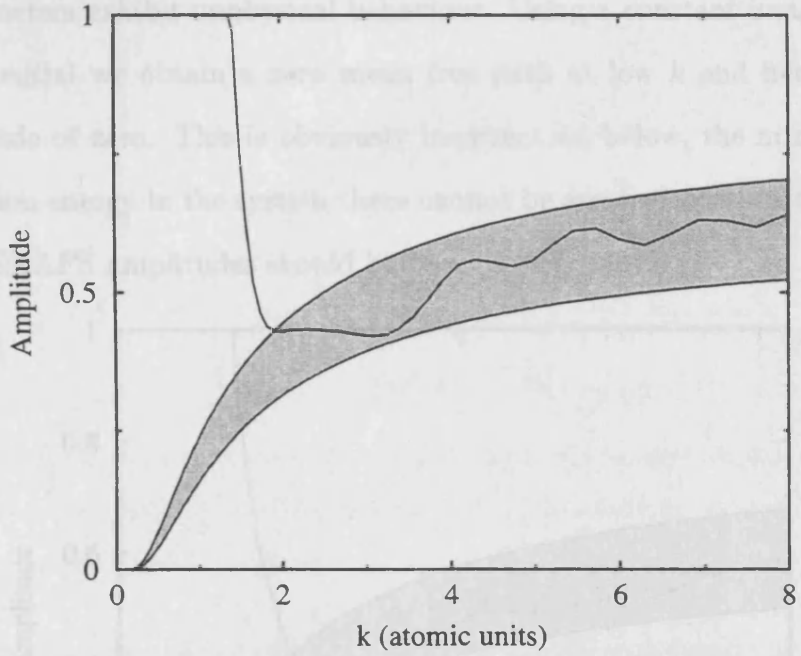

Figure 4.8: Calculated and best fit EXAFS reduction factors plotted against photoelectron wavevector for silicon. The black line gives the calculated result, the solid band shows the extent of the error in the best fit EXAFS amplitude.

The EXAFS amplitude is calculated using equation (2.59) for three elements: silicon, copper and silver. This is then compared to known values of the empirical parameters, $s_o^2(k)$ and $e^{-2r_j/\lambda(k)}$, fitted using the real X-alpha potential for the three elements with the data analysis program EXCURV98. The best fit values of s_o^2 and an effective, constant, imaginary potential, V_{PI}, were found to be [52] $s_o^2 = 0.72 \pm 0.1$ for silicon, $s_o^2 = 0.70 \pm 0.1$ for copper, and $s_o^2 = 0.67 \pm 0.15$ for silver. The V_{PI} values used were: $-4.0eV \pm 0.2eV$ for silicon, $-4.0eV \pm 0.2eV$ for copper and $-6.3eV \pm 0.2eV$ for silver where the quoted uncertainties are 2σ errors. The amplitude mean free path term is calculated from the constant imaginary

potential, V_{PI}, using the standard relation $\lambda(k) = k/V_{PI}$. In the figures the solid band shows the product of the fitted vales of s_o^2 and $e^{-2r_j/\lambda(k)}$ within the limit of experimental error whilst the black line gives the calculated EXAFS amplitude (eqn.(2.59)). Below a k of about 2 atomic units the historically used EXAFS reduction parameters exhibit unphysical behaviour. Using a constant imaginary part to the potential we obtain a zero mean free path at low k and hence an EXAFS amplitude of zero. This is obviously incorrect as, below, the minimum electron excitation energy in the system there cannot be any inelastic scatterings and hence the EXAFS amplitudes should be one.

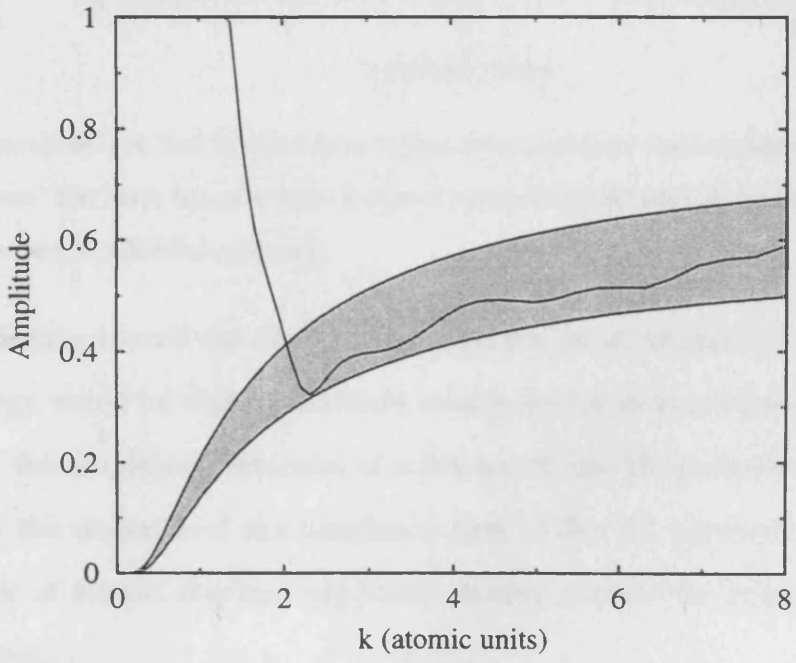

Figure 4.9: Calculated and best fit EXAFS reduction factors plotted against photoelectron wavevector for copper. The black line gives the calculated result, the solid band shows the extent of the error in the best fit EXAFS amplitude.

At low X-ray energies above the edge the calculated amplitude is unity. This is correct. At low energies the photoelectron is insufficiently energetic to excite a plasmon anywhere in the atomic muffin tin. The energy at which the amplitude begins to deviate from unity corresponds to the plasmon frequency in the region of

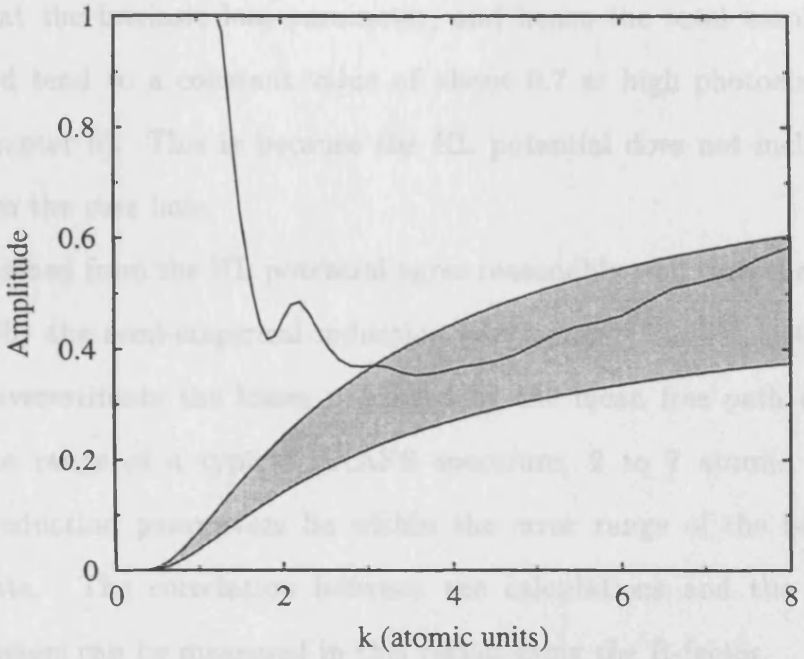

Figure 4.10: Calculated and best fit EXAFS reduction factors plotted against photoelectron wavevector for silver. The black line gives the calculated result, the solid band shows the extent of the error in the best fit EXAFS amplitude.

low electronic density toward the edge of the muffin tin. In an atomic calculation this cut-in energy would be that of the most weakly bound atomic orbital. The rapid cut-in of the amplitude reduction is a feature of the HL potential. This occurs because the majority of the imaginary part of the HL potential comes from the region of almost constant electronic density toward the edge of the muffin tin spheres.

At high k the HL potential overestimates the EXAFS amplitudes. The HL potential models the extrinsic loss effects and so, like the mean free path term it will disappear at high energies. From Figures 4.8, 4.9 and 4.10 it is clear that the calculated amplitudes are still increasing at $k = 8$ a.u.s. The HL potential itself varies as $1/k$ at large k, and, as the radial wavefunctions, $R_l(kr)$, are also proportional to $1/k$ at high energies, the EXAFS amplitudes given by the HL potential will obviously tend to unity. However, using the sudden approximation

we can show that the intrinsic loss parameter, and hence the total amplitude reduction, should tend to a constant value of about 0.7 at high photoelectron energies (see Chapter 6). This is because the HL potential does not include a contribution from the core hole.

The losses obtained from the HL potential agree reasonably well with the total reduction given by the semi-empirical reduction parameters. The HL potential must therefore overestimate the losses produced by the mean free path effects alone. Over the range of a typical EXAFS spectrum, 2 to 7 atomic units, the calculated reduction parameters lie within the error range of the best fit experimental data. The correlation between the calculations and the fitted empirical parameters can be measured in this region using the R-factor,

$$R = \frac{\sum |A_{expt} - A_{theory}|}{\sum |A_{expt}|} \times 100\%. \tag{4.19}$$

We find $R = 4.9\%$ for silicon, $R = 6.5\%$ for copper, and $R = 10.4\%$ for silver. These uncertainties are much lower than those observed in the best fit parameters for the various elements: 15.5% for silicon, 16.1% for copper and 24.4% for silver, which suggests that the reduction given by the HL potential is equivalent to that produced by the semi-empirical reduction parameters.

EXCURV98 was also used to fit values for the adjustable parameter, s_o^2, using the HL potential. We found values of $s_o^2(k) = 0.92 \pm 0.10$ for silicon, $s_o^2(k) = 1.05 \pm 0.05$ for copper and $s_o^2(k) = 1.02 \pm 0.05$ for silver. These values are all consistent with unity which suggests that additional amplitude fitting parameters should not be used when data fitting using the HL potential. It would appear that the HL potential gives extremely good results for EXAFS calculations, albeit accidentally.

Fitting the amplitude reduction parameter for a number of elements we obtain the points shown in figure 4.11. These points exhibit some scatter but are

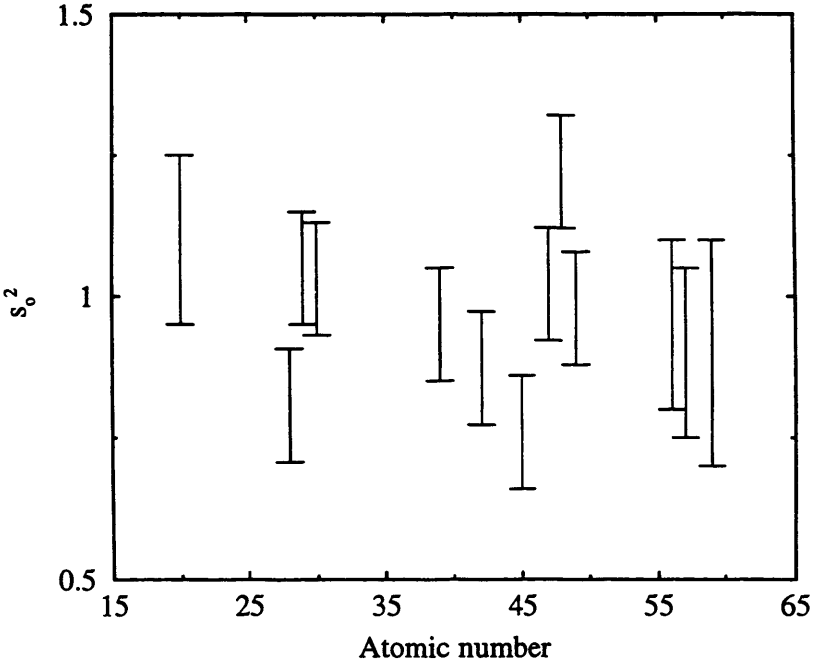

Figure 4.11: The amplitude reduction factor obtained by fitting EXAFS spectra using the HL potential with the Daresbury program EXCURV98. Plotted as a function of atomic number.

generally much larger than the values of s_o^2 which we would expect to obtain using the $X\alpha$ potential and a mean free path term. We therefore conclude that the HL potential significantly overestimates the extrinsic losses to the EXAFS amplitude. Empirically, the HL potential includes some of the contribution from the intrinsic loss events.

To summarise, the HL potential was designed to model the extrinsic loss effects. However, using equation (2.59) or the Daresbury program EXCURV98 we find that the imaginary part of the HL potential significantly overestimates the losses produced by the extrinsic effects alone. Instead it seems to, qualitatively, reproduce the total losses to the EXAFS amplitude even though the average imaginary part is consistent with the constant potential of $-4eV$ obtained from LEED experiments. The reason for this is the shape of the imaginary part of the HL potential. The average value would correctly account for the extrinsic

losses, however, the HL potential emphasises the middle and outer regions of the muffin tin as opposed to the region near to the nucleus where $r^2R_l(r)$ is small anyway and therefore overestimates the losses. This can be immediately seen from a calculation of the energy-dependent mean free path obtained from the HL potential.

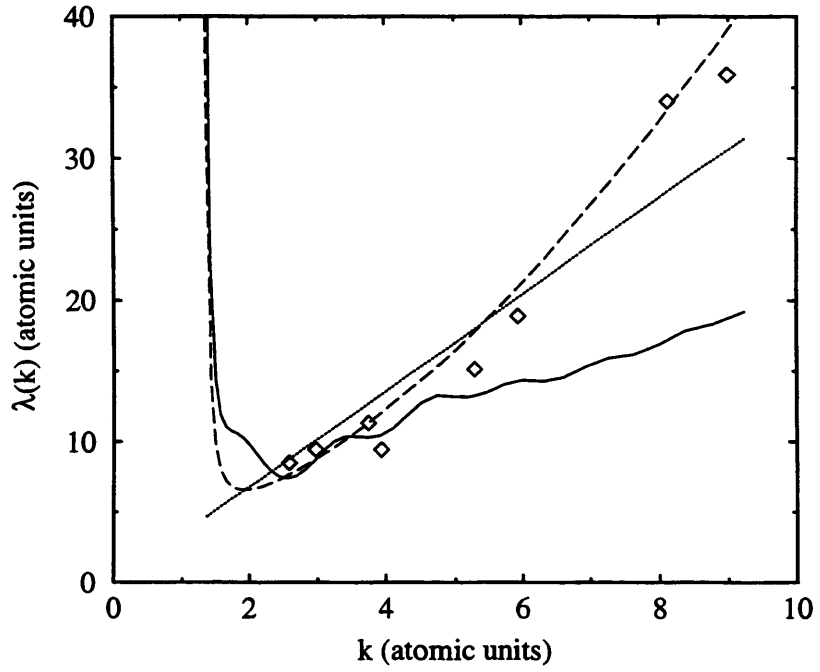

Figure 4.12: The energy-dependent mean free path in atomic units plotted against k in atomic units for aluminium. The solid line is that obtained from the imaginary part of the HL potential. The dashed line is calculated from the average imaginary part of the HL potential, the dotted line is that given by a constant imaginary potential of $-4eV$ and the diamonds are data reproduced from Penn [53].

In figure 4.12 we plot the mean free paths for aluminium obtained from three different calculations and compare to data reproduced from Penn [53]. In an isolated atom the loss of photoelectron flux is related to the mean free path by $\exp(-r_{mt}/\lambda(k))$ where λ is the relevant mean free path for flux. Equating this expression to equation (2.33) for the flux loss caused by the imaginary part of the HL potential we can immediately obtain an expression for the mean free path

given by the HL potential,

$$\lambda_{HL}(k) = \frac{-r_{mt}}{\log(1 + k\langle R_l|V_I|R_l\rangle)}. \tag{4.20}$$

In terms of a constant imaginary potential the flux mean free path can be written $\lambda(k) = \frac{k}{2V_{PI}}$.

In figure 4.12 we can see that the HL potential gives a mean free path that is much shorter than that found experimentally. The average part of the HL potential, however, reproduces the experimental results to much better accuracy and gives magnitudes for the mean free path comparable to those obtained from a constant imaginary potential of -4eV. The mean free path for both the HL potential and the average HL potential goes to infinity below the minimum plasmon excitation energy where no inelastic scattering events are possible.

To emphasise this result, the radially dependent HL potential is incorrect. It predicts values for the mean free path which are much too small. The average HL potential, on the other hand, gives values which agree tolerably well with experiment. It is the constant density, r independent, imaginary part of the HL potential (equivalent to the average HL potential) that, for example, Rehr *et al* [5] have claimed to give good agreement with the experimentally found mean free paths.

4.3 Conclusion

In this chapter we have outlined the derivation of the Hedin-Lundqvist exchange and correlation potential commonly used for EXAFS calculations. The real and imaginary parts of the potential have been calculated within the local density approximation for a number of different elements. The losses to the EXAFS given by the imaginary part of the potential were then examined using the method described in Chapter 2.

We find that the HL potential overestimates the losses to the EXAFS due to the finite photoelectron mean free path alone. However, it happens to give excellent agreement with the total experimental losses in the energy range of most EXAFS data analysis.

Empirically the HL potential seems to account for all of the losses to the EXAFS amplitudes. It should therefore not be necessary to use the amplitude fitting parameters s_o^2 and V_{PI} when data fitting using this potential. However the HL potential is "merely a phenomenological model that happens to work for the EXAFS" [25], by no means does it rigorously describe all the processes contributing to the inelastic scattering of the photoelectron. Effectively the HL potential underestimates the mean free path of the photoelectron leading to some *ad hoc* inclusion of the intrinsic effects. It is therefore possible that some further fitting of the amplitude using the variable parameters will be necessary when using the HL potential for EXAFS calculations.

Chapter 5

An Investigation of the Beni, Lee and Platzman Polarisation Potential

In the previous chapter we have shown that the HL potential, whilst giving reasonable agreement with EXAFS experiment, significantly overestimates the extrinsic photoelectron losses that it was designed to model. This may be because the HL potential does not include single electron excitations except by an appropriate weighting of the plasmons. The excitations of core levels and relatively localised states, such as the noble metal d-bands, will, however, exhibit atom-like behaviour. Thus modelling these excitations as plasmons will not, in general, be appropriate.

In 1976 Beni, Lee and Platzman (BLP) [17] derived a complex energy-dependent potential (the polarisation potential) which explicitly includes the one electron excitations although it neglects the plasmon excitations. This potential was used to calculate the scattering from the copper d-band and appeared to give reasonable results. In this chapter we investigate the BLP form of the polarisation potential without the simplifying approximations used by Beni, Lee and Platzman in an attempt to see if it will correct for the failings with the Hedin-Lundqvist form and if it may be considered as a viable alternative thereof.

BLP [17] derive their form for the polarisation potential by examining the

atomic scattering factor, $f(\boldsymbol{\eta})$. In the first Born approximation the atomic scattering factor is simply the Fourier transform of an effective scattering potential. However, $f(\boldsymbol{\eta})$ summed to all orders of scattering may also be evaluated in terms of the exact many-body wavefunctions of the system and the coulomb interaction potential. BLP obtain their form for the polarisation potential by equating the two results for $f(\boldsymbol{\eta})$. This method is explained in more detail in appendix B, however, in this chapter we show that the BLP form for the potential may also be derived using the GW formalism discussed in Chapter 3. By developing the polarisation potential via this method we can see why the potential describes correlation effects but does not include the electronic exchange, as stated by Lee and Beni [10].

We must start from the general form for the non-local self-energy derived in Chapter 3 (eqn.(3.14)). First we Fourier transform this result into energy and momentum space,

$$\Sigma(\mathbf{k}_i, \mathbf{k}_f, \omega) = \int e^{-\imath \mathbf{k}_i \cdot \mathbf{r}_1} e^{-\imath \mathbf{k}_f \cdot \mathbf{r}_2} \Sigma(\mathbf{r}_1, \mathbf{r}_2, \omega) d\mathbf{r}_1 d\mathbf{r}_2. \tag{5.1}$$

As we are again interested only in elastic scattering we chose the initial and final state photoelectron wavevectors to be $\mathbf{k}_i$ and $\mathbf{k}_f$ with $|\mathbf{k}_f|=|\mathbf{k}_i|$ and $\mathbf{k}_f - \mathbf{k}_i = \boldsymbol{\eta}$. To obtain the BLP potential we must evaluate the density operator matrix elements $\rho_{no}(\mathbf{q})$ within the Hartree approximation using bound atomic orbitals as the initial states, and continuum wavefunctions, $\psi_n(r)$, for the final states as in Chapter 3. Finally, we need to approximate $G(\mathbf{r}_1, \mathbf{r}_2, \omega - \omega_{no})$ as $G_o(\mathbf{k}_m, \omega - \omega_{no})$, the free electron Greens function. ie. the photoelectron states in the Greens function must be assumed to be plane waves. This immediately removes the dynamically screened exchange term from the result for the self-energy. As we are dealing with an atomic system (the Cu 3d orbital) there are no occupied plane wave states and thus the sum over occupied states in equation (3.14) will not contribute to the

final result. We are therefore left with a complex scattering potential containing only the contribution from the coulomb hole. This describes the electron-electron correlation. Thus, from equation (3.14), we have,

$$\begin{aligned}\Sigma(\mathbf{k}_i,\mathbf{k}_f,\omega) &= -\frac{1}{(2\pi)^9}\int d\mathbf{r}_1 d\mathbf{r}_2 d\mathbf{q}_1 d\mathbf{q}_2 d\mathbf{k}_m e^{\imath(\mathbf{q}_1-\mathbf{k}_i+\mathbf{k}_m)\cdot\mathbf{r}_1} e^{\imath(\mathbf{q}_2-\mathbf{k}_i+\mathbf{k}_m)\cdot\mathbf{r}_2} \\ &\times \quad v_{\mathbf{q}_1} v_{\mathbf{q}_2} \sum_n \frac{\rho_{no}(\mathbf{q}_1)\rho^*_{no}(\mathbf{q}_2)}{\omega - \frac{1}{2}k_m^2 - \omega_{no} + \imath\delta},\end{aligned} \tag{5.2}$$

where $\omega_{no} = \omega_n - \omega_o$ and we have removed the sum over initial states because we are only dealing with a single copper 3d orbital. Ideally we should sum over the initial states of all the electrons available to scatter the incoming photoelectron. Beni, Lee and Platzman, however, only calculate the contribution to f_2 from the 3d orbital in copper arguing that the scattering from this weakly bound state will dominate over that from the more deeply bound core orbitals.

The $\mathbf{r}_1$ and $\mathbf{r}_2$ integrals in equation (5.2) simply give $2\pi^3\delta(\mathbf{k_m} - \mathbf{k}_i - \mathbf{q})$ and $2\pi^3\delta(\mathbf{q}_2 - \boldsymbol{\eta} + \mathbf{q})$ respectively. To obtain the standard form for the polarisation potential we have written $\mathbf{q} = -\mathbf{q}_1$. Then, assuming the initial photoelectron energy, far from the atom, to be $\omega = \frac{1}{2}k_i^2$ we find that,

$$\Sigma(\boldsymbol{\eta}, \frac{1}{2}k_i^2) = -\frac{4}{\pi}\int d\mathbf{q} \sum_n \frac{\langle\phi_o|e^{\imath\mathbf{q}\cdot\mathbf{r}}|\psi_n\rangle\langle\psi_n|e^{\imath(\boldsymbol{\eta}-\mathbf{q})\cdot\mathbf{r}}|\phi_o\rangle}{q^2|\,\mathbf{q}-\boldsymbol{\eta}\,|^2(q^2 + 2qk_i x + 2\omega_{no} - \imath\delta)}. \tag{5.3}$$

We have written $x = \cos\theta$, where θ is the angle between the wavevectors $\mathbf{k}_i$ and $\mathbf{q}$. As $f(\boldsymbol{\eta}) = \frac{1}{2\pi}\Sigma(\boldsymbol{\eta}, \frac{1}{2}k_i^2)$ equation (5.3) gives an identical result to that produced by BLP. Equation (5.3) is therefore simply the Fourier transform of an effective complex scattering potential. This potential may be added to the Hartree potential to give a one-body approximation to the full interaction potential. Intuitively we would expect the polarisation potential to be more physically accurate than the equivalent HL form for the potential. The BLP form explicitly includes one electron excitations from bound states into the continuum because of its inclusion of the atomic single electron form of the inverse dielectric function

(eqn.(3.22)). The BLP potential also includes inelastic effects because, whenever an inelastic scattering channel opens up at $\omega - \frac{1}{2}k_m^2 - \omega_{no}$, the energy denominator in equation (5.2) goes to zero and we obtain an imaginary contribution to the scattering factor.

5.1 Calculation of the Polarisation Potential

We can now use equation (5.3) to evaluate an r dependent polarisation potential without the simplifying approximations used by Beni, Lee and Platzman.

In their original paper, BLP calculate the second Born approximation to the scattering factor, and hence the polarisation potential, using a spherically symmetric initial state for the copper 3d electrons and orthogonalised plane waves for the continuum final state wavefunctions. For the sake of computational efficiency they also split the range of the q integral, replacing the integrand in equation (5.3) with approximate forms valid in the limits of $q \ll \eta$ and $q \gg \eta$.

We calculate $\Sigma(\eta, \frac{1}{2}k_i^2)$ using full Clementi wavefunctions for the initial 3d state and exact numerical results for the final state wavefunctions. We are also able to perform the integrals in equation (5.3) without approximating the integrand. However, because we wish to calculate the polarisation potential for copper metal, we encounter a problem in that the copper 3d orbital extends beyond the edge of the atomic muffin tin sphere. We deal with this problem in a fashion suggested by Pendry [8]. We assume that the influence of the neighbouring atoms is to push the overlapping wavefunction back inside its own muffin tin sphere. Although a particular muffin tin may lose charge because its own functions overlap the muffin tin boundary it will also gain charge from the overlap of wavefunctions from neighbouring atoms. This is taken into account by truncating the 3d wavefunction at the muffin tin boundary and increasing its amplitude within to give the correct

number of electrons in the level.

Equation (5.3) can be immediately Fourier transformed into r space. We change variable from $\boldsymbol{\eta}$ to $\mathbf{k} = \mathbf{q} - \boldsymbol{\eta}$, then, rewriting the sum over final states as an integral over the free electron density of states, we find that,

$$\Sigma(\mathbf{r}, \frac{1}{2}k_i^2) = -\frac{4}{\pi}\sum_{m_o}\int d\mathbf{q}d\mathbf{k}d\mathbf{k}_n e^{i(\mathbf{k}-\mathbf{q})\cdot\mathbf{r}}\frac{\langle\phi_o|e^{i\mathbf{q}\cdot\mathbf{r}}|\psi_n\rangle\langle\psi_n|e^{i(\boldsymbol{\eta}-\mathbf{q})\cdot\mathbf{r}}|\phi_o\rangle}{q^2k^2(q^2+2qk_ix+2\omega_{no}-i\delta)}, \quad (5.4)$$

where $\mathbf{k}_n$ is the wavevector of the excited state ψ_n and we have summed over the contribution from each of the degenerate m_o initial states. The continuum wavefunctions are defined as in equation (2.5) so that the angular parts of the $\mathbf{k}_n$ integral may be easily performed. Then, expanding the exponentials in the matrix elements in an angular momentum sum (eqn.(3.41)), and replacing the $\mathbf{r}$ dependent initial states with $\phi_{l_o}(r)Y_{l_om_o}(\hat{r})$, we may write,

$$\begin{aligned}\Sigma(\mathbf{r}, \frac{1}{2}k_i^2) &= -\frac{4}{\pi^3}\sum_{\substack{l_f\\m_f,m_o}}\sum_{\substack{L,M\\L',M'}}\int\frac{d\mathbf{q}d\mathbf{k}k_n^2dk_n e^{i(\mathbf{k}-\mathbf{q})\cdot\mathbf{r}}Y_{LM}(\hat{q})Y_{L'M'}(\hat{k})}{q^2k^2(q^2+2qk_ix+2\omega_{no}-i\delta)}\langle R_{l_f}|j_L(qr')|\phi_{l_o}\rangle \\ &\times \langle\phi_{l_o}|j_{L'}(kr'')|R_{l_f}\rangle\int d\hat{r'}Y_{lm}Y_{LM}Y_{l_om_o}\int d\hat{r''}Y_{l_om_o}Y_{L'M'}Y_{lm}. \quad (5.5)\end{aligned}$$

The angular integrals are identical to those encountered in Chapters 2 and 3. They may be expressed in terms of the Wigner-3j coefficients [29]. Within the muffin tin approximation we are also only interested in spherically symmetric potentials, thus, expanding the remaining exponentials and averaging $\Sigma(\mathbf{r}, \frac{1}{2}k_i^2)$ over the directions of $\mathbf{r}$, we have,

$$\begin{aligned}\Sigma(r, \frac{1}{2}k_i^2) &= -\frac{2}{\pi^3}\sum_{l,l_o,L}A_{l,l_o,L}\int\frac{k_n^2dk_ndqdkdx}{q^2+2qk_ix+2\omega_{no}-i\delta}j_L(qr)j_L(kr) \\ &\times \langle R_{l_f}|j_L(qr')|\phi_{l_o}\rangle\langle\phi_{l_o}|j_L(kr'')|R_{l_f}\rangle, \quad (5.6)\end{aligned}$$

where $\omega_n = \frac{1}{2}k_n^2$ and,

$$A_{l_f,l_o,L} = (2l_f+1)(2l_o+1)(2L+1)\begin{pmatrix} l_f & l_o & L \\ 0 & 0 & 0\end{pmatrix}^2. \quad (5.7)$$

The dx integral in equation (5.6) may be written as,

$$\int_{-1}^{1} \frac{dx}{q^2 + 2\omega_{no} + 2qk_i x - \imath\delta} = \log\left|\frac{q^2 + 2\omega_{no} + 2qk_i}{q^2 + 2\omega_{no} - 2qk_i}\right| + \imath\pi \int_{-1}^{1} dx \delta(q^2 + 2\omega_{no} + 2qk_i x). \quad (5.8)$$

The dk integral in equation (5.6) may also be performed analytically. We can use the relation, $j_l(kr) = \left(\frac{\pi}{2kr}\right)^{\frac{1}{2}} J_{L+\frac{1}{2}}(kr)$ to express the integral over the spherical Bessel functions in terms of the hypergeometric function, ${}_2F_1$ [54],

$$\int_0^\infty j_L(kr) j_L(kr') dk = \frac{\pi}{2(rr')^{\frac{1}{2}}} \int \frac{1}{k} J_{L+\frac{1}{2}}(kr) J_{L+\frac{1}{2}}(kr') dk$$
$$= \frac{\pi}{2(rr')^{\frac{1}{2}}} \frac{(rr')^{L+\frac{1}{2}}}{2(r+r')^{2L+1}(L+\frac{1}{2})} {}_2F_1\left\{L + \frac{1}{2}, (L+1); 2L+2; \frac{4rr'}{(r+r')^2}\right\}. \quad (5.9)$$

This expression may be simplified using a standard result for ${}_2F_1$ taken from 'Formulas and Theorems for the Special Functions of Mathematical Physics' [55],

$${}_2F_1(a, a + \frac{1}{2}; 2a+1; z^2) = 2^{2a}[1 + (1-z^2)^{\frac{1}{2}}]^{-2a}. \quad (5.10)$$

We obtain different results for the integral over the spherical Bessel functions depending on whether r or r' is the larger.

$$\int_o^\infty j_L(kr) j_L(kr') dk = \frac{\pi}{4\left(L + \frac{1}{2}\right)} f_L(r, r'), \quad (5.11)$$

where,

$$f_L(r, r') = \left(\frac{r'}{r}\right)^L \frac{1}{r} \qquad r \geq r'$$
$$= \left(\frac{r}{r'}\right)^L \frac{1}{r'} \qquad r' \geq r. \quad (5.12)$$

We can now substitute relations (5.8) and (5.11) into equation (5.6) to obtain the final results for the real and imaginary parts of the BLP polarisation potential. Multiplying by a factor of two to account for spin degeneracy in our (presumed

full) copper d-band we have,

$$V_R(r,\frac{1}{2}k_i^2) = -\frac{2}{\pi^3}\sum_{l_f,l_o,L}\frac{A_{l_f,l_o,L}}{L+\frac{1}{2}}\int_0^\infty dq\int_0^\infty dk_n k_n^2 \log\left|\frac{q^2+k_n^2+2|\omega_o|+2qk_i}{q^2+2k_n^2+2|\omega_o|-2qk_i}\right| \times j_L(qr)\langle R_{l_f}|f_L(r,r')|\phi_{l_o}\rangle\langle\phi_{l_o}|j_L(qr'')|R_{l_f}\rangle \quad (5.13)$$

and,

$$V_I(r,\frac{1}{2}k_i^2) = -\frac{1}{2\pi}\sum_{l_f,L}\frac{A_{l_f,L,l_o}}{\left(L+\frac{1}{2}\right)}\int_{q_{min}}^{q_{max}} dq\int_{-1}^{x_{max}} dx k_n j_L(qr)\langle R_{l_f}|f_L(r,r')|\phi_{l_o}\rangle \times \langle\phi_{l_o}|j_L(qr'')|R_{l_f}\rangle\delta\left(k_n-(-2|\omega_o|-q^2-2qk_ix)^{\frac{1}{2}}\right), \quad (5.14)$$

where,

$$\begin{aligned} q_{min} &= k_i-(k_i^2-2|\omega_o|)^{\frac{1}{2}} \\ q_{max} &= k_i+(k_i^2-2|\omega_o|)^{\frac{1}{2}} \\ x_{max} &= -\frac{q}{2k_i}-\frac{|\omega_o|}{qk_i}. \end{aligned} \quad (5.15)$$

We have written the real part of $\Sigma(r,\frac{1}{2}k_i^2)$ as V_R and the imaginary part as V_I. These results can be made more general by summing over all of the n_o and l_o initial states and multiplying by the fractional occupancy of each state.

5.2 The Average Self-Energy

Beni, Lee and Platzman calculate a quantity they define as the imaginary part of the electron self-energy from the 2nd Born correction to the atomic scattering factor,

$$Im\,\Sigma = 2\pi N_I Im\, f_2(0), \quad (5.16)$$

where N_I is the ion density. This result is, in fact, just the self-energy at $\eta = 0$ averaged over the volume of the solid. This is equal to the average value of the imaginary part of the r-dependent polarisation potential and is closely

related to the imaginary part of the local inverse dielectric function (eqn.(3.23)). Substituting for $\eta = 0$ into equation (5.3) we have,

$$\Sigma(0, \frac{1}{2}k_i^2) = -\frac{4}{\pi}\int d\mathbf{q} \sum_n \frac{|\langle\psi_n|e^{\imath\mathbf{q}\cdot\mathbf{r}}|\phi_{l_o}\rangle|^2}{q^4(q^2 + 2qk_ix + 2\omega_{no} - \imath\delta)}. \tag{5.17}$$

Thus,

$$Im\,\Sigma(0, \frac{1}{2}k_i^2) = -\int d\mathbf{q}\frac{4}{q^4}\sum_n |\langle\psi_n|e^{\imath\mathbf{q}\cdot\mathbf{r}}|\phi_{l_o}\rangle|^2\,\delta(2\omega_{no} + q^2 + 2qk_ix), \tag{5.18}$$

where the delta function is given by,

$$\delta(2\omega_{no} + q^2 + 2qk_ix) = -\frac{1}{2k_n}\delta(k_n - (-2|\omega_o| - q^2 - 2qk_ix)^{\frac{1}{2}}). \tag{5.19}$$

Equation (2.5) may again be used to substitute for the continuum wavefunctions. Then, rewriting the sum over excited states as an integral over the density of states and summing over the degenerate m_o levels of the initial 3d state we can easily perform the angular integrals in the same manner as in the previous section. We find that,

$$Im\,\Sigma(0, \frac{1}{2}k_i^2) = \sum_{L,l}\int_{q_{min}}^{q_{max}} dq \int_{-1}^{x_{max}} dx\frac{k}{q^2}\,|\langle R_{l_f}(kr)|j_L(qr)|\phi_{l_o}(r)\rangle|^2\,A_{l_o,l,L}, \tag{5.20}$$

where $k = (-2|\omega_i| - q^2 - 2qk_ix)^{\frac{1}{2}}$ and the limits of the integrals are given by results (5.15). Comparing this result to equation (3.44) we can see that the average value of the polarisation potential may may expressed simply in terms of the imaginary part of the dielectric function,

$$Im\,\Sigma(0, \frac{1}{2}k_i^2) = -\frac{1}{\pi}\int_{q_{min}}^{q_{max}}\int_{-1}^{x_{max}} Im\,\epsilon_{3d}^{-1}(q, -\frac{1}{2}q^2 - qk_ix)dxdq. \tag{5.21}$$

The limits of the integrations are such that $-\frac{1}{2}q^2 - qk_ix > 0$. In order that we may compare our results directly with BLP we have taken $Im\,\epsilon_{3d}^{-1}(q,\omega)$ to be the contribution to the imaginary part of the dielectric function from the 3d orbitals only. As we have already evaluated $Im\,\epsilon^{-1}(q,\omega)$ for a number of cases we

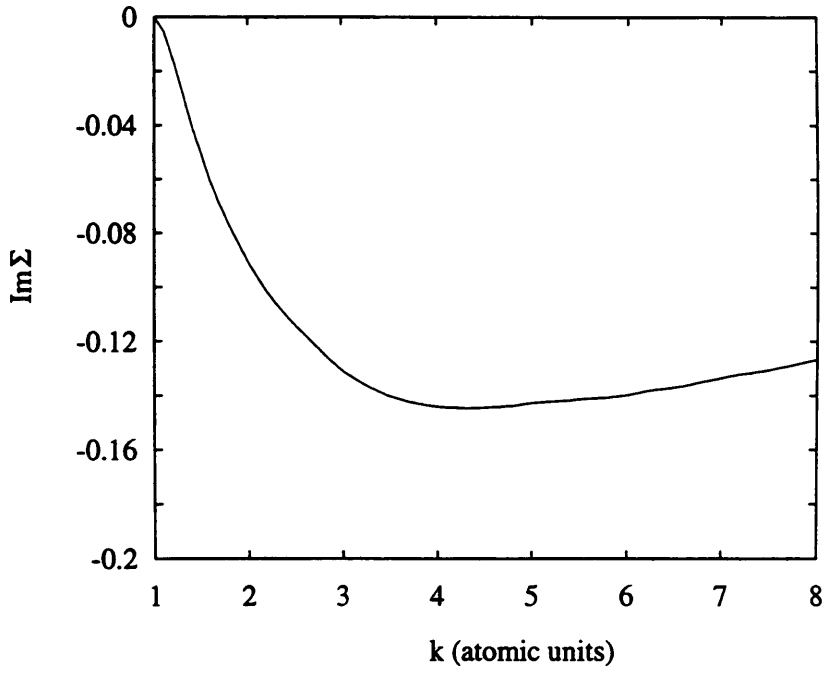

Figure 5.1: The average imaginary part of the polarisation potential in Hartrees as a function of incident photoelectron wavevector, where $\omega = \frac{1}{2}k_i^2$.

may easily calculate $Im\,\Sigma(0, \frac{1}{2}k_i^2)$ as a function of the momentum of the incident photoelectron. This is plotted in figure 5.1.

The average value of the imaginary part of the polarisation potential varies slowly with energy over the range of incident photoelectron momenta appropriate to the EXAFS. The average imaginary potential is zero for photoelectrons of energy less than the binding energy of the copper 3d state, as, in this approximation, no secondary electron excitations are possible below this energy. $Im\,\Sigma(0, \frac{1}{2}k_i^2)$ peaks at a value of approximately $3.8eV$. This is comparable in size to the results obtained by BLP and agrees reasonably well with the $-4eV$ magnitude for the constant imaginary part of the potential assumed in most LEED calculations.

5.3 Results

We can now calculate numerical results for the real and imaginary parts of the polarisation potential using equations (5.13) and (5.14). The details of the calculation are much the same as in Chapter 3. The copper 3d orbitals are again approximated by the Roothaan-Hartree-Fock states tabulated by Clementi and Roetti [26] and the regular solutions to the Schrödinger equation, $R_{l_f}(kr)$, are calculated using the Runga-Kutta routine described in Chapter 2. The calculations are performed within the muffin tin approximation of Loucks where we have assumed the spherical potential to be the sum of the Hartree potential and the Slater exchange. As we are treating copper metal rather than copper atoms we cannot use the values of the free electron exchange parameter, α, tabulated by Schwarz [44]. Instead we set α by examining full band structure calculations. This procedure is detailed later.

5.3.1 The Imaginary Part

We begin by calculating the imaginary part of the BLP polarisation potential. The integrals are performed using a simple trapezium rule routine on a linear grid where the point density may be increased until the integrals have converged. The sum over plane wave angular momenta is converged as in the calculation of $\epsilon^{-1}(q,\omega)$. This introduces an error of $\sim \pm 1.0\%$ into the final results for the polarisation potential.

We find that our results for the imaginary part of the polarisation potential depend critically on the details of the muffin tin potential and the magnitude of the Fermi energy. The calculation of $V_I(r, \frac{1}{2}k_i^2)$ is much more sensitive to the final state phase-shifts, and hence the d-band occupancy, than was the calculation of $\epsilon^{-1}(q,\omega)$. The muffin tin potential can be altered by varying the parameter α in

the Slater exchange potential (eqn.(3.50)).

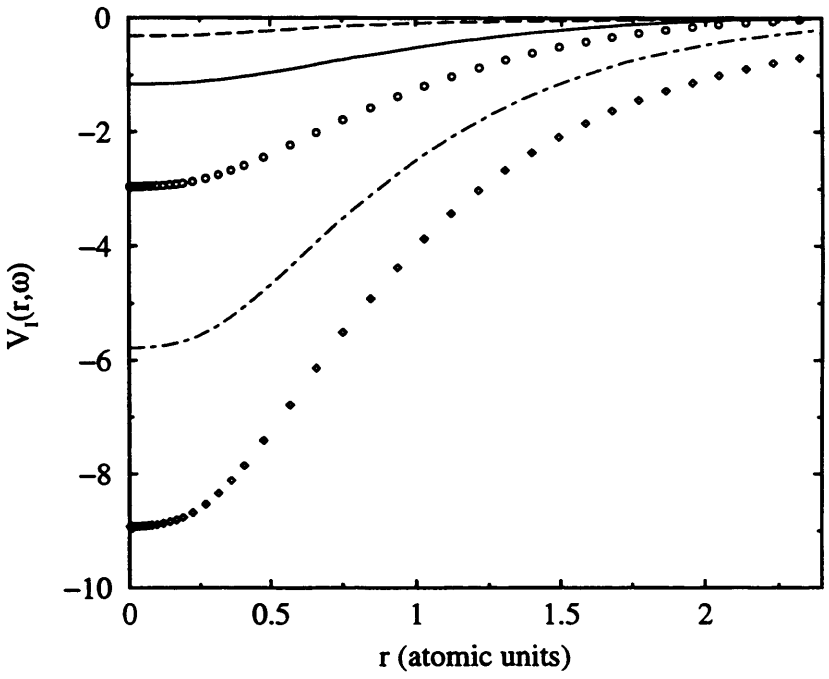

Figure 5.2: The imaginary part of the polarisation potential in Hartrees as a function of r plotted at $k_i = 2$ atomic units for a range of values of the Slater exchange parameter, $\alpha = 0$ (solid curve), $\alpha = 0.25$ (circles), $\alpha = 0.5$ (dot-dash line), $\alpha = 0.75$ (diamonds) and $\alpha = 1.0$ (dashed line).

In figure 5.2 we plot V_I against r for a range of values of α at $k_i = 2$ atomic units with a Fermi energy of zero. The potential varies over approximately a full order of magnitude, which is clearly unacceptable. To calculate V_I accurately we should first find the real part of the polarisation potential using some self consistent calculation then use V_R to calculate the phase-shifts needed to evaluate the imaginary part of the potential. This is, however, a time consuming and computationally intensive procedure. We therefore attempt to approximate the effects of exchange and correlation using the Slater exchange potential with definite, fixed, values of α and E_f. We set the Slater exchange parameter and the Fermi energy by using the Friedel sum rule to calculate the d-band occupancy

in terms of the final state phase-shifts. We first fix α so that the centre of the d-band is at an energy which agrees with band structure calculations, then set E_f to obtain the correct occupancy.

Friedel Sum Rule

To make use of the Friedel sum rule we consider the atom interacting with the X-ray photon to be an impurity added to the free electron continuum. The charge on this impurity must be normalised by extra electrons within a finite distance in such a way that the chemical Fermi energy remains unchanged at large distances from the impurity. This leads to an additional density of states in the region of the central atom [39],

$$\Delta N(E) = \frac{2}{\pi}\sum_l (2l+1)\frac{d\delta_l}{dE}. \tag{5.22}$$

The number of electrons in a certain l state is then obtained by integrating equation (5.22) and adding the number already present in the free electron density of states,

$$N(E) = \frac{2}{\pi}\sum_l (2l+1)\delta_l + \frac{2\sqrt{2}}{3\pi^2}VE^{\frac{3}{2}}, \tag{5.23}$$

where V is the atomic volume. For the copper 3d band the impurity states dominate over the continuum states but the presence of the continuum states is much more important in jellium-like metals such as Aluminium. We can use equation (5.23) to calculate the d-band occupancy from the final state phase-shifts by setting $l = 2$. For copper, where the impurity states dominate the free electron states, we will obtain a full d-band at energies where $\delta_2 \sim \pi$.

In the left hand graph of figure 5.3 we plot $\delta_2(E)$ against energy for $\alpha = 1.0, 0.75$ and 0.5. We obtain an atomic-like d-band with $\alpha = 1.0$. This has zero width and is completely bound. $\alpha = 0.75$ gives a d-band of narrow but finite width ($\sim$ 0.1 Hartrees). To fill the d-band given by this value of the Slater exchange

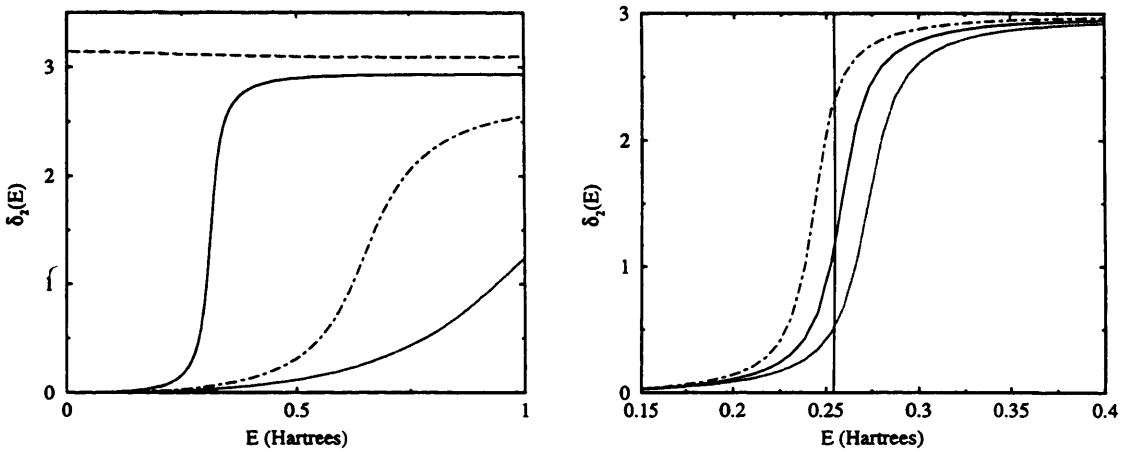

Figure 5.3: copper d phase-shifts as a function of energy. In the graph on the left the dotted line is calculated with the Slater exchange parameter, $\alpha = 0.25$, the dot-dash line with $\alpha = 0.5$, the solid line with $\alpha = 0.75$ and the dashed line with $\alpha = 1.0$. The graph on the right shows the d phase-shifts on an expanded scale calculated with $\alpha = 0.79$ (solid line), $\alpha = 0.80$ (dotted line) $\alpha = 0.78$ (dashed line).

parameter we would need to set E_f above 0.4 Hartrees as it is not until this value that δ_2 reaches its maximum value. With values of $\alpha < 0.5$ we obtain extremely broad d-bands. From figure 5.3 we can immediately see why the magnitude of the imaginary part of the potential varies with α as it does. By setting $\alpha = 0.5$, for example, we allow the possibility of resonant transitions into unoccupied d-states in the continuum. As there is consequently a high probability of the bound electrons being excited by the photoelectron there must be a correspondingly large imaginary part to the scattering potential.

The right hand plot of figure 5.3 shows the $l = 2$ phase-shifts against energy on an expanded scale. Full band structure calculations reproduced by Harrison [56] show the centre of the copper d-band to be at 0.252 Hartrees. By examining the phase-shifts we can clearly see that we need to set $\alpha \sim 0.79$ to obtain this.

The d-band in copper is occupied up to the Fermi energy, E_f. For copper metal

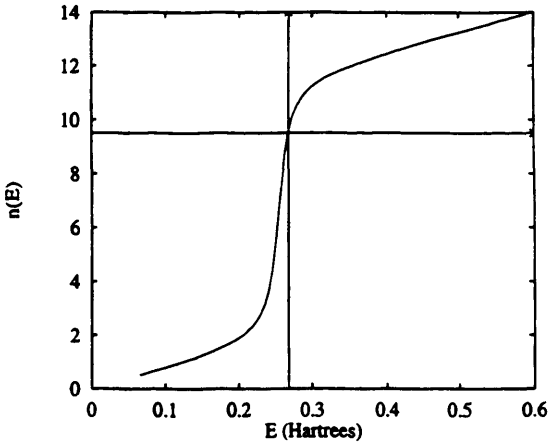

Figure 5.4: Occupancy of the copper d-band plotted against energy with $\alpha = 0.79$. The horizontal solid line marks $n(E) = 9.5$ whilst the vertical solid line is at $E = 0.268$ Hartrees.

the electron configuration will not be exactly as it would in a free atom ($3d^{10}4s^1$) but will probably have a character more like $3d^{9.5}4s^{1.5}$. We must therefore set the Fermi energy so that filling the d-band up to E_f results in an occupancy of ~ 9.5 electrons. In figure 5.4 we plot the number of electrons calculated from equation (5.23) against the energy. A Fermi energy of $E_f = 0.268$ Hartrees ($7.3eV$) must be used to obtain the correct occupancy. Schwarz [44] records a value of $\alpha = 0.706$ for a free atom of copper. Using this value of α we would need to set E_f to an unfeasibly high level in order to obtain the correct d-band occupancy. Figure 5.4 also shows why the calculation is so sensitive to the value chosen for the Fermi energy. Varying E_f by a few eV's results in large changes to the d-band occupancy. This in turn greatly effects the probability of exciting a secondary electron, especially for low energy photoelectrons, where the majority of the energetically possible excitations would be into the low lying d states if these were unoccupied.

Numerical Results

Using the fixed values of α and E_f we can now calculate the imaginary part of the polarisation potential for the copper d-band. In figure 5.5 we plot $V_I(r, \frac{1}{2}k_i^2)$ against r for a range of incident photoelectron energies. We obtain magnitudes

for the imaginary part of the potential which are very similar to BLP's. However, the energy dependence is not the same and the variation with r is slightly different in that the BLP polarisation potential falls off faster in the outer regions of the muffin tin spheres. These slight differences are not surprising. Both the energy dependence and r dependence of the potential vary significantly with both α and E_f. Also we would expect the different final states used by BLP to affect the shape of the potential.

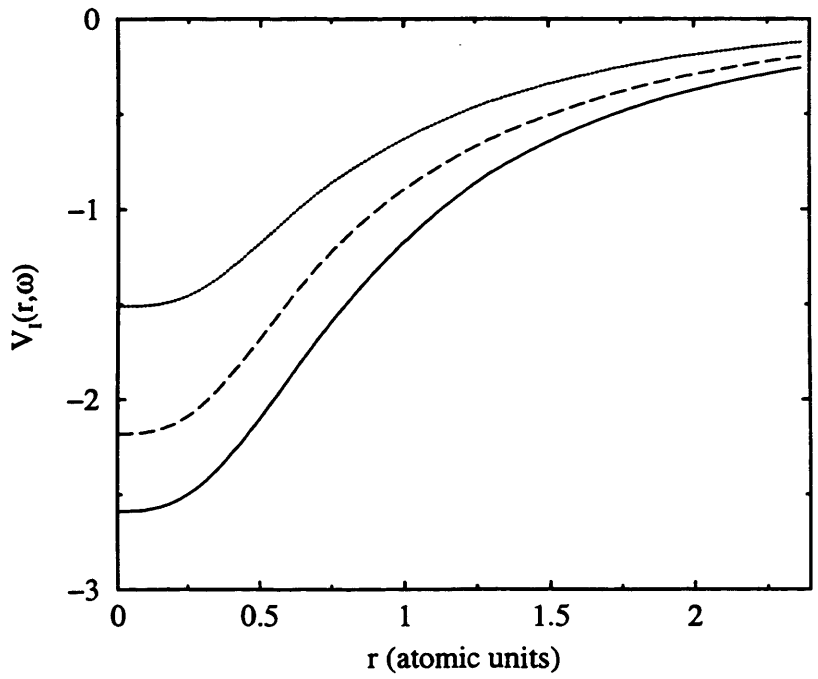

Figure 5.5: The imaginary part of the polarisation potential in Hartrees plotted against r at $k_i = 2$ (solid line), $k_i = 4$ (dashed line) and $k_i = 6$ atomic units (dotted line).

As we increase the energy of the incident photoelectron the imaginary part of the potential decreases. This is as we would expect. An extremely energetic photoelectron incident on a scattering atom will not significantly interact with the electrons in that atom. There is therefore little probability of secondary electron excitation and correspondingly only a small imaginary part to the polarisation

potential for high energy photoelectrons.

The potentials shown in figure 5.5 are much larger than the corresponding Hedin-Lundqvist potentials calculated in chapter 4, thus the imaginary part of the polarisation potential will give EXAFS amplitudes which are much smaller than those observed experimentally. The flux of the elastically scattered photoelectron wave will be almost completely killed by the BLP form for V_I. As V_I is large we cannot use the first order expansion described in Chapter 4 to calculate the EXAFS amplitudes directly, but we can use the second order expansion (eqn.(2.37)) to examine the loss of flux of the photoelectron wave in the presence of an isolated atom. In figure 5.6 we plot the photoelectron flux normalised to unity from equation (2.37) against the incident photoelectron wavevector in atomic units. The flux is much smaller than in the presence of the imaginary part of the HL potential (fig. 4.5).

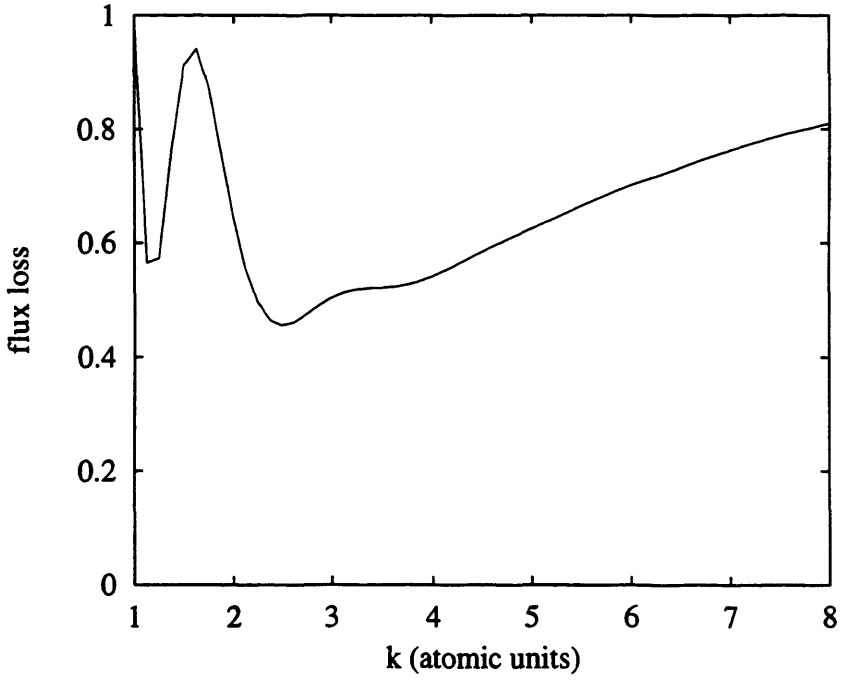

Figure 5.6: The loss of flux from the elastic photoelectron beam for an isolated copper atom calculated as a function of incident wavenumber in atomic units.

We can use this result to obtain a crude estimate to the EXAFS amplitudes. If we assume that the photoelectron may only be scattered inelastically at the central atom then the EXAFS amplitude is given by $1 - 2 \times (1 - \text{flux loss})$. This simple approximation underestimates the losses given by V_I but still gives EXAFS amplitudes much smaller then those observed experimentally. The Beni, Lee and Platzman polarisation potential therefore greatly overestimates the strength of the imaginary part of the potential.

Setting α and E_f from physical considerations obviously does not lead to physically acceptable results for the imaginary part of the polarisation potential. However the form of the calculation is such that we may fix the Fermi energy and the Slater exchange parameter to obtain V_I's of approximately the correct magnitude, but only if we know what that magnitude should be before hand. This is obviously not an acceptable situation. To improve the calculation of V_I we would therefore have to use some self-consistent procedure for which the real part of the polarisation potential would first have to be calculated.

5.3.2 The Real Part

We can evaluate the real part of the polarisation potential using equation (5.13). This calculation is slightly more complex than the corresponding computation of the imaginary part of the potential. We have to be careful when performing the k_n integral because of the logarithmic divergence in the integrand, also, we cannot integrate with respect to q or k_n over the full range of the integration, but must truncate the integral at some point. As the integrand falls off uniformly as both k_n and q become much larger than k_i the integral may be safely truncated once a point has been reached where the magnitude of the integrand is so small that it no longer contributes to equation (5.13). Empirically we find that this point is reached once k_n and q are greater than about $5k_i$. The logarithmic divergence

in the integrand is also easily dealt with. We use the NAG routine D01ALF to perform the k_n integral in the region of the singularity.

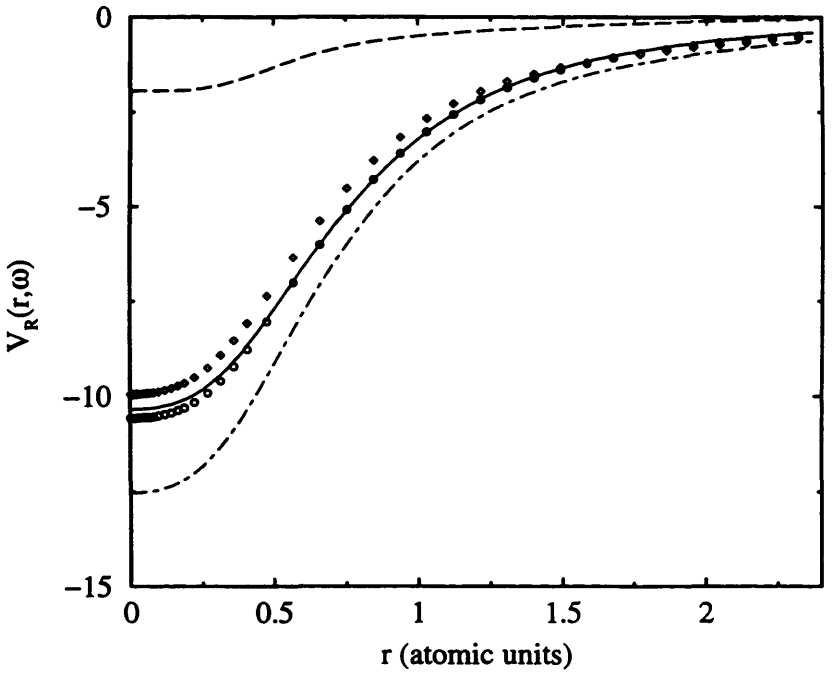

Figure 5.7: The real part of the polarisation potential in Hartrees as a function of r plotted at $k_i = 2$ atomic units for a range of values of the Slater exchange parameter, $\alpha = 0$ (solid curve), $\alpha = 0.25$ (circles), $\alpha = 0.5$ (dot-dash line), $\alpha = 0.75$ (diamonds) and $\alpha = 1.0$ (dashed line).

In figure 5.7 we plot the calculated real part of the polarisation potential against r for a range of values of α at an incident photoelectron wavevector of 2 atomic units. Again, the calculated potential varies significantly with the Slater exchange parameter and hence with the details of the band structure.

As in the calculation of V_I we set α and E_f to give the correct d-band occupancy. This will give us the best obtainable real part to the polarisation potential without the use of a self consistent calculation.

Figure 5.8 shows $V_R(r, \frac{1}{2}k_i^2)$ at $k_i = 2, 4$ and 6 atomic units. We find that the magnitudes of the real part of the potential are similar to those calculated by

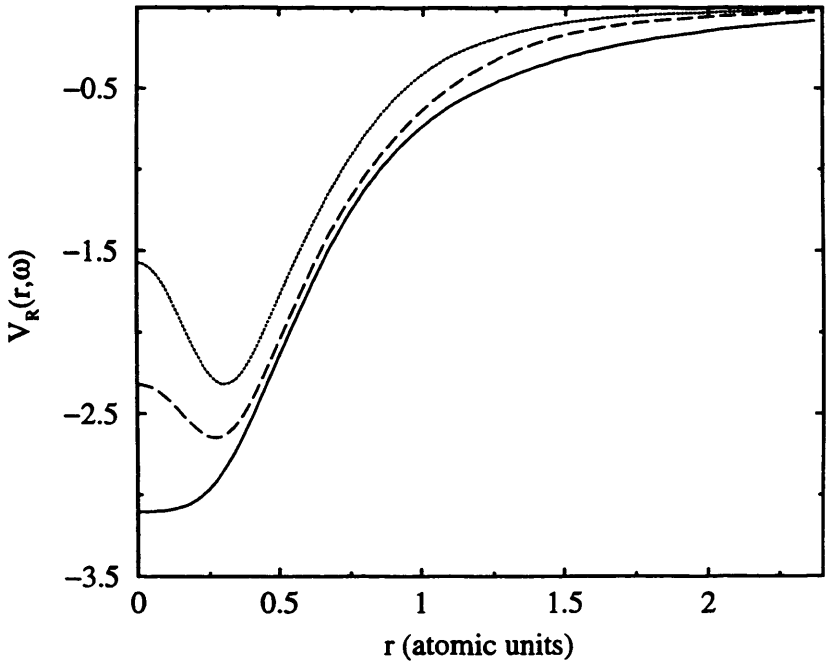

Figure 5.8: The real part of the polarisation potential in Hartrees as a function of r plotted at $k_i = 2$ atomic units (solid curve), $k_i = 4$ (dashed curve) and $k_i = 6$ atomic units (dotted curve), calculated with $\alpha = 0.79$.

Beni, Lee and Platzman. In the left hand graph of figure 5.9 we compare the real part of the HL potential with the sum of the Slater exchange potential and the polarisation potential at $k_i = 2$ and 6 atomic units. We have assumed that the best approximation to the real part of the exchange and correlation potential within the BLP formalism, is given by $V_{XC}(r, \frac{1}{2}k_i^2) = V_{X\alpha}(r) + V_R(r, \frac{1}{2}k_i^2)$. The Hedin-Lundqvist and BLP forms for V_{XC} exhibit similar energy and r dependence. The BLP potential is, however, much stronger, especially close into the nucleus. In figure 5.9 we show the phase-shifts calculated using a muffin tin potential of $V_H(r) + V_{xc}(r, \frac{1}{2}k_i^2)$ (where V_H is the Hartree potential). These exhibit similar behaviour to those calculated using $V_H(r) + V_{X\alpha}(r)$ because, as we can see from figure 5.8 the energy-dependent polarisation potential is merely a small correction

to the Slater exchange.

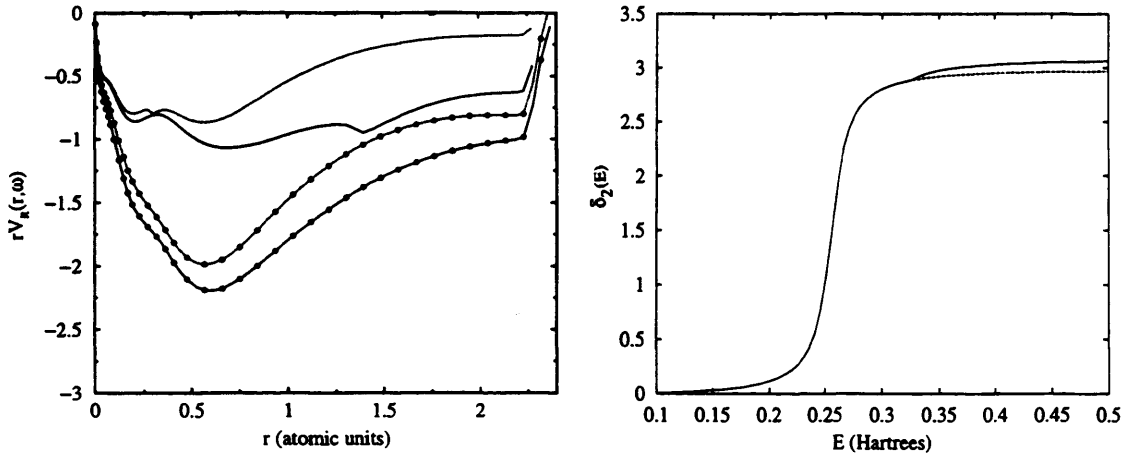

Figure 5.9: The graph on the left shows a comparison between the real part of the HL potential (lines) and the sum of the Slater exchange potential and the real part of the BLP polarisation (lines with circles) potential. $rV(r)$ in atomic units is plotted against r in atomic units at $k_i = 2$ (solid line and solid line with circles) and $k_i = 6$ (dotted line and dotted line with circles). The graph on the right shows the $l = 2$ phase-shift calculated as a function of photoelectron energy using a muffin tin potential of $V_{XC} = V_{X\alpha}(r) + V_R(r, \frac{1}{2}k_i^2)$ (solid line) and $V_{XC} = V_{X\alpha}$ (dashed line).

5.3.3 A Self-Consistent Calculation

In theory it should now be possible to calculate the real part of the polarisation potential self-consistently. We can add the calculated V_R's to the sum of the Hartree and Slater exchange potentials to create a new muffin tin potential. This is then used to calculate a new set of phase-shifts which in turn can be used to evaluate a new set of polarisation potentials. The procedure is then continued until the calculated potential has converged. This calculation, however, becomes progressively more difficult for each iteration. To calculate the polarisation potential at $k_i = 2$ atomic units after one iteration we must first calculate the zeroth order BLP potential up to a photoelectron energy of $k_i = 10$ atomic units.

To calculate the same potential after two iterations we would need to calculate the zeroth order $V_R(r, \frac{1}{2}k_i^2)$ up to $k_i = 50$ atomic units (an energy of ~ 1400 eV) and the 1st order potential up to $k_i = 10$ etc. At such high energies the calculation of the numerical final states becomes problematical. The calculations are also too time consuming to be of practical use in EXAFS data analysis problems as the calculation of the real part of the polarisation potential at a single initial photoelectron energy takes about two and a half minutes. However, as $V_R(r, \frac{1}{2}k_i^2)$ is small compared to $V_H + V_{X\alpha}$ we shall attempt to use the zeroth order results for V_R to calculate new results for the imaginary part of the potential.

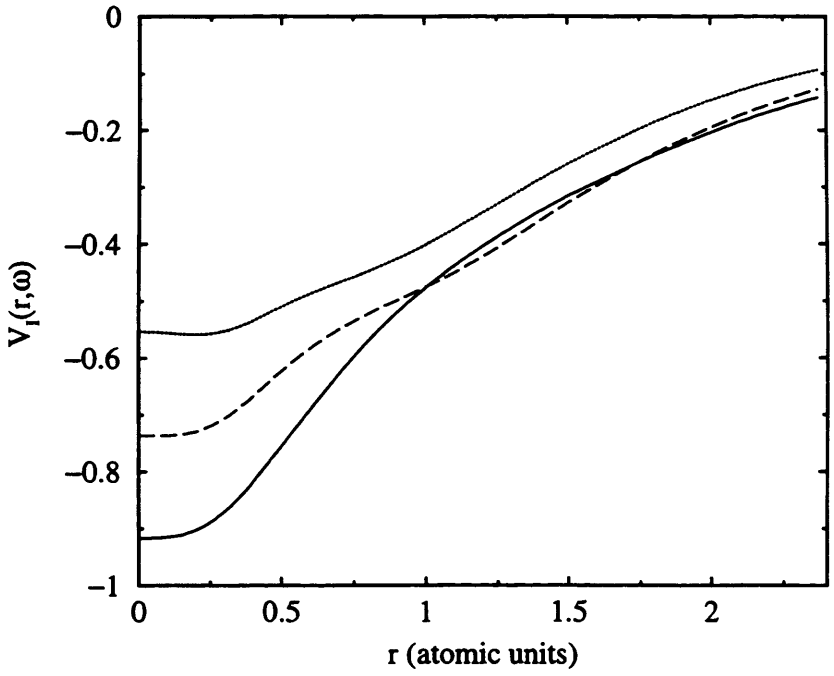

Figure 5.10: First order calculation of the imaginary part of the polarisation potential in Hartrees plotted as a function of r at $k_i = 2$ (solid line), $k_i = 4$ (dashed line) and $k_i = 6$ (dotted line) atomic units.

To obtain the correct band structure using a muffin tin potential of $V_H(r) + V_{X\alpha}(r) + V_R(r, \frac{1}{2}k_i^2)$ we must set $\alpha = 0.79$ and $E_f = 0.272$ Hartrees (7.4eV).

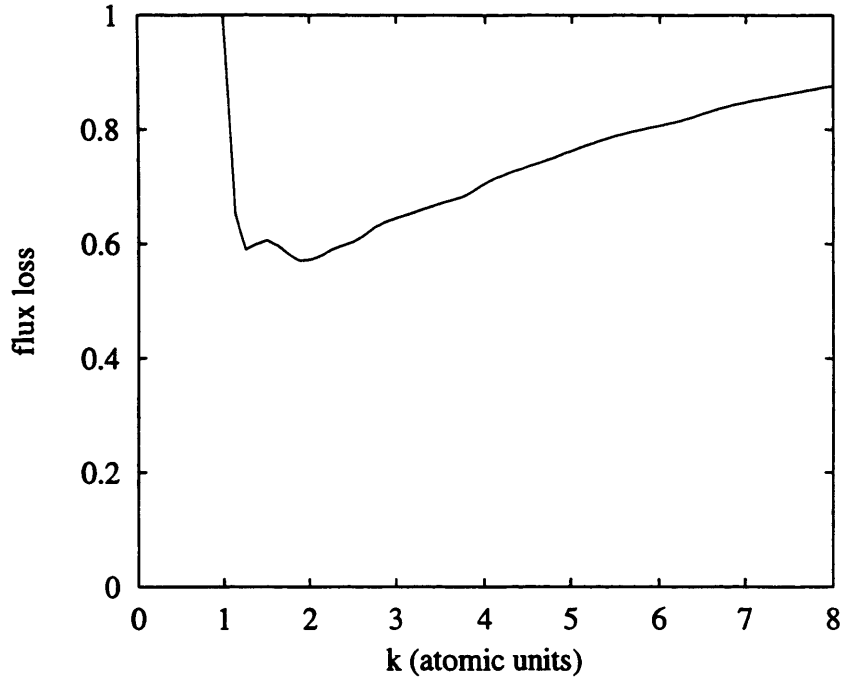

Figure 5.11: The magnitude of the photoelectron flux as the photoelectron propagates through an isolated muffin tin as a function of incident wavevector in atomic units. The flux is calculated from the imaginary part of the polarisation potential using the 2nd order result (eqn. (2.37)).

Figure 5.10 shows $V_I(r, \frac{1}{2}k_i^2)$ at $k_i = 2, 4$ and 6 atomic units. The magnitudes of V_I are smaller than were found previously but are still much larger than the corresponding values of the Hedin-Lundqvist potential. In figure 5.11 we plot the flux of a photoelectron wave scattered by an isolated muffin tin potential against the incident photoelectron energy. The flux is again smaller than we would expect physically and would lead to EXAFS amplitudes much smaller than those observed experimentally. It is possible that higher iterations of the self-consistent calculation of the BLP potential would lead to better results for V_I, however, because of the limitations of the computer program we were not able to test this.

5.4 Conclusion

In this chapter we have investigated the BLP form of the polarisation potential. By developing the potential via the GW approximation we were able to show that the potential does not account for exchange effects but merely approximates the electron-electron correlation. Intuitively we would expect the potential to describe the inelastic scattering of localised states like the copper d bands more accurately than the Hedin-Lundqvist potential because it explicitly includes one electron excitations. However, this was not found to be the case.

In calculating the complex, energy-dependent potential we were able to avoid many of the simplifying approximations originally used by Beni, Lee and Platzman. We discovered that the results for the imaginary part of the potential are extremely dependent on the values used for the Slater exchange parameter, α, and the Fermi energy. This is because the possibility of secondary electron excitations is greatly affected by the number of d-band states in the continuum. We found that setting α and E_f to give the best approximation to the band structure did not lead to physically acceptable results for $V_I(r, \frac{1}{2}k_i^2)$. The BLP form for the polarisation potential greatly overestimates the strength of the inelastic scattering and hence significantly underestimates the EXAFS amplitudes.

The real part of the polarisation potential was also calculated. $V_R(r, \frac{1}{2}k_i^2)$ was discovered to be small in comparison to the Slater exchange potential and gave only a small correction to the phase-shifts. A fully self-consistent calculation of the real part of the BLP potential was found to be computationally infeasible but the zeroth order V_R's were used to recalculate the results for V_I. The first order imaginary potentials were found to be physically more acceptable than the previous results but still lead to EXAFS amplitudes much smaller than observed

experimentally.

In conclusion we find that the BLP form for the polarisation potential is completely unsuitable for EXAFS calculations. It is possible to fix the variable parameters, α and E_f to give an imaginary part to the potential of the required magnitude but only by using a prior knowledge of that magnitude. Setting α and E_f using physical constraints does not lead to acceptable values of V_I and, whilst a self-consistent calculation of V_I would appear to lead to better results it is far too time consuming to be of any practical use in EXAFS calculations. The BLP potential therefore does not give a good description of the extrinsic inelastic scattering of the EXAFS photoelectron.

Chapter 6

The Core hole - Photoelectron System in the Sudden Approximation

In this chapter we calculate the amplitude reduction factor of equation (1.3), and hence the probability of secondary electron excitation, following a photoabsorption event. We examine the limit of high photoelectron energy, the so called sudden limit [18], where the time-dependent, core hole - photoelectron system is greatly simplified. In this limit the photoelectron leaves the atom instantaneously and the passive electrons in the atom (those not interacting with the X-ray photon) experience a sudden change in potential corresponding to the appearance of the core hole. This change in potential may be modelled very simply using Slater's rules [19]. In this fashion it is a simple matter to evaluate the secondary excitation probabilities, and hence s_o^2, for all edges of all elements. The values of the amplitude reduction factor obtained are compared to experiment. We also calculate the probability of exciting any secondary electron into a bound or continuum state following the photoabsorption. The continuum excitation probabilities will be needed in the following chapter. The calculation of the amplitude reduction factor is repeated using tight binding, rather than atomic, initial states. In this way we can determine the chemical dependence of the amplitude reduction factor, s_o^2.

The probability of secondary electron excitation has been studied extensively within the sudden approximation. However, not to our knowledge, for all elements from an EXAFS perspective. Shake-off intensities have been calculated in the sudden limit by, for example, Aberg [57], Carlson [11, 58] and Dyall [59] using wavefunctions varying in complexity from single electron states to multi-configuration Hartree Fock states. Carlson [11] examines the shake probabilities for 15 elements across the periodic table following Beta decay in which the nuclear charge is suddenly increased by one. This has been suggested as an approximation for the core hole created during EXAFS, however it is a crude one. Electrons in the same shell or in orbitals inside the photoelectron initial state will obviously see much less of an effect from the photoionisation than electrons in more weakly bound shells. Using Slaters recipe we can model the effect of the core hole following a photoionisation from any edge more accurately than with the Beta decay Z+1 approximation. In the sudden approximation the shake probabilities are given by the monopole matrix elements between the passive electron eigenstates in the presence and the absence of the core hole. Most of the computational effort in the studies mentioned goes into solving for the perturbed passive electron eigenstates (the initial states are well tabulated). By applying Slater's rules to model the effect of the core hole, however, the calculation of the relaxed atomic orbitals becomes trivial.

6.1 The Amplitude Reduction Factor

Standard, one electron, EXAFS theory (see for example equation (1.3)) includes an amplitude reduction factor, $s_o^2(\omega)$, that allows for processes that contribute to the X-ray absorption coefficient, $\mu(\omega)$, but not to the EXAFS. The need for this factor is ascribed to the possibility of multiple electron excitations at the

absorbing atom. $s_o^2(\omega)$ is almost always treated as a free parameter to be fixed by reference to a standard sample [60], and is an important factor in the experimental determination of coordination numbers. In this process it is implicitly assumed that its value is independent of the chemical environment of the absorbing atom. To calculate s_o^2 theoretically we need to move beyond a strictly one electron theory and consider the behaviour, not only of the photoelectron, but also of the other, passive, electrons in the absorbing atom.

When an atom absorbs an X-ray photon, a photoelectron and a hole in a deep core state are produced. The core hole - photoelectron system corresponds to a time-dependent change in potential which is, in general, extremely complex. To simplify matters we invoke the sudden approximation in which the photoelectron leaves the atom immediately and the passive electrons relax instantaneously. Within this approximation the passive electrons experience an abrupt change in Hamiltonian, thus there is a possibility that they too may be excited into the continuum giving rise to a multiple electron excitation.

As in section 1.3.1 we argue that multiple electron excitations, whilst obviously contributing to the X-ray absorption coefficient, do not in general contribute to the EXAFS. When two, or more, electrons are excited into the continuum the possible range of energies of each is continuous, subject only to the overall energy conservation. Photoelectrons with a host of different energies and hence wavevectors are produced and any interference effects tend to cancel out. Thus, the only case which contributes to the EXAFS is the one in which none of the passive electrons are excited. As the multiple electron excitation events contribute to the total absorption coefficient, but not to the fine structure then, from equation (1.1), the net result is a diminution in the EXAFS amplitude.

Transitions into unoccupied bound states, so called shake up events are also possible. As we discussed in section 1.3.1 these processes will contribute to the

EXAFS but, as we shall see later in this chapter (sec. 6.3.2) are much less probable than the transitions into the continuum and are therefore neglected.

6.2 The EXAFS Function

The EXAFS spectrum is defined in equation (1.1) in terms of the X-ray absorption coefficient, $\mu(\omega)$, by subtracting a smoothly varying background from the total absorption and dividing by the average absorption at each energy. Conventionally EXAFS is treated using a strictly one electron formalism. As in chapter 1 we can use Fermi's golden rule to examine the contributions to the absorption coefficient for any given absorption edge,

$$\mu_{se}(\omega) \sim \sum_k |(1+Z_l)\langle\psi_k|\epsilon\cdot\mathbf{r}|\phi_o\rangle|^2\delta(\omega-|\omega_o|-\omega_k), \tag{6.1}$$

where the function Z_l accounts for the backscattering from nearest neighbours and contains the fine structure. This is defined in equation (2.49). Z_l takes on a different value for each of the two angular momentum final states which may contribute to the matrix element above. The possible final states, $\psi_k(\mathbf{r})$, are degenerate with energy $\omega_k = \omega - |\omega_o|$, $\phi_o(\mathbf{r})$ is the initial one-electron eigenstate of the photoelectron at energy ω_o and $(\epsilon\cdot\mathbf{r})$ is the dipole operator. The smooth background to which the EXAFS is normalised corresponds physically to the absorption due to an isolated atom. This exhibits no fine structure and therefore can be written as in equation (6.1) but without the fine structure term, Z_l. Then, using the result that $\langle\psi_k|\epsilon\cdot\mathbf{r}|\phi_o\rangle$ is real, we can see from equation (1.1) that the EXAFS function in a single electron theory is given by $\chi_{se} = 2Re(Z_l)$, to first order in Z_l.

To calculate the amplitude reduction factor we must include many-body processes. If we define the exact N electron initial and final state wavefunctions

as Φ_o^N and Ψ_n^N, we can write the many-body absorption coefficient as,

$$\mu(\omega) \sim \sum_n |\langle \Phi_o^N | \sum_j \epsilon \cdot \mathbf{r}_j | \Psi_n^N \rangle|^2 \delta(\omega - |E_o| - E_n), \tag{6.2}$$

where the dipole operator includes all electrons, the sum is over all possible final states and E_o and E_n refer to the many-electron system energies. We now assume that the wavefunction may be factored into a Hartree product of single electron wavefunctions, an approximation that is more accurate at high photoelectron energies where the exchange between the photoelectron and the other electrons may be neglected. Using the Hartree form, we can immediately separate out the contribution of any given edge. If we also invoke the sudden approximation the initial and final states will become N electron eigenfunctions of different atomic potentials. Then, considering, for example, the K-edge we write,

$$\mu_{mb}(\omega) = \sum_n |\langle \psi_n | \epsilon \cdot \mathbf{r} | \phi_c \rangle|^2 |\langle \Phi_o^{N-1} | \Psi_n'^{N-1} \rangle|^2 \delta(\omega - |E_o| - E_n), \tag{6.3}$$

where a dash denotes that the eigenfunction is of the perturbed atomic potential, the states Φ_o^{N-1} and $\Psi_n'^{N-1}$ are products of the N-1 passive electron wavefunctions, ϕ_c is the 1s orbital and ψ_n describes the excited photoelectron.

As we only obtain contributions to the fine structure when none of the passive electrons are excited, the total absorption can be considered to be made up of two parts, a part which contributes to the fine structure, where only the photoelectron is excited, and a second part where one or more of the passive electrons are excited in addition to the photoelectron. The second part does not add to the EXAFS. The only final state which contributes to the fine structure is therefore,

$$\Psi_n'^{N-1} = \Phi_o'^{N-1} = \prod_i^{N-1} \phi_i'(\mathbf{r}_i), \tag{6.4}$$

where $\Phi_o'^{N-1}$ is the equivalent initial state under the perturbed atomic potential, $\phi_i(\mathbf{r})'$ are perturbed single electron eigenfunctions and the product is over all

$N-1$ passive electrons. We can separate this term out from the sum over final states in equation (6.3) to give,

$$\begin{aligned}\mu_{mb}(\omega) &= \sum_k |(1+Z)\langle\psi_k|\epsilon\cdot\mathbf{r}|\phi_c\rangle|^2|\langle\Phi_o^{N-1}|\Phi_o'^{N-1}\rangle|^2\delta(\omega-|\omega_c|-\omega_k) \\ &\quad + \sum_n |\langle\psi_n|\epsilon\cdot\mathbf{r}|\phi_o\rangle|^2|\langle\Phi_o^{N-1}|\Psi_n'^{N-1}\rangle|^2\delta(\omega-|E_o|-E_n) \\ &= 2Re(Z)\mu_o(\omega)|\langle\Phi_o^{N-1}|\Phi_o'^{N-1}\rangle|^2 \\ &\quad + \sum_n |\langle\psi_n|\epsilon\cdot\mathbf{r}|\phi_o\rangle|^2|\langle\Phi_o^{N-1}|\Psi_n'^{N-1}\rangle|^2\delta(\omega-|E_o|-E_n), \qquad (6.5)\end{aligned}$$

where, for the K-edge, we only obtain a contribution from one of the l dependent Z terms. The 1st term on the left hand side of equation (6.5) is the only one that contains any oscillatory structure, this is the contribution to the many-body absorption coefficient from excitations involving only one electron. The 2nd term in the equation above is related to the X-ray absorption coefficient,

$$\sum_n |\psi_n|\epsilon\cdot\mathbf{r}\phi_c\rangle|^2|\langle\Phi_o^{N-1}|\Psi_n'^{N-1}\rangle|^2\delta(\omega-|E_o|-E_n) = \sum_n |\langle\Phi_o^{N-1}|\Psi_n'^{N-1}\rangle|^2\mu(\omega-\Delta E_n), \qquad (6.6)$$

where ΔE_n is the difference in energy between the initial and final N-1 electron states. For the sudden approximation to be valid ω must be large. Also, the majority of the contribution to the matrix element, $\langle\Phi_o^{N-1}|\Psi_n'^{N-1}\rangle$, comes from low energy secondary electron final states. Experimentally this can be seen from primary photoelectron energy spectra where most of the photoelectrons leave the atom with an energy not far removed from $\omega_k = \omega - |\omega_c|$ (see, for example figure 7.10). We therefore take $\omega >> \Delta E_n$ so that $\mu(\omega - (\Delta E)_n) \approx \mu(\omega)$. Then, in equation (6.6) we may use the completeness relation, $\sum_n |\langle\Phi_o^{N-1}|\Psi_n'^{N-1}\rangle|^2 = 1$, so that equation (6.5) becomes,

$$\mu_{mb}(\omega) = 2Re(Z)|\langle\Phi_o^{N-1}|\Phi_o'^{N-1}\rangle|^2\mu_o(\omega) + \mu_o(\omega). \qquad (6.7)$$

We have found that the contribution of the fine structure to the many-body absorption coefficient is less than that in the one electron theory. Thus, because

of the normalisation to the average absorption at each energy, the many-body EXAFS function will be reduced.

Following the usual definition of the normalised EXAFS function we find,

$$\begin{aligned} \chi_{mb} &= |\langle \Phi_o^{N-1} | \Phi_o'^{N-1} \rangle|^2 \, 2\, Re(Z_l), \\ &= s_o^2 \chi_{se}, \end{aligned} \tag{6.8}$$

where,

$$s_o^2 = |\langle \Phi_o^{N-1} | \Phi_o'^{N-1} \rangle|^2 = \prod_i^{N-1} |\langle \phi_i(r) | \phi_i(r)' \rangle|^2. \tag{6.9}$$

In this theory the amplitude reduction factor, s_o^2, is simply the product of the square of the overlap integrals between equivalent one electron functions before and after the perturbation in the atomic potential. This is the probability that none of the passive electrons are excited. Result (6.9) was first stated by Rehr *et al* [61].

6.3 Results

6.3.1 Free Atom Calculation of s_o^2

Within the sudden approximation equation (6.9) is a general form for the amplitude reduction factor. In this section we shall, however, specialise, and calculate s_o^2 for free atoms. If we choose the single electron functions, $\phi_i(\mathbf{r})$, to be Slater orbitals [19] we find that the calculation of s_o^2 as a function of Z becomes trivial. The ith orbital of an electron in an element of particular atomic number Z is considered by Slater [19] to be of the form,

$$X_i(\mathbf{r}) = A_i r^{n_i - 1} e^{-\alpha_i r} Y_{lm}(\hat{r}), \tag{6.10}$$

where n_i, l, and m are the principal, angular, and magnetic quantum numbers respectively, $Y_{lm}(\hat{r})$ is a spherical harmonic and A_i is the normalisation constant.

The effective nuclear charge is given by $\alpha_i = \frac{Z_A - \sigma_i}{n_i}$, where σ_i is a screening constant to be determined using Slater's rules [19] and Z_A is the atomic number.

We orthogonalise the Slater functions using the Gram-Schmidt process, so that,

$$\phi_i(\mathbf{r}) = \sum_{u=1}^{n_i} c_u X_u(\mathbf{r}). \tag{6.11}$$

The c_j coefficients are determined via a recurrence relation that ensures that each higher atomic orbital is correctly orthogonalised to the one directly below it.

Using the orthogonalised Slater orbitals the radial integral in equation (6.9) is easily performed. For these monopole transitions the angular integrals are simply the orthogonality relations for the spherical harmonics and the radial integrals may be performed analytically to give,

$$\begin{aligned} s_o^2 &= \prod_i \left[\sum_{u=1}^{n_i} \sum_{v=1}^{n_i} c_u c'_v \langle X_u | X'_v \rangle \right]^{2m_i} \\ &= \prod_i \left[\sum_{u=1}^{n_i} \sum_{v=1}^{n_i} c_u c'_v \frac{(2\alpha_j)^{u+\frac{1}{2}} (2\alpha'_v)^{v+\frac{1}{2}}}{(\alpha_u + \alpha'_v)^{u+v+1}} \right]^{2m_i}, \end{aligned} \tag{6.12}$$

where m_i is the number of electrons in the i orbital and i now runs over different orbitals rather than electrons. α'_i is the effective nuclear charge of the state ϕ'_i following the photoionisation. Slater's rules describe how the effective nuclear charge is perturbed by the appearance of the core hole, giving different values for the change in screening constant depending on whether the photoelectron initial state is inside or outside the ϕ_i orbital. Using Slater's recipe to generate values of the initial state and final state effective nuclear charge we may use equation (6.12) to calculate the amplitude reduction factor for all Z_A.

We obtain reasonable agreement with experiment for low atomic number but find increasing discrepancies at higher Z_A. From figure 6.1 it is clear that the calculated values of s_o^2 are unsatisfactory for elements with unfilled d or f shells. We can, however, greatly improve the accuracy of this simple form for the wavefunctions, and hence the results, by using numerical values for α_i

derived by fitting the Slater form to full SCF Roothaan-Hartree-Fock calculations. Clementi *et al* [26] have tabulated values of the effective nuclear charge from Z=2 to 54. Following Clementi we denote wavefunctions of the Slater form with the tabulated, numerical, values of α_i as single Zeta functions. For atomic numbers greater than $Z_A = 54$ we have generated our own single Zeta functions by fitting orbitals of the Slater form to the tabulated initial states of McLean *et al* [27] using the NAG routine E04BBF. The numerical values of α_i are an improvement over those given by Slater's rules. We have, in effect, refined the calculation of the screening coefficient of the initial state, σ_i. We must, however, still use Slater's rules to model the effect of the core hole on the numerical values of the initial state effective nuclear charge. We also orthogonalise the single Zeta functions using the Gram-Schmidt process.

Using orthogonalised single Zeta functions as the appropriate single electron functions, we find that the calculated values of s_o^2 agree well with the fitted values for the amplitude reduction factor found using the data analysis program EXCURV98 [14] with the $X\alpha$ potential option (figure 6.1). The best fit points have been collated from data taken by Gurman *et al* [52] and Van Dorssen *et al* [62].

The calculated amplitude reduction factor has a characteristic dependence on atomic number and lies between 0.65 and 0.80 for all edges of use in EXAFS. The values are largely independent of the edge, especially for large Z, as is found experimentally.

We can use the R-factor defined in equation (4.19) to provide some measure of the correlation between the calculations and the experimental results. We obtain an R factor of 7.8% between the best fit values and the K-edge amplitude reduction factor calculated using orthogonalised single Zeta wavefunctions. This is less than the errors in the fitted values.

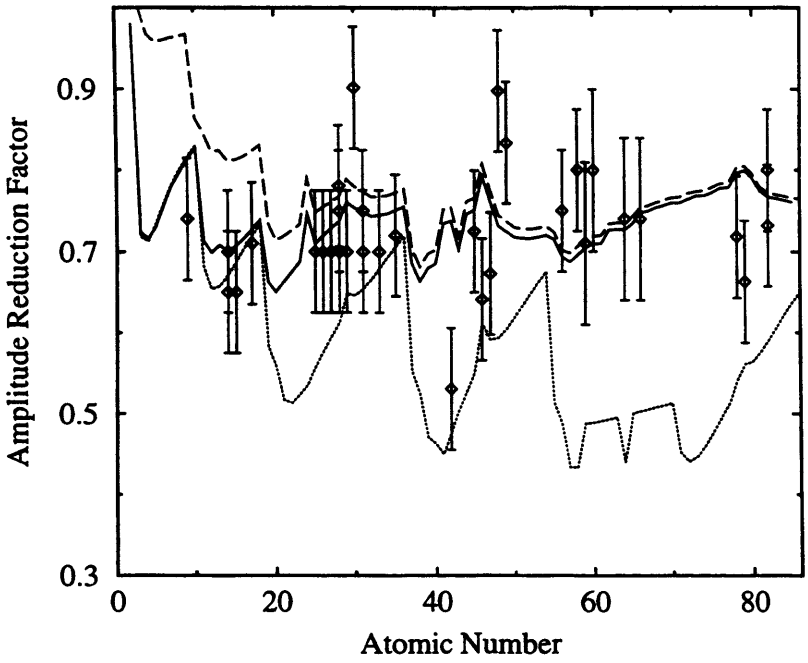

Figure 6.1: The amplitude reduction factor as a function of atomic number. The solid line and dashed line give the magnitudes for the K and L edges respectively, calculated using the single Zeta functions whilst the dotted line records the K-edge values for s_o^2 calculated using Slater orbitals. The points with error bars are values found from experimental data.

6.3.2 Shake Probabilities

We can use the method described above to examine the individual excitation probabilities for each orbital. The probability that each electron stays in the same state after the perturbation to the potential is given by the overlap integral $\left[\langle\phi_i|\phi_i'\rangle\right]^2$, thus the total shake probability per orbital is,

$$P_{suso} = 1 - \left[\langle\phi_i(r)|\phi_i(r)'\rangle\right]^{2m_i}. \tag{6.13}$$

From figure 6.2 we can see that the greatest excitation probabilities and hence the largest contributions to the amplitude reduction come from the outermost atomic orbitals. As we expect it is the weakly bound electrons that are most likely to be excited by the perturbation in the potential caused by the photoionisation.

Ignoring the small probability of shake-up into a bound excited state the results in figure 6.2 may be taken as the high energy limit for the probability of secondary electron excitation into the continuum. These probabilities per atomic orbital and for each edge of all elements will be used in the following chapter.

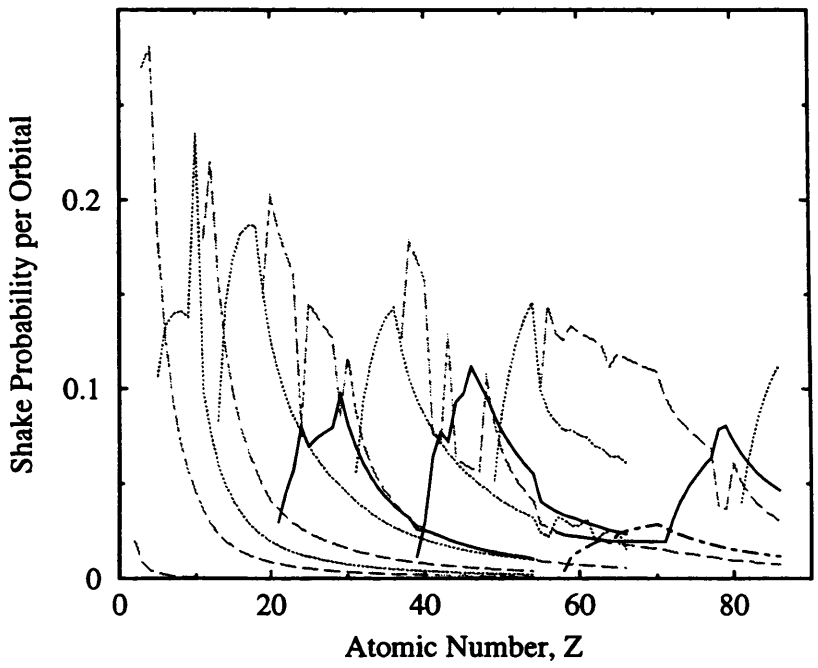

Figure 6.2: Total excitation probability per orbital. Wide spaced dashed lines denote s-orbitals, n=2 to 6 from left to right. Dotted lines are the p-orbitals with n=2 to 6 from left to right. The total excitation probability of the d-orbitals are given by the solid lines (n=3 to 5 from left to right) and the 4f excitation probabilities are recorded by the dot-dashed line.

We can also obtain an estimate of the magnitude of the bound to bound transitions using the sudden approximation. The probability of a secondary electron transition from an initial state, ϕ_i, into a bound excited state, ϕ_{n_f}, under the sudden approximation is proportional to the square of the matrix element, $\langle \phi_i | \phi'_{n_f} \rangle$. Using Slater's rules and equation (6.11) we may generate orthogonalised bound excited states in the presence of the core hole from the single Zeta basis functions. These will be of the form of equation (6.10) with an effective nuclear

charge of $1/n_f$, where n_f is the final state principal quantum number. In figure 6.3 we plot the probability of a transition into a bound occupied state following a K-edge photoexcitation in Copper as a function of n_f. The diamonds show the probability of an excitation from the 4s orbital into a higher unoccupied s-state whilst the circles show the probability of exciting a 3d electron into a higher unoccupied d-state. The probabilities are per electron. The Shake-up probabilities are greater for the more weakly bound states, they also fall off with increasing final state quantum number. The calculated shake-up probabilities are, as we have assumed, negligible compared to the shake-off probabilities. For a Copper 4s electron, for example, we find the total probability of a transition into a bound state to be 0.03% compared to the probability of a transition into the continuum of 8.69%.

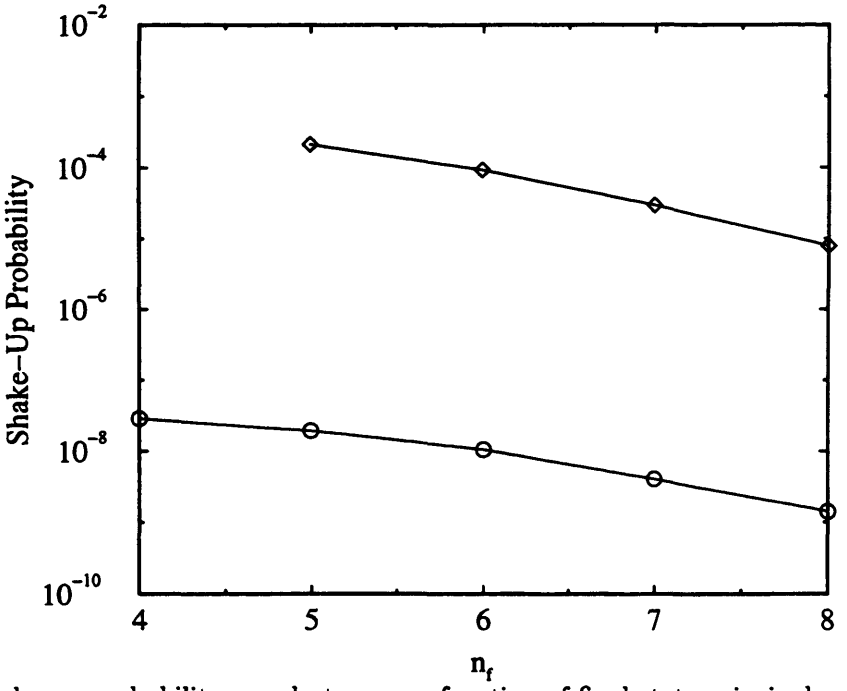

Figure 6.3: Shake up probability per electron as a function of final state principal quantum number following a K-edge photoabsorption in copper. The diamonds give the transition probabilities for an electron initially in the 4s state, the circles, for an electron initially in the 3d state.

6.4 The Chemical Dependence of s_o^2

6.4.1 Tight Binding Method

In the analysis of EXAFS data it is usually assumed that the amplitude reduction is independent of the chemical environment of the absorbing atom. To investigate the accuracy of this assumption we calculate s_o^2 for the solid state using the tight binding approximation. We take the initial state, single electron, wavefunctions to be a Bloch sum of atomic orbitals,

$$|\varphi_{i\mathbf{k}}(\mathbf{r})\rangle = A_i \sum_{\mathbf{R}} e^{i\mathbf{k}\cdot\mathbf{R}} |\phi_i(\mathbf{r}-\mathbf{R})\rangle, \tag{6.14}$$

where the sum over $\mathbf{R}$ runs over all lattice sites, and $\phi_i(\mathbf{r})$ are orthogonalised atomic orbitals constructed from basis functions of the form of equation (6.11). The normalisation constant, A_i, is given by the expression

$$\frac{1}{|A_i|^2} = N\left(1 + \sum_{\mathbf{R}} e^{i\mathbf{k}\cdot\mathbf{R}} \langle\phi_i(\mathbf{r})|\phi_i(\mathbf{r}-\mathbf{R})\rangle\right), \tag{6.15}$$

in which N is the number of atoms in the sample and comes from summing the terms over N identical lattice sites. We have assumed that the overlaps between atomic orbitals fall off rapidly with distance. The overlaps will be negligible except when $\mathbf{R}' = \mathbf{R}$ or when $\mathbf{R}'$ refers to one of the nearest neighbours of the atom at $\mathbf{R}$. The summation above is therefore restricted to nearest neighbours only.

After a photoionisation event one of the atoms in the lattice will contain a core hole. We assume this absorbing atom to be at the origin, then the perturbed wavefunction becomes,

$$|\varphi'_{i\mathbf{k}}(\mathbf{r})\rangle = A'_i\left(\sum_{\mathbf{R}} e^{i\mathbf{k}\cdot\mathbf{R}} |\phi_i(\mathbf{r}-\mathbf{R})\rangle + |\phi'_i(\mathbf{r})\rangle - |\phi_i(\mathbf{r})\rangle\right). \tag{6.16}$$

This wavefunction no longer satisfies the Bloch condition because the presence of the core hole on one of the atoms has made the crystal aperiodic. In the equation

above A_i' is given by,

$$\frac{1}{|A_i'|^2} = N\left(1 + s_{ni}^* + \frac{1}{N}\left(s_{ni}^{*\prime} + s_{ni}' - s_{ni} - s_{ni}^*\right)\right), \tag{6.17}$$

where, $s_{ni} = \sum_{\mathbf{R}} e^{i\mathbf{k}\cdot\mathbf{R}}\langle\phi_i(\mathbf{r})|\phi_i(\mathbf{r}-\mathbf{R})\rangle$, $s_{ni}' = \sum_{\mathbf{R}} e^{i\mathbf{k}\cdot\mathbf{R}}\langle\phi_i'(\mathbf{r})|\phi_i(\mathbf{r}-\mathbf{R})\rangle$, and $s_i' = \langle\phi_i(\mathbf{r})|\phi_i'(\mathbf{r})\rangle$. The difference between A_i and A_i' is of order $1/N$ as we would expect. We have one core hole amongst N atoms. Again we have restricted the sums over lattice sites to nearest neighbours only.

To calculate s_o^2 under the sudden approximation we need to find the overlap $|\langle\varphi_{i\mathbf{k}}|\varphi_{i\mathbf{k}}'\rangle|^2$ for each allowed initial state. Then,

$$\begin{aligned} s_o^2 &= \prod_{k,i} |\langle\varphi_{i\mathbf{k}}(\mathbf{r})|\varphi_{i\mathbf{k}}'(\mathbf{r})\rangle|^2 \\ &= N^2 \prod_{k,i} |A_i|^2 |A_i'|^2 \left|1 + s_{ni} + \frac{1}{N}(s_{ni}^{*\prime} - s_{ni}^* + s_i' - 1)\right|^2 . \end{aligned} \tag{6.18}$$

The single electron wavefunctions, $\phi_i(\mathbf{r}-\mathbf{R})$, are constructed from sets of Slater orbitals therefore the overlaps between them must be real. We also note that the sum over nearest neighbours includes both positive and negative nearest neighbour vectors and hence terms like s_{ni} will also be real. We now assume that we may neglect terms of the order of N^{-2}. Then, substituting for $|A_i|^2$ and $|A_i'^2|$ we find,

$$\ln s_o^2 = \sum_{k,i} \ln\left(1 + \frac{2(s_i' - 1)}{N(1 + s_{ni})}\right) \approx \sum_{k,i} \frac{2(s_i' - 1)}{N(1 + s_{ni})}, \tag{6.19}$$

where we have factorised out $(1 + s_n)^{-1}$ from $|A_i'|^2$ and expanded the remaining factor to 1st order in $1/N$. We have also taken the $1/N$ term to be small in order to approximate the logarithm to first order.

The sum over k above may be converted into an integral over occupied states within the Brillouin zone. The integral over the full zone must give $2N$ electrons [63], thus we have,

$$\ln s_o^2 = \sum_i \frac{4(s_i' - 1)}{u(2\pi)^3} \int d\mathbf{k} \frac{1}{(1 + s_{ni})}, \tag{6.20}$$

where we have multiplied by 2 to account for spin degeneracy and changed variable from k to k/a where a is the length of the unit cell in real space. u is the number of atoms in the real space unit cell.

We can examine the behaviour of equation (6.20) in the free atom limit, where the overlaps between nearest neighbours go to zero. In this case we simply have an integral over the occupied states which returns a factor proportional to the number of electrons in the band, $m_i = \frac{2}{(2\pi)^3 u} \int d\mathbf{k}$. In a free atom, this is just the number of electrons in the initial state, ϕ_i. Then, making the approximation that $s_i' - 1$ is small we can see that

$$s_o^2 = \exp\Big(\sum_i 2m_i \ln s_i'\Big) = \prod_i |\langle\phi_i(\mathbf{r})|\phi_i(\mathbf{r})'\rangle|^{2m_i} . \tag{6.21}$$

Thus, in the free atom limit we obtain exactly the same result for the amplitude reduction as in the previous calculation (eqn.(6.9)). Using this result we may rewrite the full tight binding form for s_o^2 in terms of the free atom values and a correction factor. Writing the contribution from each initial state to the free atom amplitude reduction factor as s_{fi}^2 and the overlap integrals between nearest neighbour atoms as $p_{\mathbf{R}} = \langle\phi(\mathbf{r})|\phi(\mathbf{r}+\mathbf{R})\rangle$, we find,

$$\ln s_o^2 = \sum_i \ln s_{fi}^2 + 4(s_i' - 1)\left(\frac{1}{(2\pi)^3 u}\int \frac{d\mathbf{k}}{1 + \sum_{\mathbf{R}} p_{\mathbf{R}} cos(\mathbf{k}\cdot\mathbf{R}/a)} - \frac{1}{2}m_i\right). \tag{6.22}$$

Or, for a single initial state, $s_o^2 = exp\Big[4(s'-1)(C - \frac{1}{2}m_i)\Big]s_f^2$ where C is the integral on the right hand side of the equation above.

Equation (6.22) gives a value for s_o^2 calculated for the solid state using tight binding wavefunctions in terms of the free atom amplitude reduction factor modified by a correction factor. In order to estimate the magnitude of this correction factor we must evaluate the integral over the occupied states within the Brillouin zone. We can calculate this integral numerically for various types of real space lattice using the trapezium rule to perform the integration to an accuracy of within 1%.

The integral over the Brillouin zone is most easily performed in Cartesian coordinates. For body centred cubic, face centred cubic and simple cubic real space lattices the nearest neighbours are distributed symmetrically in the x,y, and z directions. The sum over nearest neighbours of $cos(\mathbf{k} \cdot \mathbf{R})$ is an even function in x,y and z thus, when performing the integrals numerically, we need only consider an eighth of the Brillouin zone. In the tight binding scheme the $E(\mathbf{k})$ dispersion relation depends only on $\sum_{\mathbf{R}} cos(\mathbf{k} \cdot \mathbf{R})$ [64], therefore, this too is an even function in x,y, and z. The integrals are over occupied (k_x, k_y, k_z) states, those for which $E(\mathbf{k})$ is less than the Fermi energy.

To obtain general results for the correction factor $exp\Big[4(s'-1)(C-\frac{1}{2}m_i)\Big]$ we must examine the magnitude of the overlaps between nearest neighbour atomic orbitals, $p_{\mathbf{R}}$. The nearest neighbour tight binding scheme used is only valid if $p_{\mathbf{R}}$ is less than the reciprocal of the number of nearest neighbours. Thus, for each type of real space lattice we may set $p_{\mathbf{R}}$ to just under the reciprocal of the number of nearest neighbours in order to study the case most different from the free atom situation. Thus, for the SC cubic lattice we set $p_{\mathbf{R}} = 0.15$. $p_{\mathbf{R}} = 0.11$ for a BCC lattice and we take $p_{\mathbf{R}} = 0.07$ for an FCC where there are 12 nearest neighbours.

In figure 6.4 we plot the results of the various integrals in equation (6.22). Each integral is over the occupied states within the first Brillouin zone for the particular type of real space lattice shown. The solid line shows the integral, C, integrated over the region where $E(\mathbf{k})$ < Energy. The energy has been scaled so that it goes from 0 to 1 between the edges of the band (see figure 6.6). Unsurprisingly C is zero where the band is empty and reaches its maximum for a full band. The dashed line shows $\frac{1}{2}m_i = \frac{1}{(2\pi)^3 u} \int d\mathbf{k}$, again integrated up to $E(\mathbf{k})$ = Energy. Finally, the long dashed line with circles records $\frac{dm_i}{dE}$, this is the tight binding density of states.

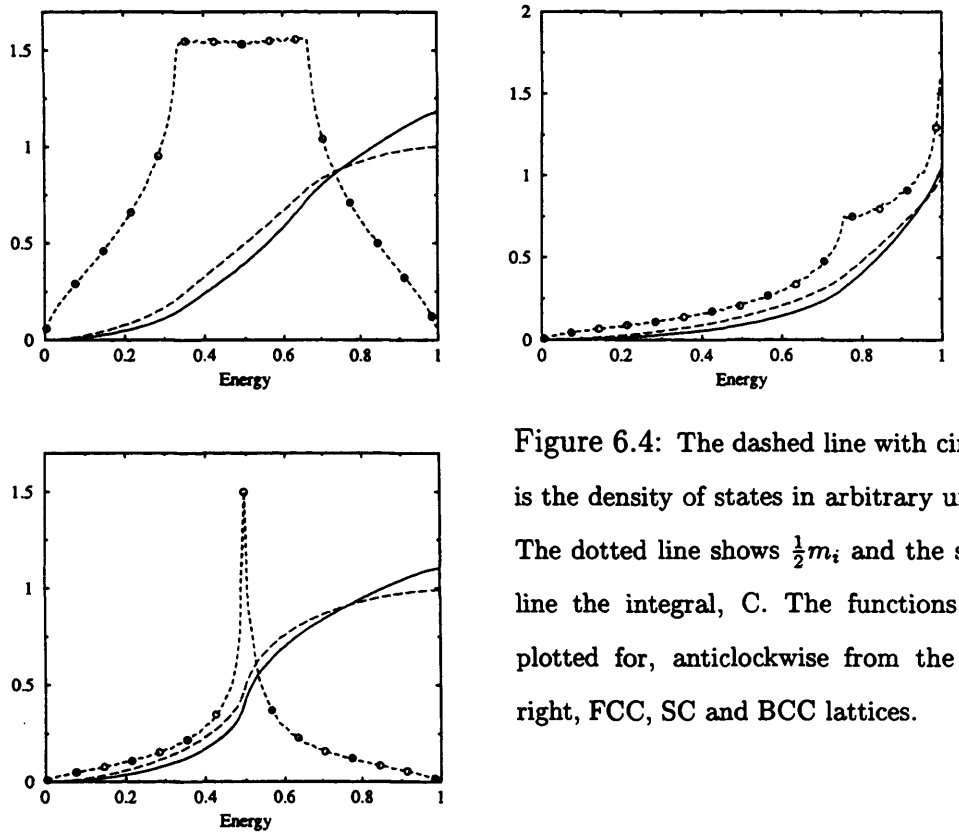

Figure 6.4: The dashed line with circles is the density of states in arbitrary units. The dotted line shows $\frac{1}{2}m_i$ and the solid line the integral, C. The functions are plotted for, anticlockwise from the top right, FCC, SC and BCC lattices.

Figure 6.4 shows results for C where the nearest neighbour overlaps take their maximum allowed values. We can use these results to obtain an estimate for the value of the correction factor, $exp\left[4(s'-1)(C-\frac{1}{2}m_i)\right]$, that differs most from one. We must first, however, specify a value for the overlap integral between perturbed wavefunctions on the absorbing atom site, s'. The values of s' are generally around 0.93 for the most weakly bound states of most elements. The minimum value of s', which will give the maximum correction factor to the free atom amplitude reduction factor, is $s' = 0.821$ for the Sodium 3S initial state. Taking this value for s' we can evaluate the maximum correction factor for each type of real space lattice. This is plotted in figure 6.5.

The correction factor is greater than one where the band is less than half full and less than one where more than a single electron occupies the band. This is reasonable. Figure 6.6 shows a schematic diagram of how a single atomic

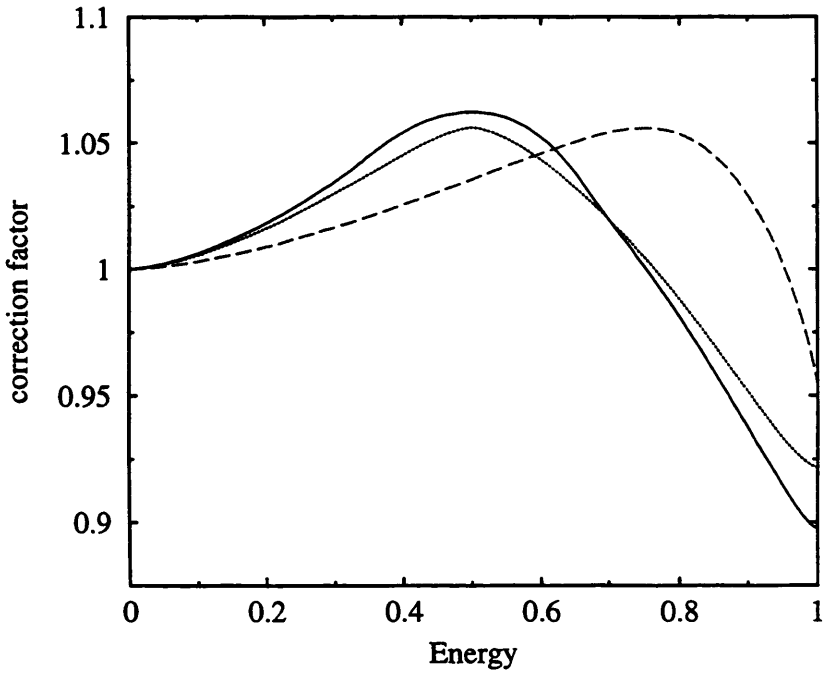

Figure 6.5: The tight binding correction factor to the free atom amplitude reduction factor. The solid line shows the result for an SC lattice, the dashed line for an FCC lattice and the dotted line for a BCC lattice.

energy level broadens to form an energy band as the atoms comprising the solid move closer together. In a band which is less than half full the electrons in the band will be more tightly bound than the electrons in the corresponding atomic state. The electrons will therefore be harder to excite and the tight binding amplitude reduction factor will be closer to one than that in a free atom. Thus, the correction factor must be greater than one. For a full band however, some electrons are in much more weakly bound states than in the free atom. These electrons are consequently much easier to excite, leading to lower values of s_o^2 in the solid and hence a tight binding correction factor of less than one.

In figure 6.5 the tight binding correction to s_o^2 is at most $\sim$ 10%. In reality we would expect the correction to be smaller than this as the perturbed overlap integral, s' is generally larger than 0.821. However, even using the minimum value for s' we obtain minimal differences between the tight binding amplitude

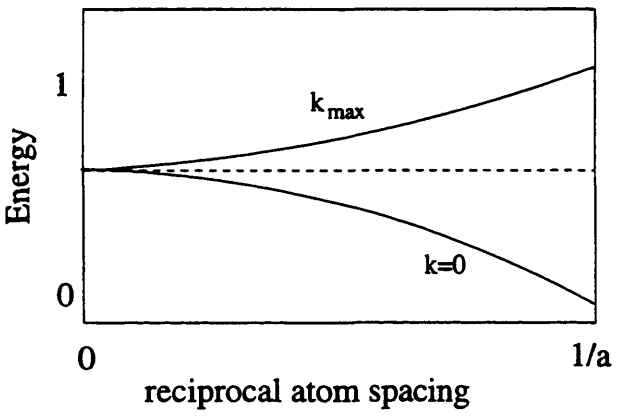

Figure 6.6: Schematic of the broadening of the atomic energy levels to form energy bands as the atoms move closer together in a solid. The dotted line shows the free atom energy state.

reduction factor and the free atom s_o^2. The differences of at most 10% between the two calculations are of the order of the errors encountered in s_o^2 when performing data analysis and may therefore be neglected.

There is effectively no change to the amplitude reduction factor between elements in their atomic states and in condensed matter. In writing the appropriate single electron functions as a Bloch sum we have not assumed that the orbitals on adjacent lattice sites are of the same atom type. Thus the theory deals equally well with compounds in addition to elements. We therefore conclude that the amplitude reduction factor is independent of chemical environment as is generally assumed and depends only on the properties of the atom absorbing the X-ray photon.

6.5 Conclusion

In this chapter we have used the sudden approximation to perform a model calculation of the amplitude reduction factor for all edges of all elements. We take the electronic initial states to be of the Slater [19] form with numerical coefficients for the effective nuclear charges as tabulated by Clementi *et al* [26]. Then, using Slater's rules to model the effect of the core hole we obtain results

which agree extremely well with experiment. Using tight binding wavefunctions to describe the electronic initial states we have also demonstrated that, in the high energy limit, s_o^2 is effectively independent of the chemical environment of the absorbing atom.

In section 6.3.2 we have also produced results for the high energy limit of the shake probabilities for any electron in any atom. We find that the probability of transitions into unoccupied bound states are small, verifying the conclusions of, for example, Hayes and Boyce [13] who state that such transitions may generally be neglected. The values for the calculated shake-off probabilities will be needed in the following chapter.

Chapter 7

A Time-Dependent Model of the Core hole - Photoelectron System

In this chapter we investigate and extend a model proposed by Thomas [20] to explain the energy dependence of shake-up and shake-off processes following core photoionisation.

We treat an event in which a photon is absorbed by an atom producing a photoelectron and a core hole. The core hole - photoelectron system is described using a spatially and temporally varying model potential. This potential is then used to calculate the probability of secondary electron excitation using standard time-dependent perturbation theory; the perturbation being the core hole - photoelectron system. The model proposed is used to calculate the secondary electron shake-off intensity, the ejected electron energy spectrum and the two electron X-ray absorption coefficient. The probability of secondary electron shake-off is, of course, closely related to the amplitude reduction factor used in EXAFS data analysis.

The problem of multiple photoionisation has been extensively studied in the literature. Shake-off intensities have been calculated in the sudden limit by a number of authors (see chapter 6). Zhang et al [65] and Schaphorst et al [66] examine the two electron X-ray absorption coefficients in Xenon and

Krypton respectively. These authors use the sudden approximation and single configuration Hartree Fock wavefunctions. Single configuration wavefunctions cannot, however, adequately describe the effects of electron-electron correlation which are known to be important in multiple electron excitations [67, 20]. More complex calculations which include the effects of the electronic correlation and describe the energy dependence of the shake-off intensities have also been performed. Chang and Poe [68] and Carter and Kelly [69] use many-body perturbation theory (MBPT) to calculate the double electron excitation probabilities with multi-configuration initial and final states. These studies appear to give good agreement with experiment but suffer from a number of disadvantages from the point of view of EXAFS data analysis: The calculations are complex and computationally intensive, the important excited final states have to be put in by hand, and the method is limited to summations over final states so that the continuum must be approximated by a number of discrete excited states. Ideally, for EXAFS purposes, we would like a theory which combines the simplicity of the single electron approach with the description of the energy dependence and the electron-electron correlation given by MBPT. The outlines of such a theory are given by Thomas [20] who treats the coulombic interaction between the photoelectron and the passive electrons explicitly using time-dependent perturbation theory. Along with other workers [70, 71, 72, 73], Thomas approximates the core hole - photoelectron system with a simple model potential.

Thomas [20] uses a time-dependent model potential to describe the transition from the adiabatic to the sudden regime in the shake-up spectra of one of the satellites of N_2 adsorbed on Nickel. Thomas' model reproduced the energy variation of the shake-up probability measured by Stohr, Jaeger and Rehr [74] but could not give the shake-up intensity. This had to be included as an adjustable

parameter taken from experiment. Thomas also claimed good agreement with neon shake-off data produced by Carlson and Krause [58]. However, this analysis of the shake-off data is incorrect. Thomas only considers transitions into one particular excited state, at $47.3eV$ above the neon 2p edge, whereas, for shake-off, the possibility of secondary electron transitions into any of the energetically available continuum states must be taken into account.

In this chapter we first extend Thomas' model to correctly describe shake-off processes and connect it to the results for secondary electron excitation given by the sudden approximation (calculated in chapter 6). In the second part of the chapter we produce a more complex form of the model potential. We introduce some of the exchange and correlation effects included in the MBPT calculations by screening the core hole - photoelectron potential with a model dielectric function. With the screened potential we obtain reasonable results for both the magnitudes and energy variation of the shake-up intensity. We compare our calculated results with a number of experimental studies.

7.1 Theory

In this model we assume that an atom absorbs a photon of frequency ω. The photon excites an electron from a given initial state, ϕ_i, into a continuum state of energy $\omega - |\omega_i|$. Following the photoionisation, the resulting photoelectron and core hole system acts as a perturbation on the other, passive, electrons in the absorbing atom. We approximate this time-dependent perturbation with a model potential and use first order time-dependent perturbation theory to calculate the probability of exciting each of the secondary electrons.

We start from a standard result of time-dependent perturbation theory [18].

The perturbed electronic wavefunctions may be expanded as,

$$\Psi(r,t) = \sum_n a_n(t)\psi_n exp\left(-\imath \int_o^t E_n(t')dt'\right), \tag{7.1}$$

where the expansion coefficients, $a_n(t)$, are written in terms of the time differential of the perturbing potential,

$$\frac{da_n}{dt} = \frac{1}{\omega_{no}}\left\langle \psi_n \left| \frac{dV(r,t)}{dt} \right| \phi_o \right\rangle exp\left(\imath \int_o^t \omega_{no}(t')dt'\right). \tag{7.2}$$

$V(r,t)$ is the potential seen by the passive electrons due to the creation of the photoelectron and the core hole, and $\omega_{no} = \omega_n - \omega_o$ is the difference between the excited and initial state energies of the passive electron in question. $\psi_n(\mathbf{r})$ are the excited states of the system and we have taken the system to be initially in the state $\phi_o(\mathbf{r})$ before the creation of the photoelectron.

Following Thomas, we assume that the energies of the excited states do not vary with time. Then, as we are interested in the expansion coefficients of the excited states a long time after the application of the perturbation, we find,

$$a_n(\infty) = \frac{1}{\omega_{no}}\left\langle \psi_n \left| \int_o^\infty \frac{dV}{dt} exp(\imath\omega_{no}t)dt \right| \phi_o \right\rangle. \tag{7.3}$$

The probability of exciting the passive electron initially in state, ϕ_o, into a particular excited state, ψ_n, is simply the modulus squared of the expansion coefficient,

$$P_{o\to n} = \frac{1}{\omega_{no}^2}\left| \left\langle \psi_n \left| \int_o^\infty \frac{dV}{dt} exp(\imath\omega_{no}t)dt \right| \phi_o \right\rangle \right|^2. \tag{7.4}$$

Thomas [20] completely separates the spatially and temporally varying parts of the potential. In general, both the shape and the magnitude of the core hole - photoelectron potential will vary with time, however, the approximations proposed by Thomas greatly simplify the analysis and lead to reasonable agreement with experiment. We choose our potential to have the form,

$$\begin{aligned} V(r,t) &= V(r)f(t) \\ &= V(r)\left\{1 - exp\left(\frac{-t}{t_o}\right)\right\} \qquad t > 0, \end{aligned} \tag{7.5}$$

where t_o is some measure of the time taken by the photoelectron to leave the atom. This potential has the correct limits at small and large times. At the moment the X-ray photon is absorbed, when the core hole and the photoelectron exist in the same place, the model potential is zero. At large times when the photoelectron has departed from the atom the potential looks like that produced by the core hole alone, $V(r)$. At intermediate times the potential varies smoothly between the two limits.

Thomas assumed the potential varied as an error function in time so that the time differential was Gaussian. We however, use another form of the time dependence proposed by Gadzuk and Sunjic [70]. This is simply for mathematical convenience. The only strictures placed on the time-dependent part of the potential are that it starts at zero, goes to unity at large times, and varies significantly over the time t_o. Both the Thomas and the Gadzuk and Sunjic forms for $f(t)$ satisfy these constraints.

Thomas defines t_o as,

$$t_o = \frac{R_c}{\sqrt{2E_p}}, \tag{7.6}$$

where E_p is the energy of the primary photoelectron and R_c is defined as a distance comparable to atomic dimensions. In this theory the photoelectron is created *before* the secondary electrons. The relevant perturbation is therefore the original photoelectron produced by the absorption of the X-ray photon, thus $E_p = \omega - |\omega_i|$. The velocity of the photoelectron has been assumed to be constant throughout the atom. Thomas varies R_c between $1.5\mathring{A}$ and $3.0\mathring{A}$ when modelling the Nitrogen shake-up data and sets R_c equal to the mean radius of the neon 2p shell when examining the neon shake-off data. We take R_c to be the mean radius of each atomic orbital, arguing that the majority of the interaction between the passive electron and the photoelectron will take place within this radius. We set

R_c from the binding energy of each atomic orbital using the relation for hydrogenic wavefunctions,

$$R_c = \frac{n_o}{\sqrt{2E_o}}, \tag{7.7}$$

where E_o is the binding energy and n_o the principal quantum number of the passive electron initial state in question.

7.1.1 Shake-off Intensities and the Sudden Approximation

We now use equation (7.5) for the perturbing potential to obtain an expression for the energy dependence of the shake-off probabilities. Substituting for $V(r,t)$ into equation (7.4) gives the relevant excitation probability as,

$$\begin{aligned} P_{o\to n} &= \frac{|\langle\psi_n|V(r)|\phi_o\rangle|^2}{\omega_{no}^2}\left|\frac{1}{t_o}\int_o^\infty exp\left\{\left(\omega\omega_{no}-\frac{1}{t_o}\right)t\right\}dt\right|^2 \\ &= \frac{|\langle\psi_n|V|\phi_o\rangle|^2}{\omega_{no}^2}\left(1+\omega_{no}^2t_o^2\right)^{-1}. \end{aligned} \tag{7.8}$$

This is the probability of exciting a particular passive electron into a particular excited state of energy ω_n, and is equivalent to the result used by Thomas to describe the neon data of Carlson with a fixed transition energy of $\omega_{no} = 47.3eV$. However, in reality, the secondary electrons may be excited into a number of different states. Thus, to obtain the total probability of exciting a given passive electron, we must sum over all the energetically available excited states,

$$P_o = \sum_n \frac{|\langle\psi_n|V|\phi_o\rangle|^2}{\omega_{no}^2}\left(1+\omega_{no}^2t_o^2\right)^{-1}. \tag{7.9}$$

We are simply interested in the secondary electron shake-off. We therefore ignore the possibility of bound to bound transitions in equation (7.9) (the shake-up) and concentrate on transitions into propagating states in the continuum. This allows us to rewrite the sum over excited states as an integral over the free electron density of states,

$$P_o = \frac{1}{(2\pi)^3}\int_o^{k_{max}} \frac{|\langle\psi_k|V|\phi_o\rangle|^2}{\omega_{ko}^2}\left(1+\omega_{ko}^2t_o^2\right)^{-1} d\mathbf{k}. \tag{7.10}$$

From energy conservation we find that, $k_{max} = (2.0(E_p - |\omega_o|))^{\frac{1}{2}}$, where E_p is the energy of the primary photoelectron. The continuum wavefunctions are as usual given by equation (2.5) whilst the initial states are taken to be products of radial functions $\phi_{l_o}(r)$ and spherical harmonics $Y_{l_o,m_o}(\hat{r})$.

Taking these forms for the wavefunctions, the angular part of the k integral may be easily done. Also, because $V(r)$ is assumed to be spherically symmetric, only transitions between initial and final states of the same angular momenta are allowed. These monopole transitions are the same as those encountered in chapter 6. In the sudden approximation the transition probabilities were found to depend on the matrix element between the initial and the perturbed final states (eqn.(6.13)). In this calculation the shake-off probabilities depend on the matrix element between initial and unperturbed continuum states modulated by the perturbing potential, $V(r)$.

From equation (7.10) the probability of exciting a secondary electron from a given initial state is,

$$P_o = \frac{1}{2\pi} \int_o^{k_{max}} \frac{k^2 |\langle R_{l_o}(k,r)|V(r)|\phi_{l_o}(r)\rangle|^2}{\omega_{ko}^2(1+\omega_{ko}^2 t_o^2)} dk, \tag{7.11}$$

where $\langle R_{l_o}|V|\phi_{l_o}\rangle$ now represents $\int r^2 R_{l_o} V \phi_{l_o} dr$.

In principle this result can be used to calculate numerical values for the shake-off probability. However the exact form for the hole potential is unknown. We therefore follow the procedure of Thomas and rewrite equation (7.11) as the product of some energy-dependent function normalised to the probability of exciting a secondary electron in the sudden limit. This probability may then be treated as an adjustable parameter to be taken from experiment or from other theoretical calculations.

To connect equation (7.11) to the sudden approximation results we must take the limit as the photoelectron energy goes to infinity. If the primary photoelectron

is extremely energetic the time taken for it to leave the absorbing atom, t_o, will tend to zero whilst k_{max} will go to infinity. In this case we ignore the factor $\omega_{ko}^2 t_o^2$ in the denominator of the above equation. Strictly speaking this is not a valid approximation over the whole of the region of the integration because, whilst t_o tends to zero, ω_{ko} can go to infinity. However, in the regions where k is large the matrix element in equation (7.11) will be insignificant due to the rapid oscillations of the continuum final state. The majority of the contribution to the secondary electron shake-off comes from low energy transitions thus, in the limit of high photoelectron energy, we find,

$$P_o^{\infty} = \frac{1}{2\pi} \int_o^{\infty} \frac{k^2 |\langle R_{l_o} | V | \phi_{l_o} \rangle|^2}{\omega_{ko}^2} dk. \tag{7.12}$$

To evaluate the integral above we assume a power law dependence for the matrix element $|\langle R|V|\phi_{l_o}\rangle|^2$. We know that the X-ray absorption coefficient falls off as some power of the photoelectron energy above the edge [60] and will show later that the matrix element above does also. We take the energy dependence of the matrix element to be,

$$|\langle R_{l_o}(k)|V|\phi_{l_o}\rangle|^2 \approx |\langle R_{l_o}(k_e)|V|\phi_{l_o}\rangle|^2 \left(\frac{\omega_{ko}}{|\omega_o|}\right)^{-\gamma}, \tag{7.13}$$

where γ is some arbitrary constant, and $|\langle R_{l_o}(k_e)|V|\phi_{l_o}\rangle|^2$ is evaluated at the X-ray absorption edge. Using this approximate form for the radial matrix element we may evaluate the high energy limit for the probability of secondary excitation using a standard integral from Gradsteyn and Ryzhik [54],

$$P_o^{\infty} = \frac{1}{2\pi} \left(\frac{2}{|\omega_o|}\right)^{\frac{1}{2}} \left[\frac{\Gamma\left(\frac{3}{2}\right)\Gamma\left(\gamma+\frac{1}{2}\right)}{\Gamma(\gamma+2)}\right] |\langle R_{l_o}(k_e)|V|\phi_{l_o}\rangle|^2, \tag{7.14}$$

where $\Gamma(x)$ is the Gamma function. With the correct form of $V(r)$ this expression should give identical results to equation (6.13) for the sudden limit of the shake-off probability.

It is now possible to substitute for P_o^∞ into the general result for the shake-off probability as a function of photoelectron energy (equation (7.11)). Then, to obtain the total probability of exciting any of the electrons in the atom, we must sum over all the n_o, l_o occupied initial states multiplying by the number of electrons, $n_{(n_o,l_o)}$, remaining in each state after the photoionisation,

$$P(\omega) = \sum_{n_o,l_o} \frac{n_{(n_o,l_o)} P_o^\infty \sqrt{2} |\omega_o|^{\gamma+\frac{1}{2}} \Gamma(\gamma+2)}{\Gamma\left(\gamma+\frac{1}{2}\right)\sqrt{\pi}} \int_o^{k_{max}} \frac{k^2 dk}{\omega_{ko}^{(2+\gamma)}(1+\omega_{ko}^2 t_o^2)}. \qquad (7.15)$$

This expression gives the correct form for the energy dependence of the secondary electron shake-off within this model. The magnitudes of the state dependent excitation probabilities, P_o^∞, can be taken from experiment or from theories such as that described in chapter 6. equation (7.15) then contains a single variable parameter, the energy dependence of the radial matrix element, γ.

In order to calculate the shake-off probabilities correctly using equation (7.15) we must know from which initial state the photoelectron originates. This is not a problem for the calculation of the EXAFS amplitude reduction factor, $s_o^2(\omega) = 1 - P(\omega)$, because, in an EXAFS experiment, the photoelectron is always excited from a well defined initial state. However, when comparing with shake-off experiments where, typically, the number of exited electrons are counted and which are generally performed at lower energies than EXAFS experiments, we must consider the possibility of exciting an electron from any of the occupied core states, ϕ_i. A photon incident on an atom may excite an electron in any of the occupied core states provided that $\omega > |\omega_i|$. Thus, to compare directly with experiment, we must weight the probability of exciting a secondary electron, given that the photoelectron comes from a state ϕ_i, with the probability that an electron in state ϕ_i does indeed absorb a particular photon. For example, if we hit a neon atom with a low energy photon of say, $100eV$ we may excite a 2s electron which could then excite a 2p or a 2s electron. Alternatively the photon

may be absorbed by a 2p electron which could then excite any of the 2s electrons or the 5 remaining 2p electrons. Both processes contribute to the total shake-off intensity. We must therefore include both possibilities in our calculation.

The total two electron transition probability can then be written in terms of the photon energy, ω, as,

$$P_T(\omega) = \sum_i \frac{\mu_o^i(\omega)}{\mu_o(\omega)} \sum_{n_o,l_o} \frac{n_{i(n_o,l_o)} P_{oi}^{\infty} \sqrt{2} |\omega_o|^{\gamma+\frac{1}{2}} \Gamma(\gamma+2)}{\Gamma\left(\gamma+\frac{1}{2}\right)\sqrt{\pi}} \int_o^{k_{max}} \frac{k^2 dk}{\omega_{ko}^{(2+\gamma)}(1+\omega_{ko}^2 t_{oi}^2)}. \tag{7.16}$$

Where $n_{i(n_o,l_o)}$ is now the number of electrons in the n_o, l_o initial state given that an electron has been removed from the state ϕ_i, and the relevant primary photoelectron energy is $E_p = \omega - |\omega_i|$. $\mu_o(\omega)$ is the single electron absorption coefficient and $\mu_o^i(\omega)$ is the contribution to the total absorption from all the electrons in the initial state ϕ_i. μ_o is simply the one electron absorption coefficient already calculated in chapter 3, because, in this model, the photoelectron is created before the excitation of the passive electrons. At photoelectron energies a long way above a particular absorption edge, where only that edge contributes significantly to the X-ray absorption coefficient, equation (7.16) reduces to equation (7.15) for the shake-off probability.

7.1.2 A Screened Core Hole Potential

The theory described in the previous section allows us to calculate the energy dependence of the secondary electron shake-off but cannot be used to find the magnitude of the shake-off intensity. In this section we describe an explicit form for $V(r)$, the core hole potential, with which we calculate the radial matrix element and hence the shake-off intensities directly.

Using a simple $\frac{1}{r}$ potential for the core hole gives values for the probabilities which are much too large. The $\frac{1}{r}$ perturbation is too strong: the majority of

passive electrons will not see a bare core hole because of the screening effects of the other passive electrons. This screening will, in general, be energy dependent. We can model the screening using the single plasmon pole dielectric function of Hedin and Lundqvist [9]. This energy-dependent dielectric function reduces the magnitude of the hole potential seen by the passive electrons. It will also introduce some many-body effects into our single electron theory. The correlation between electrons is known to be important especially at low primary photoelectron energies [20]. However, because of the complexity of calculations using multi-configuration wavefunctions it would be impractical, from the EXAFS point of view, to treat the electronic correlation rigorously. We can, however, include some of the effects of exchange and correlation by the use of the dielectric function.

To screen the time-dependent potential we must first write it in Fourier transform. With an unscreened core hole we have, from equation (7.5), that,

$$V(r,t) = \frac{1}{r}\left(1 - e^{(-t/t_o)}\right)\Theta(t), \tag{7.17}$$

where $\Theta(t)$ is the Heaviside step function which ensures that the perturbation is switched on at $t = 0$ when the photoelectron is created. The equation above may be Fourier transformed into q and ω space,

$$V(q,\omega) = \frac{4\pi}{\imath q^2}\left(\frac{1}{\omega} - \frac{1}{\omega - \imath t_o^{-1}}\right). \tag{7.18}$$

The screened time-dependent perturbation is then given by,

$$V(r,t) = \frac{1}{(2\pi)^4}\int d\mathbf{q}d\omega e^{\imath \mathbf{q}\cdot\mathbf{r}} e^{\imath\omega t} V(q,\omega)\epsilon^{-1}(q,\omega), \tag{7.19}$$

where $\epsilon^{-1}(q,\omega)$ is the causal single plasmon pole dielectric function. This is slightly different to the time ordered dielectric function defined earlier in that the causal $\epsilon^{-1}(q,\omega)$ has both poles in the upper half plane [41]. This is the correct form of dielectric function to use in this case because, if $\epsilon^{-1}(q,\omega)$ had poles in

either half plane, we would necessarily obtain a contribution to the screened perturbed potential before $t = 0$, ie. before the perturbation had been switched on. Thus, in the SPP approximation,

$$\epsilon^{-1}(q,\omega) = 1 + \frac{\omega_p^2}{2(\omega - \imath\eta)}\left(\frac{1}{\omega - \omega_q - \imath\eta} + \frac{1}{\omega + \omega_q - \imath\eta}\right), \tag{7.20}$$

where ω_p is the appropriate plasma frequency and ω_q the q dependent plasmon excitation energy. Substituting result (7.19) into equation (7.2) for the expansion coefficients of the perturbed wavefunction gives,

$$\frac{da_n}{dt} = \frac{e^{\imath\omega_{no}t}}{(2\pi)^4\omega_{no}}\left\langle \psi_n \left| \int \imath\omega e^{\imath(\omega+\imath\eta')t} V(q,\omega)\epsilon^{-1}(q,\omega) d\mathbf{q} d\omega \right| \phi_o \right\rangle. \tag{7.21}$$

We have added a convergence factor $exp(-\eta' t)$ to the integral, where η' is an infinitesimal. This corresponds physically to the finite core hole lifetime.

The above equation may now be integrated with respect to time from $t = 0$ to infinity to give an expression for the expansion coefficients a long time after the onset of the perturbation,

$$a_n(\infty) = \frac{1}{\omega_{no}(2\pi)^4}\left\langle \psi_n \left| \int d\mathbf{q} e^{\imath\mathbf{q}\cdot\mathbf{r}} \int d\omega \frac{\omega}{\omega_{no} + \omega + \imath\eta'} V(q,\omega)\epsilon^{-1}(q,\omega) \right| \phi_o \right\rangle. \tag{7.22}$$

The ω integral above may be performed using contour integration by closing contours in the lower half plane. All the poles in $V(q,\omega)$ and $\epsilon^{-1}(q,\omega)$ must lie in the upper half plane so that $V(r,t)$ is zero for $t < 0$. We therefore simply pick up a contribution from the pole at $\omega = -\omega_{no} - \imath\eta'$ to obtain,

$$a_n = \frac{\imath}{(2\pi^3)}\left\langle \psi_n \left| \int d\mathbf{q} e^{\imath\mathbf{q}\cdot\mathbf{r}} V(q,-\omega_{no})\epsilon^{-1}(q,-\omega_{no}) \right| \phi_{l_o} \right\rangle. \tag{7.23}$$

Hedin and Lundqvist define the q-dependent plasmon excitation frequency as in equation (3.32). We, however, use a slightly simpler form for ω_q so that we may evaluate the q-integrals analytically. We choose,

$$\omega_q^2 = \omega_p^2 + \frac{1}{4}q^4. \tag{7.24}$$

This plasmon excitation frequency exhibits the correct high and low q limits and should therefore give a good approximation to the true excitation frequencies. As we are dealing with atoms and not a free electron gas we again make use of the local density approximation (see chapter 3) to write the plasma frequency ω_p in terms of the radially varying atomic charge density.

Then, using this approximate form for ω_q and taking the infinitesimals in $\epsilon^{-1}(q,\omega)$ to zero we can integrate equation (7.23) directly using a result from Gradsteyn and Ryzhik [54],

$$\begin{aligned} a_n &= \frac{2it_o^{-1}}{\pi\omega_{no}(\omega_{no}+it_o^{-1})}\left\langle\psi_n\left|\int\frac{sin(qr)}{qr}\left[1+\frac{4\omega_p^2(r)}{4(\omega_{no}^2-\omega_p^2(r))-q^4}\right]dq\right|\phi_o\right\rangle \\ &= \frac{it_o^{-1}}{\omega_{no}(\omega_{no}+it_o^{-1})}\left\langle\psi_n\left|\frac{\omega_{no}^2-\omega_p^2(r)f(r,\omega_{no})}{r(\omega_{no}^2-\omega_p^2(r))}\right|\phi_o\right\rangle, \end{aligned} \tag{7.25}$$

where,

$$\begin{aligned} f(r,\omega_{no}) &= \frac{1}{2}e^{-br}+\frac{1}{2}cos(br) && \omega_{no}>\omega_p(r) \\ &= e^{-br/\sqrt{2}}cos(\frac{br}{\sqrt{2}}) && \omega_{no}<\omega_p(r), \end{aligned} \tag{7.26}$$

and,

$$b^4 = |\omega_{no}^2-\omega_p^2|. \tag{7.27}$$

There are weak divergences in the r-integrand for both $\omega_{no}>\omega_p$ and $\omega_{no}<\omega_p$ of the form $|\omega_{no}^2-\omega_p^2(r)|^{\frac{1}{4}}$.

As in the previous section we concentrate on the secondary electron shake-off and ignore the possibility of bound to bound transitions. We can then calculate the probability of exciting any of the secondary electrons into any continuum state following the absorption of a photon in the same way as before. We find,

$$\begin{aligned} P_T(\omega) &= \frac{1}{2\pi}\sum_i\frac{\mu_o^i(\omega)}{\mu_o(\omega)}\sum_{n_o,l_o}n_{(n_o,l_o)}\int_o^{kmax}\frac{k^2t_o^{-2}}{\omega_{ko}^2(\omega_{ko}^2+t_o^{-2})}\times \\ &\left|\left\langle R_{l_o}(k,r)\left|\frac{\omega_{ko}^2-\omega_p^2(r)f(r,k)}{r(\omega_{ko}^2-\omega_p^2(r))}\right|\phi_{l_o}\right\rangle\right|^2 dk, \end{aligned} \tag{7.28}$$

where the bra and ket now indicate $\int r^2 dr$ and $\phi_{l_o}(r)$ is merely the radial part of the initial state. As in the previous section, where the initial photoelectron state is known, for example in EXAFS experiments, the $\sum_i \frac{\mu_o^i}{\mu_o}$ term in the equation above may be removed.

The double electron photoionisation cross-section, $\sigma^{2+}(\omega)$, can be calculated within this model simply by multiplying equation (7.28) by the single electron absorption coefficient.

$$\sigma^{+2}(\omega) = \frac{1}{2\pi}\sum_i \mu_o^i(\omega) \sum_{n_o,l_o} n_{(n_o,l_o)} \int_o^{kmax} \frac{k^2 t_o^{-2}}{\omega_{ko}^2(\omega_{ko}^2 + t_o^{-2})} \times \left| \left\langle R_{l_o}(k,r) \left| \frac{\omega_{ko}^2 - \omega_p^2(r) f(r,k)}{r(\omega_{ko}^2 - \omega_p^2(r))} \right| \phi_{l_o} \right\rangle \right|^2 dk. \quad (7.29)$$

Equation (7.28) can be used to calculate numerical results for both the energy dependence and the magnitude of the secondary electron shake-off. However, we must take care when calculating the r-integral because of the divergence at $r = r_o$, the radius at which the radially varying plasma frequency is equal to the transition energy, ω_{ko}. This integral is not calculable using any of the standard NAG routines for poorly behaved integrands. We can, however, evaluate the integral in the region of the divergence using a Romberg integration routine.

Romberg integration is commonly used to solve problems involving improper integrals like the one above. In Romberg integration, the results from k successive evaluations of the extended trapezoid rule are used to remove all the terms in the error series up to $0(N^{2k})$. Basically, we calculate the integral for various numerical values of the step size h, then extrapolate to the continuum limit of $h = 0$. The Romberg integration routine is taken from Numerical Recipes in Fortran [75]. To use it, we must know the function to be integrated in analytical form rather than simply on a fixed numerical grid. The results for the final states and the radially varying plasma frequency, $\omega_p(r)$, are purely numerical, but this is not a problem in this situation. Both $\omega_p(r)$ and $R_l(kr)$ vary slowly on the

Herman-Skillman radial grids used. We therefore simply linearly interpolate the final state wavefunction and the plasma frequency in the region of the singularity in order to obtain the r-integrand as an analytical function.

The Romberg integration routine is used to calculate the integral only in the region of the singularity. To perform the whole integral we split the region into four. From $r = 0$ to $r_o - \delta$, from $r = r_o - \delta$ to r_o, from r_o to $r_o + \delta$ and finally from $r_o + \delta$ to $r = r_{mt}$, where δ is a small amount and r_{mt} is the muffin tin radius. The integrals over the two regions at the centre and the edge of the muffin tin are performed using the trapezium rule whilst the integrals over the two regions near to the divergence are calculated using the Romberg method. We use a mid point integration routine in these regions so that the r-integrand never has to be calculated at the divergence. The accuracy of the Romberg integration routine is controlled by a tolerance parameter. This is set so that a fractional accuracy of 10^{-4} is reached on the extrapolated final result.

In addition to the shake-off transition probability, Equation (7.28) can be used to calculate the ejected electron energy spectrum following the absorption of a photon. The k-integrand above simply gives the number of secondary electrons excited into continuum states within the small k range $k \rightarrow k + dk$ normalised to one. Experimentally we measure the number of secondary electrons within a small *energy* range. We have,

$$n(k)dk = \frac{1}{2\pi} \sum_{i,n_o,l_o} \frac{\mu_o^i(\omega) n_{(n_o,l_o)} k^2 t_o^{-2}}{\mu_o(\omega)\omega_{ko}^2(\omega_{ko}^2 + t_o^{-2})} \left| \left\langle R_{l_o}(k,r) \left| \frac{\omega_{ko}^2 - \omega_p^2(r) f(r,k)}{r(\omega_{ko}^2 - \omega_p^2(r))} \right| \phi_{l_o} \right\rangle \right|^2 , \tag{7.30}$$

then,

$$\begin{aligned} n(E) &= n(k)\frac{dk}{dE} \\ &= \sum_{i,n_o,l_o} \frac{\mu_o^i(\omega) n_{(n_o,l_o)} \sqrt{2E} t_o^{-2}}{2\pi\mu_o(\omega)\omega_{ko}^2(\omega_{ko}^2 + t_o^{-2})} \left| \left\langle R_{l_o}(k,r) \left| \frac{\omega_{ko}^2 - \omega_p^2(r) f(r,k)}{r(\omega_{ko}^2 - \omega_p^2(r))} \right| \phi_{l_o} \right\rangle \right|^2 , \end{aligned}$$

(7.31)

where $E = \frac{1}{2}k^2$ and $0 < E < \omega - |\omega_i|$. Equation (7.31) gives the contribution to the electron spectrum from the excited secondary electrons. We will also obtain a contribution to the ejected electron spectrum from the elastic photoelectrons at $E = \omega - |\omega_i|$ and from those photoelectrons which have excited secondaries at $E = \omega - |\omega_i| - \omega_{no}$.

7.1.3 The Two Electron Absorption Coefficient

In this model it has been assumed that an X-ray photon has been absorbed and a photoelectron created *before* the excitation of any of the secondary electrons. Thus, strictly speaking, the single and double electron absorption coefficients are identical within this theory. We can, however, slightly extend the model to give a rough approximation to the actual many electron absorption coefficient. We know that, in reality, the primary and secondary photoelectrons are produced at the same time. The energy of the secondaries will then affect that of the primary electron.

In chapter 6 (eqn.(6.5)) we saw that the single electron contribution to the many-body absorption coefficient was simply $s_o^2\mu_o(\omega)$. The single electron contribution to the total absorption is therefore less in a many-electron theory than in a purely one electron calculation. The difference between μ_o and $s_o^2\mu_o$ is, however, largely made up by the contribution to the absorption from multiple electron excitations.

The total absorption integrated over all energies must be the same regardless of whether many-electron effects are included or not because both single and many-electron calculations must satisfy the same sum rule [7],

$$\frac{c}{2\pi^2 Z\omega}\int \mu(\omega)d\omega = 1. \tag{7.32}$$

Also, in chapter 6 we showed that, at high energies, the single and many-electron calculations give identical results for $\mu(\omega)$. Thus, the many-electron effects cannot alter the absorption coefficient much from μ_o at any energy.

The theory discussed in this chapter gives a single electron contribution to the many-electron absorption coefficient which is not less than $\mu_o(\omega)$ because of the incorrect normalisation of the many-body final state. We correct for this in a somewhat *ad hoc* manner by writing the one electron contribution to the total, many-body, absorption coefficient as,

$$\mu_1(\omega) = (1 - \sum_n |a_n(\infty)|^2)\mu_o(\omega), \tag{7.33}$$

where $\mu_o(\omega)$ is the X-ray absorption coefficient given by a purely one electron theory and $a_n(\infty)$ is given by equation (7.25). When two electrons are excited the primary photoelectron must have its energy lowered from $\omega - |\omega_i|$ because of the energy carried away by the secondary. We allow for this by writing the contribution of two electron processes to the many electron absorption coefficient as,

$$\mu_2(\omega) = \sum_n |a_n|^2 \mu_o(\omega - \omega_{no}). \tag{7.34}$$

The total two electron absorption coefficient is then,

$$\mu(\omega) = \mu_o(\omega) + \sum_n |a_n|^2 (\mu_o(\omega - \omega_{no}) - \mu_o(\omega)). \tag{7.35}$$

Above the threshold where two electron excitations become possible, this calculation gives an absorption coefficient that is always larger than $\mu_o(\omega)$. This is because $\mu_o(\omega)$ always falls with increasing photon energy, at least for hard edges, so that $\mu_o(\omega - \omega_{no}) > \mu_o(\omega)$. This result will violate the sum rule on the absorption coefficient, presumably because we have neglected the relaxation energies and edge shifts in this simple analysis. In a true many-electron theory we would expect the electronic potential to be deepened due to the screening of

the passive electrons. This would move the absorption edge to slightly higher energies and hence the absorption coefficient would have to be slightly greater than the one electron result in order to satisfy the sum rule.

We can rewrite equation (7.34) in a form amenable for computation if we again ignore the bound to bound transitions and only consider two electron transitions where both electrons are excited into the continuum,

$$\mu(\omega) = \mu_o(\omega) + \frac{1}{2\pi}\int_o^{k_{max}} \sum_{i,n_o,l_o} \mu_o^i(\omega-\omega_{ko}) \frac{n_{(n_o,l_o)}k^2 t_o^{-2}}{\omega_{ko}^2(\omega_{ko}^2+t_o^{-2})} \left|\left\langle R_{l_o}\left|\frac{\omega_{ko}^2-\omega_p^2(r)f(r,k)}{r(\omega_{ko}^2-\omega_p^2(r))}\right|\phi_{l_o}\right\rangle\right|^2 dk. \tag{7.36}$$

We expect this result to look very similar to the absorption coefficient calculated in a one electron calculation. Experimentally we know that sharp steps in $\mu(\omega)$ are never observed at energies corresponding to the onset of two electron transitions. The consensus view is rather that the two electron transitions switch in slowly and almost indetectably [76].

7.2 Results

We can now proceed to compute numerical results for the two electron transition probabilities, the ejected electron spectra and the two electron absorption coefficient using equations(7.16), (7.28), (7.31) and (7.36).

The details of the calculation are much the same as in previous chapters. The initial states, $\phi_{l_o}(r)$, are taken to be the atomic orbitals tabulated by Clementi and Roetti [26] whilst the excited final states $R_l(kr)$ are the regular solutions to the Schrodinger equation described in chapter 2. The single electron absorption coefficient is calculated as detailed in chapter 3.

As in chapter 3, we treat free atoms by extending the atomic muffin tins to about 25 atomic units. This avoids any problems which may be caused by the

truncation of the atomic orbitals at the edge of the muffin tin sphere. The atomic potential is again assumed to be the sum of the Hartree potential and the $X\alpha$ potential, where the values of the variable parameter, α, have been taken from the tabulation of Schwarz [44]. When dealing with the noble gas elements, neon, and argon, we set the Fermi energy to $0.1eV$. Technically this should be zero. We use a small but finite E_f to avoid numerical problems with the calculation of very low energy photoelectron wavefunctions. When treating metals and semi conductors we set $E_f = 5eV$. The threshold energies for two electron excitation are taken from experiment. The threshold is not at $\omega = |\omega_i| + |\omega_o|$ because of relaxation effects following the creation of the photoelectron. The k integration in equation (7.28) is performed using a trapezium rule routine on a linear grid. The number of points in the grid are then increased until the result for the integration has converged. We find that 200 points are sufficient to converge the integral in all the situations investigated.

7.2.1 Calculation of γ

In deriving equation (7.16) for the shake-off probabilities we assumed the true radial matrix element to vary as some power of the primary photoelectron energy energy above the edge. We used the variable parameter γ to describe this energy dependence. The constant, γ, can be set by examining the energy variation of the radial matrix element with an unscreened core hole potential, $V(r) = \frac{1}{r}$. The matrix element with the unscreened core hole gives values for the excitation probabilities which are much larger than those observed experimentally but has an energy dependence similar to that of the true matrix element. In the left hand graph of figure 7.1 we plot $log|\langle R_{l_o}|\frac{1}{r}|\phi_{l_o}\rangle|^2$ against $log\left(\frac{E_p+E_o}{E_o}\right)$ for the two most weakly bound initial states of two different elements, copper and neon. It is the most weakly bound states that provide the majority of the contribution to the

secondary excitation probability.

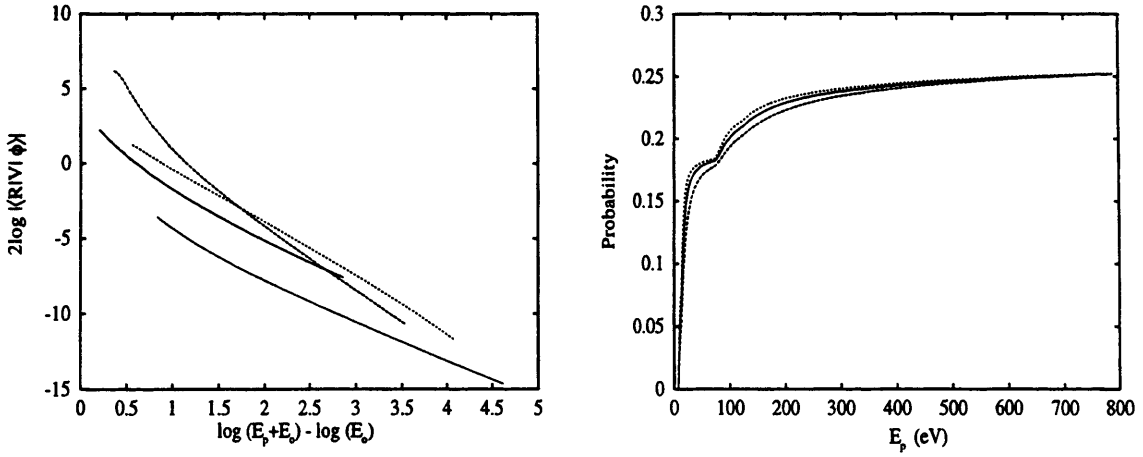

Figure 7.1: The left hand graph shows $log\,|\langle R_{l_o}|V|\phi_{l_o}\rangle|^2$, plotted against $log\left(\frac{E_p+E_o}{E_o}\right)$ for various initial states: neon 2s (solid line), Ne 2p (dashed line), Cu 3d (short dashed line), and Cu 4s (dotted line). The right hand curve shows the probability of secondary electron excitation following a K-edge photoionisation in copper plotted as a function of the photon energy above the K-edge in electron volts. The three curves show results obtained with values of, $\gamma = 3.4$ (solid curve), $\gamma = 2.0$ (long dashed curve), and $\gamma = 5.0$ (short dashed curve).

$log|\langle R_{l_o}|V|\phi_{l_o}\rangle|^2$ varies approximately linearly with $log\left(\frac{E_p+E_o}{E_o}\right)$ over most of the energy range. The gradient varies between $\gamma = 2.7$ (neon 2s), and $\gamma = 4.3$ (neon 2p), over all the initial states examined. We approximate γ as the average of the gradients plotted in the left hand graph of figure 7.1, $\gamma = 3.4$. In the right hand plot of this figure it can be seen that the probability of secondary excitation is not very sensitive to changes in γ. Varying the energy dependence parameter from $\gamma = 2$ to $\gamma = 5$ results in changes in the excitation probability of less than 5%.

7.2.2 Secondary Electron Shake-off Probabilities

Neon

In figure 7.2 we compare the secondary electron excitation probabilities for neon, measured by Carlson and Krause (CK) [58] with calculated results from Thomas [20] and results found using a model energy dependence and the sudden approximation (equation (7.16)). The shake-off probabilities are plotted against the photon energy.

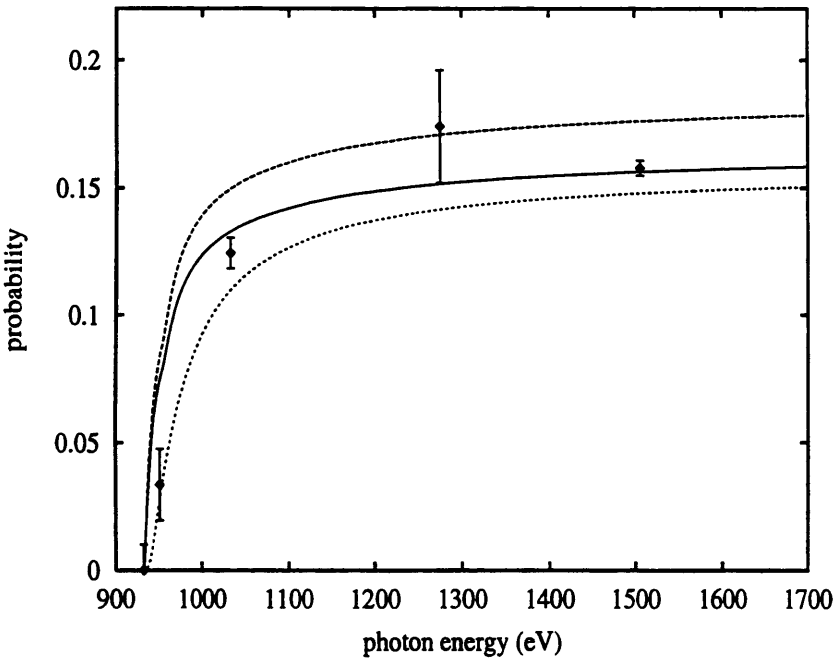

Figure 7.2: The probability of secondary electron excitation as a function of photon energy following the creation of a photoelectron from a 1s state in neon. The points with error bars are data from Carlson and Krause [58], the solid line shows the calculated result from equation (7.16) normalised to the experimental data in the high energy limit. The dashed line is the calculated result with the high energy probabilities found using the sudden approximation, whilst the dotted line gives Thomas' result, equivalent to equation (7.8).

CK measure the shake-off probabilities by examining the relative populations of the various types of neon ions produced after irradiating neutral neon gas with

X-rays above the K-edge absorption energy. CK argue that 99% of the neon atoms in which a K-shell photoabsorption takes place will undergo an Auger transition (the KLL Auger). This will promote an additional electron into the continuum, transforming the singly ionised neon into Ne^{+2}. If a further passive electron is excited via a shake-off transition then Ne^{+3} will be created. CK therefore take the probability of single electron shake-off to be the number of Ne^{+3} ions divided by the total number of neon ions detected.

To obtain the plots in figure 7.2 we have estimated the threshold energy for two electron transitions as $911.5eV$ from the data (25.5eV above the k-edge). The solid and dashed curves have been calculated with equation (7.16) with the values of P_o^∞ taken from chapter 6 (eqn.(6.13)). The solid curve has then been normalised to the high energy limit of the measured results of CK (15.8%) so that it may be compared directly to the result of Thomas (the dotted curve).

The calculated result (eqn.(7.16)) shows reasonable agreement with experiment although it cuts in slightly too quickly at low energies. Thomas' result, which does not include the possibility of transitions into all of the energetically available excited states, fits well at low energies but generally rises too slowly. It has not reached its sudden limit even by 800eV above the edge. The calculated and measured shake-off probabilities, however, reach their full magnitude within approximately 50eV of the two electron excitation threshold. The magnitudes found using the sudden approximation are slightly too large. We find a high energy limit of 17.8% as compared to 15.8% from experiment.

In figure 7.3 we again plot the secondary electron excitation probabilities for neon, this time following the creation of a 2s or 2p hole, ie. for low energy photons. The calculated result gives the energy dependence of the shake-off probabilities reasonably well although, again, it cuts in a little too quickly at low energies. The high energy limit given by the sudden approximation (13.2%) agrees extremely

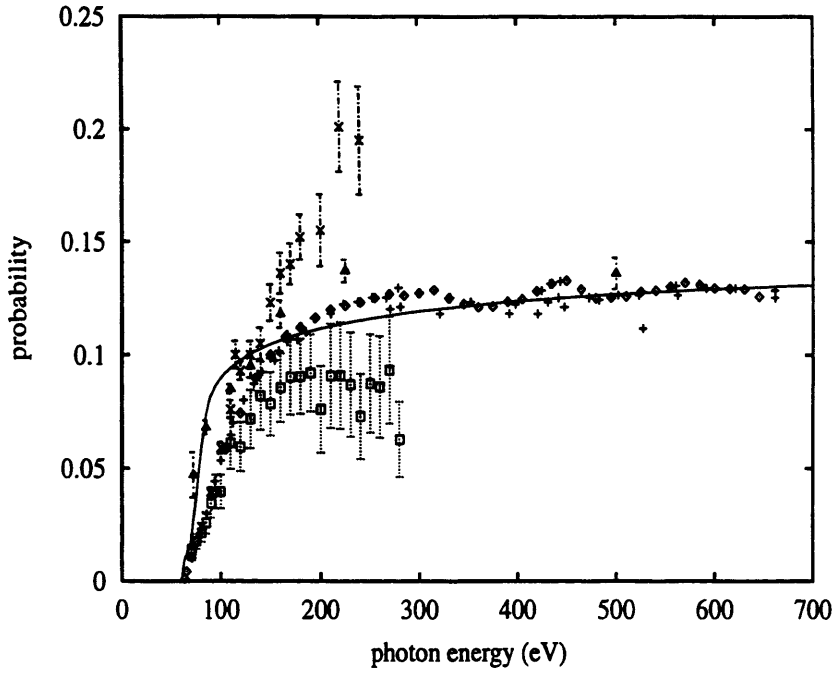

Figure 7.3: The probability of secondary electron excitation as a function of photon energy following the creation of a photoelectron from an L shell in neon. The points are experimental data: diamonds from Bartlett *et al* [77], crosses from Samson *et al* [78], open squares with error bars from Holland *et al* [79], crosses with error bars from Wight and Van der Viel [80] and triangles with error bars from Carlson [67]. The solid line shows the calculated result from equation (7.16) with the magnitude given by the sudden approximation.

well with the 13% measured by Bartlett *et al* [77]. The threshold energy for two electron transitions is given as $62.5eV$ by Bartlett *et al.*

There is some disagreement between the experimentally measured data sets. The results produced by Bartlett *et al* [77] are, however, the most recent and therefore, presumably, the most accurate. Bartlett *et al* claim that the measurements of Holland *et al* [79] may underestimate the two electron transition probability due to a stray light problem.

Stray light is a commonly recorded problem in measurements of this type. The X-rays are never perfectly monochromated and thus there exists the possibility that photons of energy lower than that expected may reach the sample. These

X-rays may excite a single electron but are insufficiently energetic to promote two electrons into the continuum. The numbers of singly ionised gas atoms are therefore increased in proportion to the number of doubly ionised gas atoms leading to an apparent decrease in the measured two electron excitation probability.

Wight *et al* [80] measure the 2 electron excitation probability after bombarding the neon atoms with high energy photoelectrons. Bartlett *et al* suggest that these measurements may overestimate the shake-off probability due to additional ionisation channels being opened by momentum transfer from the incident electron beam to the target atoms.

Normal Auger transitions cannot take place during 2s,2p photoionisation in neon because there is insufficient energy available (see figure 7.4). However, Becker *et al* [81] show that so-called participator Auger events are possible in which Auger transitions take place after the secondary electron shake-off. These transitions transform Ne^{+2} ions into Ne^{+3} reducing the measured two electron excitation probabilities by $\sim$ 3% in the high energy limit. We ignore this small effect. Compared to the uncertainties in the rest of the data it is negligible.

Figure 7.5 shows the shake-off probability for neon following an L-edge photoionisation calculated using the dynamically screened core hole (eqn.(7.28)). We obtain surprisingly good results from this screened single electron theory. The magnitudes are very close to those found experimentally over the whole of the energy range investigated. Also the energy dependence of the calculated result is a fair approximation to that measured experimentally. The calculated result for the neon L edge matches the data well at low energies and appears to exhibit the correct energy dependence up to a photon energy of $\sim 300eV$. The theoretical result has not, however, reached its sudden limit even by 700eV above threshold but gives shake-off probabilities which are still rising with energy. We believe

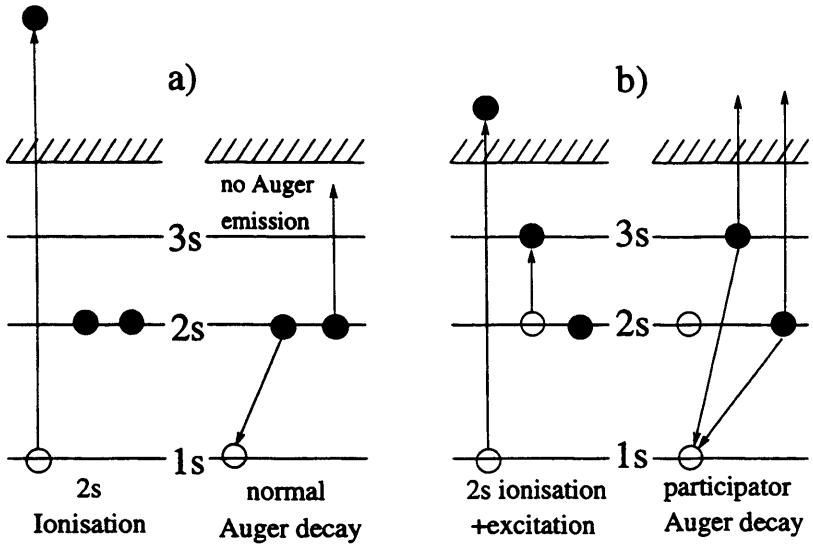

Figure 7.4: Reproduced from Becker *et al* [81]. Schematic level and transition diagram of neon 2s photoionisation (a) without and (b) with accompanying excitation and subsequent recombination processes.

this is due to a fault in our model dielectric function. With the simplified single plasmon pole, LDA, dielectric function (eqn.(7.20)) we may be under-screening the core hole at high primary photoelectron energies. A more accurate form of the dielectric function might therefore account for this incorrect behaviour as the calculated result is strongly dependent on the form of the screening used.

In figure 7.6 we show the calculated result using a slightly different form of the screening (see appendix A). The solid curve is evaluated using a q dependent plasmon frequency of $\omega_q = \omega_p + \frac{1}{2}q^2$. This is a worse approximation to the actual Hedin-Lundqvist definition of the SPP plasmon excitation frequency than that used in equation (7.24). We can see that the results calculated using the q^2 form of the dielectric function are, indeed, much worse that those found using the q^4 form. The q^2 form significantly over-screens the core hole at all primary photoelectron energies. As the calculation varies significantly with the form of the screening chosen we would expect a more accurate dielectric function, for

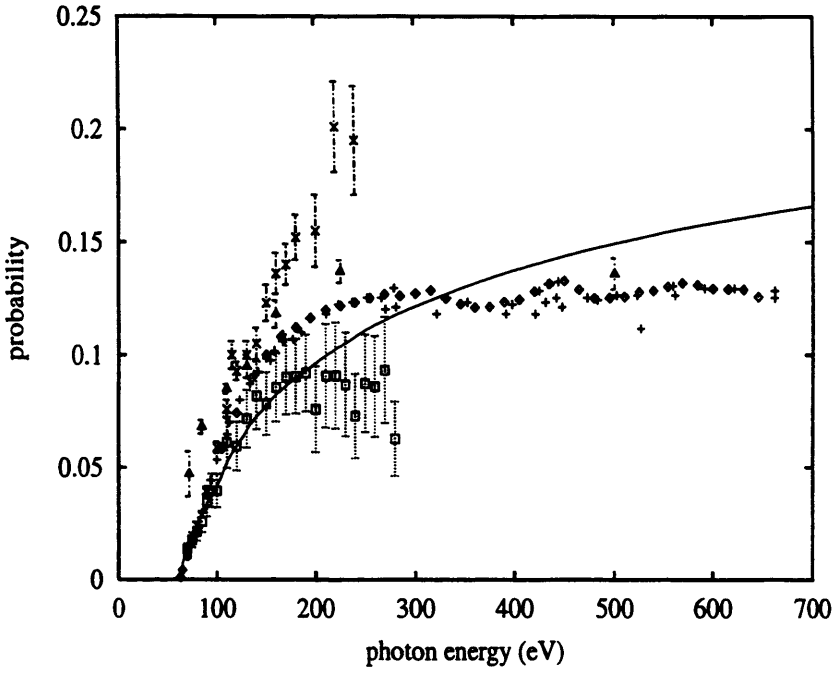

Figure 7.5: The probability of secondary electron excitation as a function of photon energy following the creation of a photoelectron from an L shell in neon. The solid line shows the result calculated using a screened hole potential (eqn.(7.28)). The points are experimental data: diamonds from Bartlett *et al* [77], crosses from Samson *et al* [78], open squares with error bars from Holland *et al* [79], crosses with error bars from Wight and Van der Viel [80] and triangles with error bars from Carlson [67].

example the true single plasmon pole result from Hedin and Lundqvist or an atomic dielectric function such as that given in chapter 3 to produce better results for the calculated shake-off probabilities.

In figure 7.6 we also show a result in which the final states of equation (7.28) were calculated in the presence of the Hartree potential. ie with a Slater exchange parameter of $\alpha = 0$. The results found using $\alpha = 0$ and $\alpha = 0.73$ (from Schwarz's table [44]) are very similar. The calculation is not particularly sensitive to small changes in the atomic potential, and we are therefore justified in using the $X\alpha$ potential to model the electronic exchange.

Figure 7.7 shows the shake-off probability for neon following a K-edge

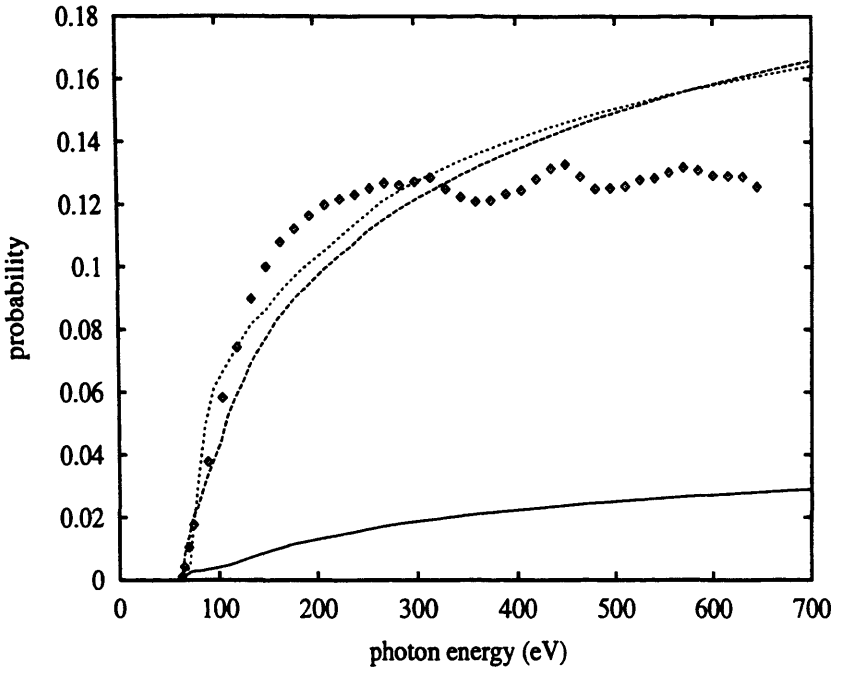

Figure 7.6: The probability of secondary electron excitation as a function of photon energy following the creation of a photoelectron from an L shell in neon. The points are experimental data: diamonds from Bartlett *et al* [77]. The three lines are calculated using two different forms of screened core hole potential. The solid line with a q dependent plasmon frequency of $\omega_q = \omega_p + \frac{1}{2}q^2$ and the dashed and dotted lines with $\omega_q^2 = \omega_p^2 + \frac{1}{4}q^4$. In the calculation of the dotted line we have assumed the atomic potential to be the Hartree potential alone.

photoabsorption. Again, the result calculated using a screened core hole potential matches experiment reasonably well, the main failing being in the energy dependence at high photon energy, where the calculated probabilities are still rising. We also show the sudden approximation result in figure 7.7 for comparison. This has a better energy dependence but gives magnitudes no better than the screened core hole result. Effectively this plot shows the energy dependence of the EXAFS amplitude reduction factor, $s_o^2(\omega)$, which is just the probability that none of the passive electrons are excited into the continuum (see sec.(7.2.6)). For neon, at least, both theories give the shake-off probabilities, and hence s_o^2, to within the $\pm 10 - 15\%$ needed for EXAFS purposes. For the neon L edges the experimental

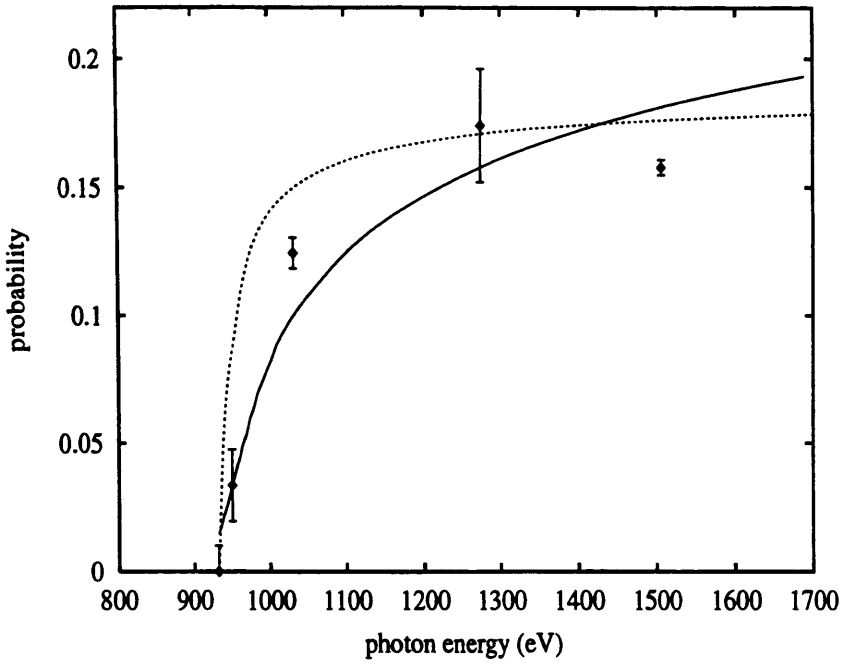

Figure 7.7: The probability of secondary electron excitation as a function of photon energy following the creation of a photoelectron from the K shell in neon. The points are experimental data measured by Carlson and Krause [58]. The solid line shows the result calculated using a screened core hole potential (eqn.(7.28)). The dotted line shows the result calculated using a model energy dependence and the sudden approximation (eqn.(7.16)).

probabilities are not quite $1 - s_o^2(\omega)$ because the primary photoelectron initial state is unknown. This has been discussed in section 7.1.1.

Argon

The two methods of calculating the shake-off described in this chapter have one major advantage. They may be used to calculate the secondary electron excitation probabilities for any absorption edge of any element very easily. In the next two figures we compare the calculated results for argon with experimental data taken from various sources.

Figure 7.8 shows the shake-off probabilities against photon energy following a

K-edge photoionisation. The experimental results (points with error bars) have been measured by Armen *et al* [82]. These authors measured the Auger satellites in order to determine the M-shell secondary electron excitation. Up to $250eV$ above threshold only M-shell secondary excitation is energetically possible. The result calculated using the screened core hole is a reasonable approximation to the measured data although the energy dependence is not as good as for neon. At high photon energy the calculated result is, again, still rising. Also, at low photon energies the calculated result cuts in too slowly. The sudden approximation result (the dotted line) shows excellent agreement with both the experimental magnitudes and energy dependence. We find a high energy limit of 25.0% from the sudden approximation compared to about 24% from the data. Again, this result is effectively the EXAFS amplitude reduction factor. We obtain excellent agreement for $s_o^2(\omega)$ for argon using result (7.15) whilst the screened core hole method gives a result which appears adequate for EXAFS purposes.

The shake-off probabilities following M-edge photoionisation are plotted in figure 7.9. The screened core hole results cut in too slowly but agree fairly well with the experimental data between a photon energy of about 50 to 200 volts. The sudden approximation results mimic the energy dependence of the data better but give magnitudes that are too small at high energies. The sudden approximation gives a high energy limit of 13.8% whereas the data tends to a limit of approximately 18%.

We cannot directly compare our results to the experimental points above the L-edge photoionisation threshold ($\sim 250eV$). At each absorption edge the calculated two electron excitation probabilities exhibit a sharp fall almost to zero. At the edge $\mu_o(\omega)$ increases sharply whilst the two electron excitation probabilities, following a photoabsorption at the new edge, switch in more slowly. This effect is not seen in the data, because, above the L-absorption edge, LMM

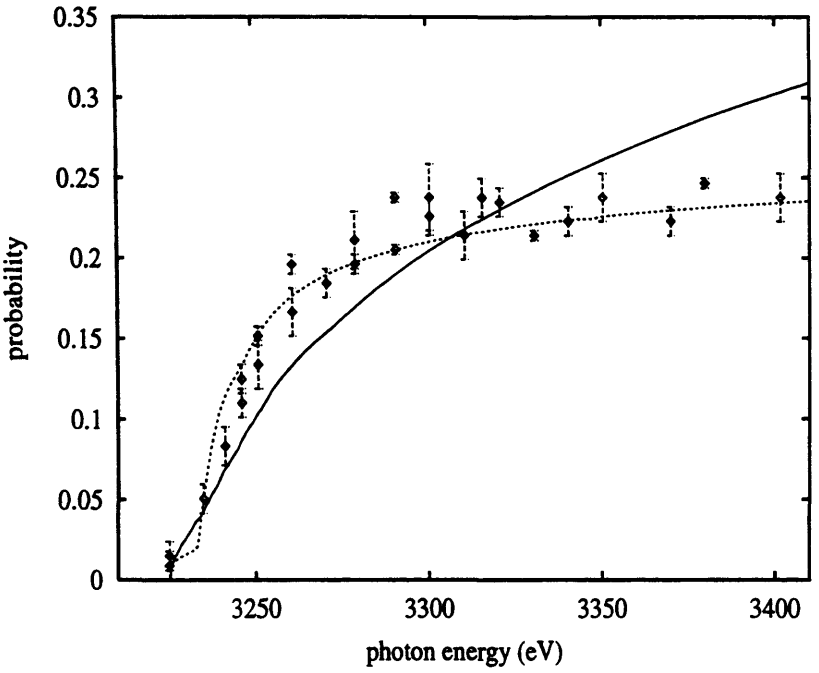

Figure 7.8: The probability of secondary electron excitation as a function of photon energy for the argon K-edge. The points are experimental data from Armen *et al* [82]. The solid line shows the result calculated using a screened core hole potential (eqn.(7.28)) whilst the dashed line shows the result calculated from equation (7.16). Threshold is measured at 43.4eV.

Auger transitions become possible. These transitions cause a sharp rise in the number of Ar^{+2} ions detected which gives an apparent increase in the shake-off probability calculated from the ratio of the number of 2+ ions to the total number of ions detected. The apparent rise in the shake-off intensity can just be seen in the data from Holland *et al* [79].

7.2.3 The Ejected Electron Spectrum

The ejected electron shake-off spectra can be investigated using equation (7.31). In figure 7.10 we plot the observed and calculated primary photoelectron energy spectrum. This contains a contribution from the elastically scattered photoelectrons in addition to those which have lost energy in exciting a secondary

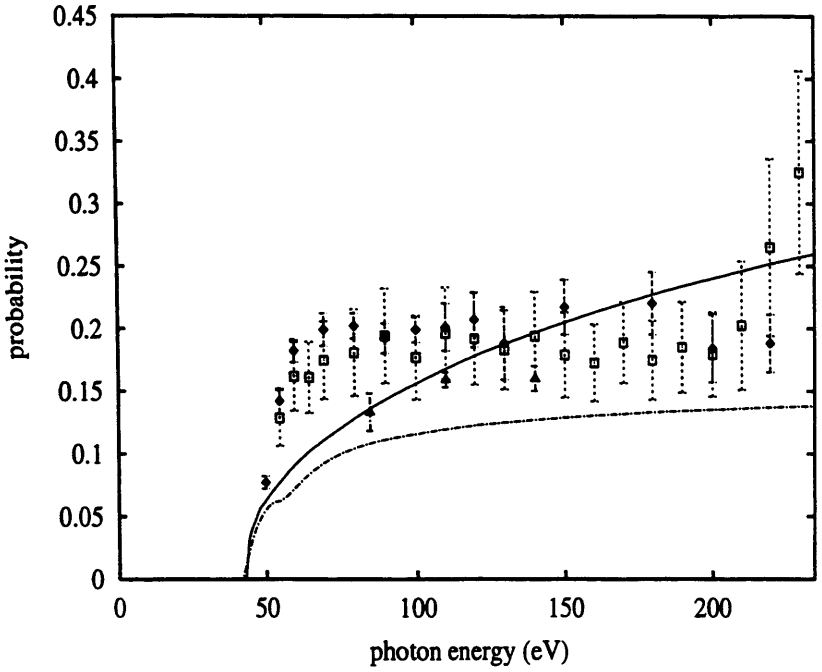

Figure 7.9: The probability of secondary electron excitation as a function of photon energy for argon. The points are experimental data: diamonds with error bars from Wight and Van der Viel [80], open squares with error bars from Holland *et al* [79] and triangles with error bars from Carlson [67]. The solid line shows the result calculated using a screened core hole potential (eqn.(7.28)), the dashed line shows the result calculated using equation (7.16) with magnitudes given by the sudden approximation.

into the continuum. Equation (7.31) can be used to calculate the number of electrons within the energy range $E \rightarrow E + dE$ normalised to 1. In order to compare directly with the data of Carlson [67] we normalise this result to Carlson's at the second peak in the shake-off spectrum due to 2p,2s shake off. We also use an energy scale of 'Channels', where 1 Channel = 2.05eV and a channel of zero corresponds to an electron energy of 100eV, as in Carlson's paper. To obtain the relative sizes of the peaks for the elastically scattered photoelectrons we have examined the ratio of the 2p and 2s contributions to the absorption coefficient. We find $\mu_o^{2p}/\mu_o^{2s} = 1.89$, this is the ratio between the number of 2p and the number of 2s photoelectrons created. From Carlson's data we can see

that experimentally we obtain approximately twice as many 2p photoelectrons as 2s photoelectrons. In plotting our data we have normalised the 2p peak to that of Carlson and broadened the energy distributions using a Gaussian of half width 2.05eV centred on the 2p and 2s binding energies.

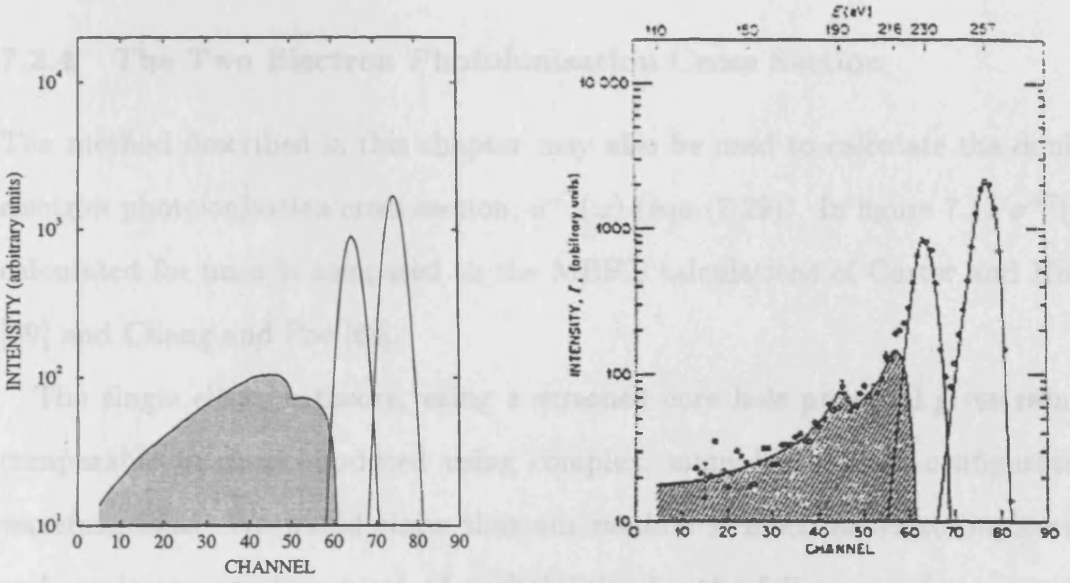

Figure 7.10: The primary photoelectron energy spectrum. The graph on the left is calculated using the screened core hole potential as described in the text. The graph on the right is reproduced from Carlson [67].

The inelastic part of the calculated secondary electron spectrum does not show the same features as that measured experimentally. The calculated shake-off peaks are too broad and we do not obtain the correct ratio between 2p,2p shake-off and 2s,2p shake-off. From the previous section, however, we know that the total number of electrons (the area under the curve) is about right. We also obtain a reasonable agreement in the fall off in the number of primary electrons with energy. The intensity falls from $\sim$ 100 at the 2s,2p peak to approximately 15 at 5 channels, compared to Carlson's measured value of about 20 at 5 channels.

We believe the discrepancies between the calculated and measured results are due to inaccuracies in the calculated low energy, final state phase-shifts. Unlike

the previous calculation, the calculation of the secondary electron spectrum is sensitive to changes in the details of the atomic potential. We should therefore use some form of energy-dependent atomic potential rather than the simple $X\alpha$ Slater exchange.

7.2.4 The Two Electron Photoionisation Cross Section

The method described in this chapter may also be used to calculate the double electron photoionisation cross section, $\sigma^{+2}(\omega)$ (eqn.(7.29)). In figure 7.11 $\sigma^{+2}(\omega)$ calculated for neon is compared to the MBPT calculations of Carter and Kelly [69] and Chang and Poe [68].

The single electron theory, using a screened core hole potential gives results comparable to those produced using complex, many-body, multi-configuration wavefunctions. We would claim that our method is much easier to implement and, as it can produce a set of probabilities for the full range of energies for a given element in under 30 seconds, is probably much quicker to use than any comparable many-body calculation. Carter and Kelly [69] use their MBPT theory method to give good agreement with the argon data and less good agreement with the neon shake-off data. Their calculated results fit the experimental neon cross sections well at high energies but not between $\omega = 60eV$ to $\omega = 135eV$. They claim that this is a fault of the potential used. The V^{N-2} potential, calculated with 2 electrons missing from the atom, overestimates $\sigma^{2+}(\omega)$, whereas the V^{N-1} potential (with one electron missing from the atom) underestimates the cross sections at low energies. Carter and Kelly claim that the physical situation lies somewhere between the two cases and could be obtained by including more terms in the perturbation series. By screening our core hole potential we obtain results for the cross section which bisect the two curves of Carter and Kelly at low energies. We already know from figure 7.5 that we obtain reasonable agreement

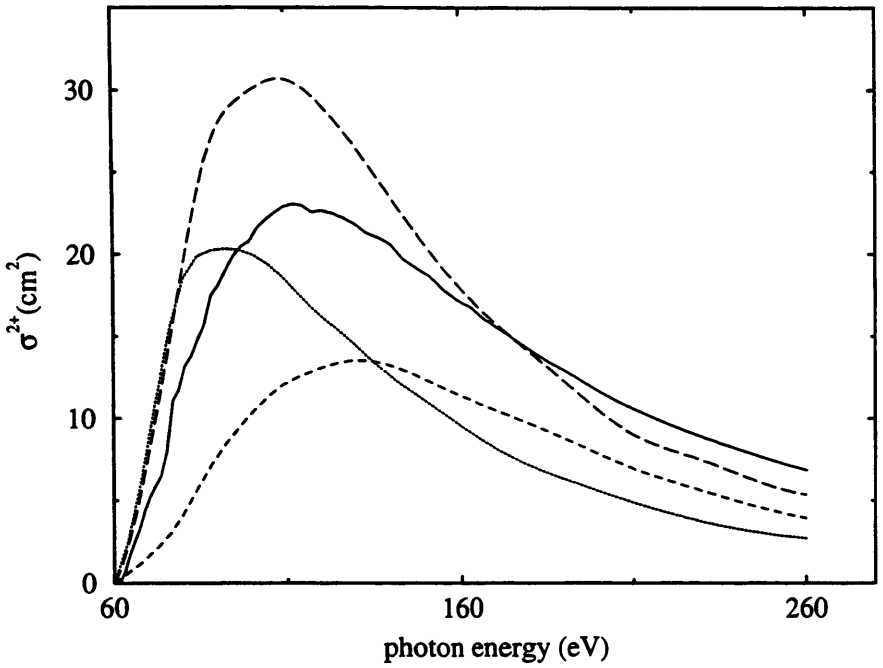

Figure 7.11: The two electron excitation cross section for neon. The solid line gives the calculated result from equation (7.29). The long dashed line is that produced by Chang and Poe [68], whereas the short dashed line and the dotted line are calculated by Carter and Kelly [69]. The short dashed line is calculated using the V^{N-1} potential and the dotted line using the V^{N-2} potential. The results by Carter and Kelly [69] and Chang and Poe [68] have been reproduced from figure 7 of reference [69].

with experiment at low energies. At high energies, however, the cross section calculated using equation (7.29) is larger than those produced by Carter and Kelly or by Chang and Poe. This is probably because we underestimate the screening of the core hole at high photoelectron energies. This overestimates the two electron cross section and therefore gives larger than expected results for the shake-off probabilities at high photon energies.

7.2.5 The Two Electron Absorption Coefficient

In section 7.1.3 we discussed an approximate method for determining the two electron absorption coefficient. Strictly speaking, in the time-dependent perturbation theory discussed, the single and double electron absorption coefficients are identical. However, in section 7.1.3 we used an *ad-hoc* argument in order to obtain an idea of the shape of the two electron X-ray absorption coefficient.

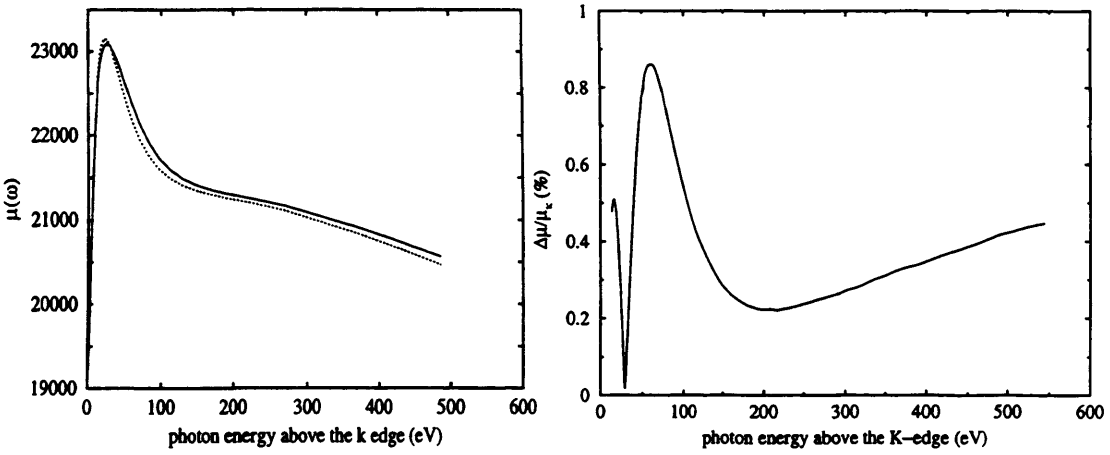

Figure 7.12: The two electron absorption coefficient for Bromine. The graph on the left shows a comparison between the X-ray absorption coefficient calculated using a purely one electron calculation (the dotted line) and $\mu(\omega)$ calculated using equation (7.36) (the solid line). The graph on the right shows the difference between the two curves normalised to the K-edge absorption as a percentage.

On the left of figure 7.12 we show the X-ray absorption coefficient for Bromine as a function of photon energy. The single and double electron absorption coefficients have very similar magnitudes. This must be the case because, first, both calculations satisfy the sum rule, and second, single electron calculations of $\mu(\omega)$ such as those produced by Veigele [45] give reasonable agreement with experiment. From detailed experimental studies of multiple electron excitations by, for example Deutsch and Hart [76], Kodre *et al* [83] and Filipponi [84] we

know that the features produced on the absorption edge due to multiple electron excitations are small, of the order of 1%. Although the total contribution to $\mu(\omega)$ from two electron events is approximately 20−30% the two electron excitations do not produce sharp jumps in the absorption coefficient of this magnitude because of the slow cut in of the multiple electron transition probabilities with energy. Experimentally the two electron shake-off events can be seen as bumps on the absorption coefficient [84]. We do not see these features on the calculated two electron absorption coefficient because, in this model, the energy dependence is too slow. From the curve to the right of figure 7.12 we can see, however, that we do obtain multiple electron features of about the right order of magnitude. In calculating $\Delta\mu/\mu_k$ in figure 7.12 we have assumed the one electron calculation to be equivalent to the smooth atomic background. The difference between the one and two electron calculations ($\Delta\mu$) therefore shows up the multi-electron features.

7.2.6 The Amplitude Reduction Factor

The probability of secondary electron shake-off is very closely related to the amplitude reduction factor used in EXAFS. This factor is used in the purely one electron EXAFS calculation to account for many-electron excitations at the absorbing atom. We argued previously that only those photoelectrons which did not excite passive electrons into the continuum would contribute to the EXAFS signal, thus the amplitude reduction factor is simply the probability that none of the secondary electrons are excited into the continuum,

$$s_o^2(\omega) = 1 - P(\omega), \tag{7.37}$$

where $P(\omega)$ may be taken from equation (7.15) or from equation (7.28) with the relevant modifications as discussed in the text.

The theory used in this chapter describes both the photoelectron and the core

hole, it includes both the intrinsic and extrinsic EXAFS loss processes at the central atom. At high energies, of course, the extrinsic losses tend to zero and equations (7.15) and (7.28) reduce to the sudden limit for the shake-off probability discussed in chapter 6. Because equation (7.37) for the amplitude reduction factor includes all the EXAFS losses at the central atom we cannot use it directly in equation (1.3) for the EXAFS. We must first modify the mean free path term in equation (1.3) so that it describes the extrinsic losses only at the scattering atom. For the mean free path term we therefore have, $exp\Big(-2(r_j - r_o)/\lambda\Big)$, where r_j is the distance to the scattering atom and r_o subtracts off the contribution from the central atom.

In section 7.2.2 we obtained results, effectively for $s_o^2(\omega)$, that agreed well with experimental data for neon and argon following K-edge photoabsorption. In figure 7.13 we compare values of $s_o^2(\omega)$ calculated using the two methods in this chapter with data produced by Stern *et al* [85] for Bromine. The magnitudes of the data and the two calculated sets of results agree well at high photon energies although the result calculated using the screened core hole is still falling at $700eV$ above the edge. Both the calculated curves cut in far quicker than the experimentally measured set of points. The measured amplitude reduction does not deviate from unity until approximately 100eV above the edge, this is therefore the primary photoelectron energy at at which the first secondary electrons are excited into the continuum. We find this result surprising. The most weakly bound state in Bromine has a binding energy of only $\sim 5eV$ [28] which suggests that we should see secondary electrons excited into the continuum at a photon energy of at most 10eV above the K-edge. Data from Kodre *et al* [83] supports this view. Kodre *et al* find the onset of the 3d shake-off in Bromine to be $90eV$ above the K-edge. The 4s and 4p shake-off must appear at much lower energies than this.

In figure 7.14 we have plotted the amplitude reduction factor against photon

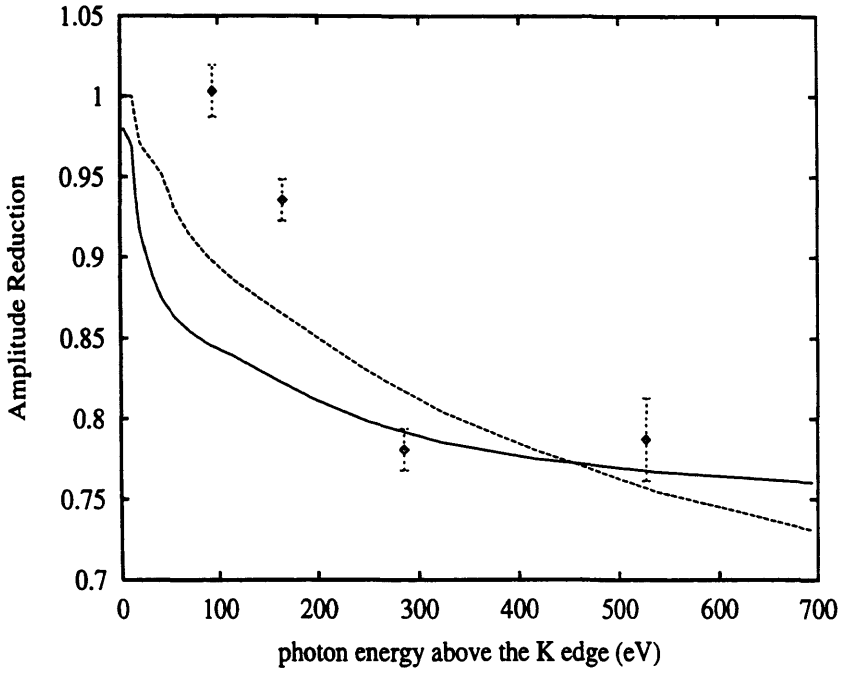

Figure 7.13: The amplitude reduction factor $(1 - P(\omega))$ as a function of the photon energy above the K-edge for Bromine. The solid line shows the result calculated using the sudden approximation with a model energy dependence (eqn.(7.16)) whilst the dashed line shows $s_o^2(\omega)$ calculated using the screened hole potential (eqn.(7.28)). The diamonds with error bars are experimental data measured by Stern *et al* [85].

energy above the K-edge for copper, silicon and silver. The points give the results calculated using a model energy dependence and the sudden approximation whilst the lines are values of $s_o^2(\omega)$ calculated using the screened core hole. From chapter 6 we know that the sudden approximation gives reasonable high energy limits for the amplitude reduction. The energy dependence also fits in with the commonly held view that $s_o^2(\omega)$ reaches its full magnitude within at most a couple of hundred volts of the edge. The results using the screened core hole for copper and silicon are also surprisingly good. The energy dependence seems reasonable and the magnitudes are within 15% of those given by the sudden approximation at 800eV above the edge. The screened core hole result for silver is not so good. The

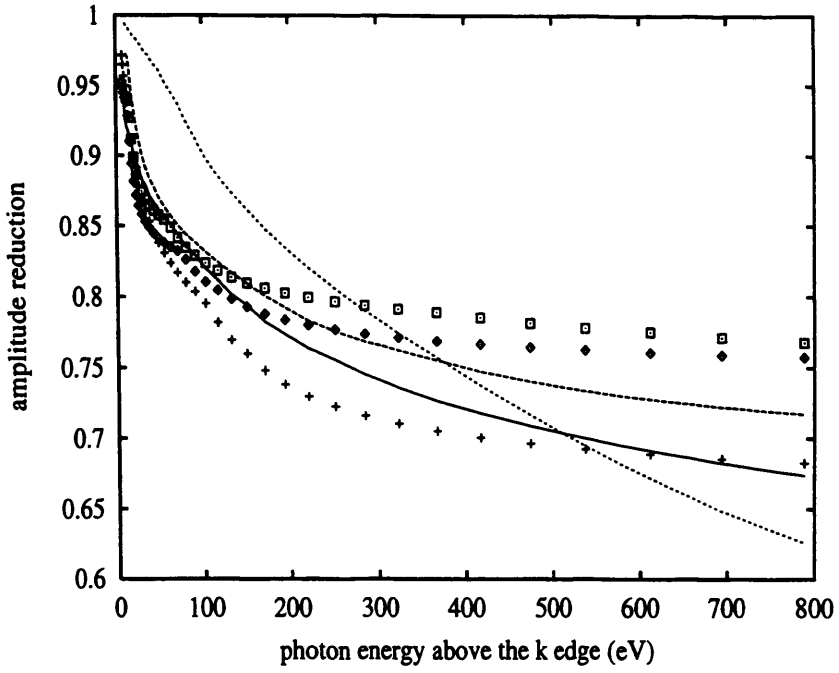

Figure 7.14: The amplitude reduction factor $(1 - P(\omega))$ as a function of the photon energy above the K-edge. The solid line shows the result calculated using a screened core hole potential (eqn.(7.28)) for copper, the dashed line for silicon and the dotted line for silver. The points are results found using the sudden approximation and a model energy dependence: diamonds for copper, crosses for silicon and squares for silver.

amplitude reduction varies much more slowly with energy than we would expect and looks to be tending toward a high energy limit of less than 0.6, compared to the sudden approximation result of 0.8. We believe that the poor results for Silver may be due to the large number of weakly bound electrons in the 4d orbitals. The calculation for silver is more sensitive to changes in the low energy final state phase-shifts. It may be that, in this case, the Slater $X\alpha$ potential is an inadequate representation of the true electronic exchange.

7.2.7 Connection with EXAFS Data Analysis

In this chapter we have described a method by which an energy-dependent amplitude reduction factor may be quickly calculated for all edges of all elements. This factor can then be used, along with the appropriate mean free path term, in a single electron theory using real atomic scattering potentials to calculate EXAFS of the correct magnitude. Of course, the losses to the photoelectron wave could be evaluated using a complex scattering potential and, from chapter 4, we know that the Hedin-Lundqvist (HL) potential gives a good, if somewhat fortuitous, agreement with experiment. However data analysis programs using complex scattering potentials are complex to write and maintain, especially when multiple scattering must be taken into account. Programs using only real potentials are extremely simple in comparison. The Dirac-Hara exchange potential gives better phase-shifts for EXAFS purposes than the real part of the HL potential [51]. Using this real scattering potential and an energy-dependent loss factor such as that described in this chapter we would expect to obtain good EXAFS spectra without the complications of the complex phase-shift approach.

In figure 7.15 we compare calculated EXAFS spectra for copper metal. As described in chapter 4, section 4.2.4, we used the Daresbury program EXCURV98 [14] to calculate an EXAFS spectrum for Cu foil with both the HL (solid line) and the $X\alpha$ potentials using only the first shell of scattering atoms. The spectra calculated using the $X\alpha$ exchange is slightly out of phase with the best fit HL spectra, it is also much larger as it includes none of the losses to the photoelectron beam from inelastic scattering.

To obtain the curves denoted by diamonds in figure 7.15 we multiply the $X\alpha$ EXAFS spectra with the energy-dependent loss factors calculated in this chapter and by a mean free path term, $exp\Big(-2(r_j - r_o)V_{PI}/k\Big)$, where $r_j = 2.541\mathring{A}$ is the

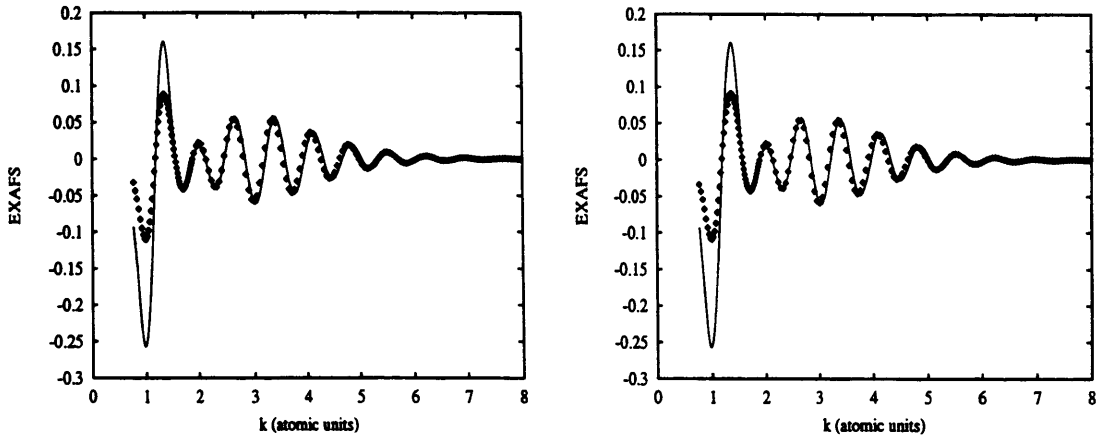

Figure 7.15: Unweighted EXAFS spectra for copper foil. The solid curve gives the result calculated with the Daresbury program EXCURV98 using the Hedin-Lundqvist exchange potential. The two sets of points are the spectra obtained using the real $X\alpha$ potential in EXCURV98 multiplied by the two types of loss factors investigated in this chapter. The curve on the left is with a loss factor calculated using a model energy dependence and normalised to the sudden approximation whilst the graph on the right is with a result calculated using a screened core hole.

nearest neighbour distance, $r_o = 1.27\mathring{A}$ is the central atom muffin tin radius and $V_{PI} = 4eV$. The curve on the left shows the spectra obtained with a loss factor given by equation (7.16) normalised to a sudden limit of 0.67. The curve on the right shows the spectra calculated using the screened core hole loss factor. Both loss factors seem to give a reasonable description of the losses, both significantly improve the fit from that obtained with the $X\alpha$ potential alone and both factors are considerably better than the constant s_o^2 and V_{PI} loss factors used historically.

Because the spectra are slightly out of phase it is not particularly instructive to give an R-factor value for the comparison of the various theories. However, both the model energy dependence curves give an R-factor of around 42%. This is much better than the R-factor obtained by comparing the curve calculated with the HL potential to that calculated with the $X\alpha$ potential and a constant loss factor, $s_o^2 exp(2r_j V_{PI}/k)$, of $R = 64\%$.

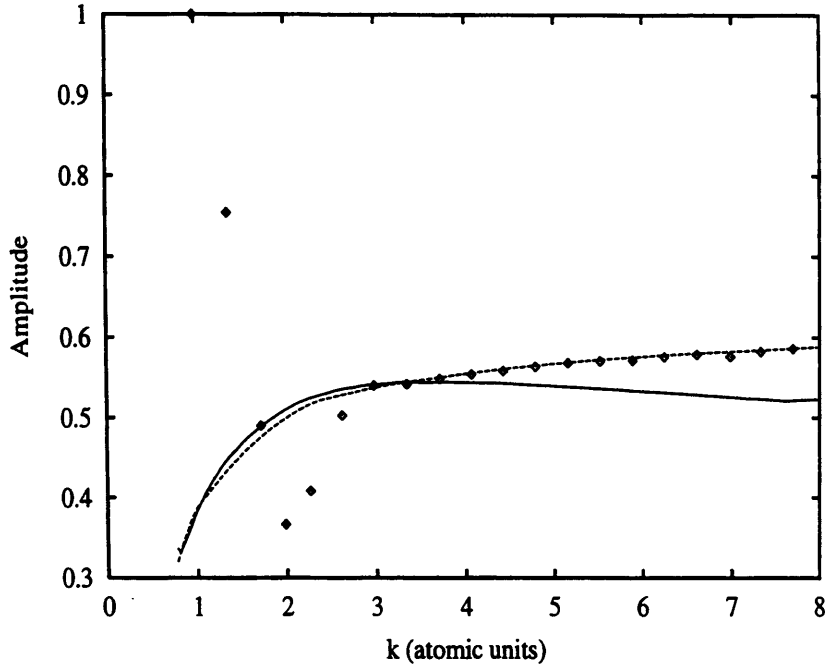

Figure 7.16: EXAFS loss factors. The points are obtained by ratioing the EXAFS peak heights calculated using the HL potential which empirically includes all the losses and the $X\alpha$ potential which includes none. The solid line is the loss factor calculated using the screened core hole whilst the dotted line is the loss factor calculated with a model energy dependence normalised to a sudden limit of 0.67.

In figure 7.16 we compare the loss factors directly. To obtain the data points we have ratioed the peak heights of the EXAFS spectra calculated with the HL potential to the equivalent peak heights of the spectra calculated with the $X\alpha$ potential. The dotted line shows the result of the model energy dependence calculation normalised to a sudden limit of 0.67 whilst the solid line shows the result for the loss factor calculated using the screened core hole. Both loss factors have been multiplied by the appropriate mean free path term to describe the losses outside of the central muffin tin.

Within the range of an EXAFS spectra the model energy dependence calculation gives excellent agreement with the losses obtained using the HL potential, with much less computational effort. The screened core hole also gives

reasonable results although the energy dependence is not quite correct. The energy dependence of both the loss factors is unphysical at small k because of the constant value for V_{PI} used in the mean free path term. This completely kills the EXAFS at very small k. To model the mean free path term more accurately we need an energy-dependent V_{PI}, the simplest form being one which simply cuts off at the binding energy of the most weakly bound state. Below this energy, no inelastic scattering is possible and thus we obtain no losses to the EXAFS.

7.3 Conclusion

In this chapter we have used time-dependent perturbation theory and a model core hole - photoelectron potential, $V(r)$, to obtain results for the secondary electron shake-off probabilities as a function of photon energy above the X-ray absorption edge.

Initially we follow the procedure of Thomas [20]. We model the energy dependence of the radial matrix element involving $V(r)$ and set its magnitude using the high energy limit for the shake-off probabilities which may be calculated using the sudden approximation (see chapter 6) or taken from experiment. We extend Thomas' model to correctly obtain the probabilities for secondary electron shake-off rather than shake-up by including the possibility of transitions into all energetically available continuum states. This method gives results for the shake-off probabilities which compare very well with experimental data for neon and argon. This method can also be used to generate an energy-dependent loss factor applicable to EXAFS calculations which use a real scattering potential. The results obtained using the $X\alpha$ potential and the energy-dependent loss factor agree extremely well with those obtained using the complex HL potential which is known to give good agreement to experiment.

In a further extension to Thomas' theory we model V(r) explicitly. We choose a form for the potential which starts at zero at small times and tends to a screened $\frac{1}{r}$ potential once the primary photoelectron has departed from the atom. We found that the results obtained were fairly dependent on the form of screening used. However, an SPP dielectric function used within the local density approximation gave results which agree reasonably well with experiment. The energy dependence of the shake-off probabilities is, however, not quite correct. The dielectric function used appears to underestimate the screening at high photoelectron energies, although the magnitudes obtained are generally within the experimental error over the region of energy of interest in EXAFS. This method gives double electron absorption cross sections which are as good as those produced using the configuration interaction method. However, the secondary electron excitation spectra produced using the screened core hole are, at best, acceptable, the energy dependence of the spectra being incorrect. This method does, however, show promise, and it may be that calculations with a better form for the dielectric function or more accurate final state wavefunctions would greatly improve the results. Again, using this method to generate an energy dependent loss factor for EXAFS calculations would appear to give results as good as those obtained with HL potential.

In summary we have investigated two methods which give reasonable results for the energy dependence and magnitude of the secondary electron shake-off probabilities. Both methods can be used to generate energy-dependent loss factors which may be used in real potential EXAFS scattering codes to give good agreement with the experimental EXAFS.

Chapter 8

Summary and Conclusions

In this thesis we have investigated some of the many-electron effects which affect the X-ray absorption fine structure or EXAFS. EXAFS is an important experimental technique of particular use for the study of the structure of non-crystalline materials. Data analysis of the EXAFS is generally performed by comparing the experimental spectra to spectra calculated theoretically using plausible model structures. To date the theory has been developed using a wholly single electron formalism with the many-body effects, which are not well understood, typically lumped into various empirical parameters and scattering potentials. These many-electron effects are, however, important. In particular they have a large effect on the EXAFS amplitude which greatly affects the experimental determination of coordination numbers. Typically, the EXAFS technique cannot determine coordination numbers to an accuracy of better than $\pm 10\%$.

In this thesis we investigate some of the approximations used to describe many-electron effects in EXAFS data analysis programs. The Daresbury program EXCURV98 [14] uses a complex exchange and correlation potential to model the many-electron effects. The imaginary part of this potential models the extrinsic inelastic losses to the EXAFS. It therefore reduces the EXAFS amplitude. In

chapter 2 we develop approximations which allow us to calculate the amplitude of the EXAFS in the presence of a complex scattering potential without calculating the EXAFS itself. This allows us to study the effect of the imaginary potential on the theoretical amplitudes without having to consider the other changes to the EXAFS spectra caused by the complex potential.

The exchange and correlation potential most commonly used today is the Hedin-Lundqvist [9] potential which is derived from the GW formalism using uniform electron gas relations and the local density approximation. This potential lumps all of the inelastic scatterings into collective excitations, the plasmons, without explicitly mentioning the single electron transitions. The HL potential neglects single electron excitations because it is calculated using an approximate form of the inverse dielectric function, the single plasmon pole form [9]. In chapter 3 we examine the SPP dielectric function and compare it to a full atomic calculation of $\epsilon^{-1}(q,\omega)$. To our knowledge this is the first such calculation of an atomic ϵ^{-1}. The two forms show similar overall energy and q dependence. The SPP dielectric function, however, does not exhibit the sharp structure of the atomic calculation at the X-ray absorption edges because of its neglect of the single electron excitations.

In chapter 4 we use the SPP dielectric function to calculate the HL potential. The effects of the imaginary part of this potential on the EXAFS amplitudes are then examined using the formulae derived in chapter 2. We find that the HL potential significantly overestimates the extrinsic EXAFS losses. It gives values for the mean free path which are much shorter than those observed experimentally. Instead the amplitudes given by the HL potential agree well with the total (extrinsic plus intrinsic) losses to the EXAFS. Additional amplitude fitting parameters should therefore not be used when data fitting with the HL potential. This is an important result. Previously it had been assumed that the

HL potential gave a good approximation to the extrinsic losses, thus, values of the amplitude reduction factor of 0.6 to 0.8 were considered reasonable when data analysing using this potential. Using such low values, however, would lead to erroneous results for the Debye-Waller factor and for the coordination numbers. This has now mostly been acknowledged amongst the UK EXAFS community, the default value of the constant amplitude fitting parameter, AFAC (s_o^2), in EXCURV has been changed from 0.8 in the 1992 release to 1.0 in the current version.

In chapter 5 we develop the work of Beni, Lee and Platzman [17] who produced a complex scattering potential which explicitly includes single electron excitations. BLP derive their potential from a consideration of the atomic scattering factor. In chapter 5 we show that this potential may also be obtained from the GW approximation by making the relevant approximations. We derive a method by which we may solve for the BLP potential without using the many approximations applied by BLP. However, we find that the imaginary part of the potential is much larger than the imaginary part of the HL potential and therefore vastly overestimates the inelastic scatterings. We find that the magnitude of the potential is critically dependent on the phase-shifts and hence the potential itself. A proper calculation of the BLP potential would require a self-consistent procedure taking many iterations. However, such a procedure is not practical for EXAFS data analysis purposes where computer time must be kept to a minimum. We therefore conclude that this potential is unsuitable for EXAFS purposes.

In chapter 6 we change tack somewhat and examine the intrinsic losses to the EXAFS. In this chapter we discuss the problem in terms of the sudden approximation which is valid in the limit of high photoelectron energy. By describing the appearance of the core hole using Slater's rules [19] we may easily calculate the effects on the EXAFS amplitudes in this limit for all edges of

all elements, the first time that this has been done. We find that, using this simple model with numerical values for the effective nuclear charge tabulated by Clementi *et al* [26], we obtain surprisingly good agreement with experiment. The method can also be used to calculate the probability of excitation into the continuum and the probability of transitions into excited bound states which we find to be small. In this chapter we also calculate the amplitude reduction factor using tight binding initial state wavefunctions. In the worst possible case this calculation gives results which differ at most by $\pm 10\%$ from the free atom calculation of s_o^2. We therefore conclude that the amplitude reduction factor is independent of the chemical environment of the absorbing atom.

Chapter 7 is concerned with a time-dependent model of the core hole - photoelectron system. We take a simple model form for the time dependence of the potential of the core hole and photoelectron and use it to calculate results for the secondary electron shake-off probabilities. The time-dependent form of the potential comes from Thomas [20] who calculated the neon shake-off spectra by normalising his results to the experimental high energy limit. Thomas' theory is, however, incorrect. We correct the theory of Thomas and calculate shake-off spectra for neon, and argon K and L edges either by normalising to experiment or to the calculated results of chapter 6. The calculations are compared to experiment and are found to agree well. We also describe a more complex model of the core hole - photoelectron system in which we explicitly include the screening of the core hole by using the SPP dielectric function. This calculation gives less good results than the simpler model used but is at least as good as the many-body perturbation theory models which have been used previously [68, 69]. The results obtained for the shake-off spectra can be used to calculate the total (intrinsic+extrinsic) losses to the EXAFS. The total EXAFS losses appear to agree well with experiment thus, this method could be used with an entirely real

scattering potential in an EXAFS data analysis program. Chou *et al* [51] state that the Dirac-Hara potential (a real scattering potential) gives better final state phase-shifts than the HL potential. Also, data analysis programs with complex potentials are difficult to produce, especially where multiple scattering must be taken into account. Using the methods described in this chapter it would be relatively simple to produce an EXAFS data analysis program using the Dirac-Hara potential but which also adequately describes the inelastic losses. In such a program the energy dependent loss factors calculated in this Chapter could be input for each element in parameterised form. In most data analysis programs the intrinsic losses are approximated by a constant or are included in an *ad hoc* manner by the use of the HL potential. The method described in chapter 7, however, does not suffer from this drawback, and would also be of use to groups who do not readily have access to such codes as EXCURV98.

A possible future work stemming from this thesis would, of course, be to produce such a multiple scattering EXAFS program using the methods described above. This program could then be tested fully against the presently available codes. Also, other interesting results have been produced in this thesis. Namely, whilst being good enough at present, the approximations made to describe many-body effects in EXAFS are not accurate. Restrictions, largely due to the lack of available computing power mean that we cannot do much better than the HL or other similar potentials. However, improvements could be made to the results reported in this thesis by using fully self-consistent calculations and including higher order terms in the perturbation theories. A further study along these lines might produce results of interest for their own sake.

APPENDIX A

The Real Part Of The Hedin-Lundqvist Potential

In Chapter 4, equation (4.12), the real part of the Hedin-Lundqvist potential was defined in terms of 3 coefficients. I_1, I_2 and I_3 are the results of the angular integrals in equation (4.10). These are listed below.

$$I_1 = \frac{E_f - E_i}{k} \log\left|\frac{k + k_f}{k - k_f}\right| + k_f \tag{A.1}$$

$$I_2 = \frac{1}{kq_c^2} \log\left|1 - \frac{q_c}{k}\right| - \frac{1}{k^3} \log\left|1 + \frac{k}{q_c}\right| + \frac{1}{k^2 q_c} \tag{A.2}$$

$$\begin{aligned}
I_3 \;=\; & \frac{1}{k^2}\left\{\frac{1}{q_{min}} - \frac{1}{q_c} - \frac{1}{q_{max}}\right\} + \frac{1}{kq_{max}^2} \log\left|1 - \frac{q_{max}}{k}\right| + \frac{1}{kq_c^2} \log\left|1 - \frac{q_c}{k}\right| \\
& + \frac{1}{k^3} \log\left|\frac{q_c(q_{min} - k)q_{max}}{q_{min}(q_c - k)(q_{max} - k)}\right| \\
& - \frac{1}{kq_{min}^2} \log\left|\frac{(k - q_{min})(q_{min}^2 - 2E_f + 2E_i)}{k(q_{min}^2 + 2E_f - 2E_i}\right| \\
& + \frac{1}{2E_f - 2E_i} \log\left|\frac{q_{min}^4(q_{max}^2 - 2E_f + 2E_i)(q_{max}^2 + 2E_f - 2E_i)}{q_{max}^4(q_{min}^2 - 2E_f + 2E_i)(q_{min}^2 + 2E_f - 2E_i)}\right| \\
& - \frac{1}{kq_{max}^2} \log\left|\frac{q_{max}^2 - 2E_f + 2E_i}{q_{max}^2 + 2E_f - 2E_i}\right| \qquad q_c < q_{min} \\
= \; & \frac{1}{k^2 q_{max}} - \frac{1}{k^3} \log\left|1 + \frac{1}{q_{max}}\right| + \frac{1}{kq_c^2} \log\left|\frac{q_c^2 - 2E_f + 2E_i}{q_c^2 + 2E_f - 2E_i}\right| \\
& + \frac{1}{2E_f - 2E_i}\left\{\log\left|\frac{q_{max}^2 - 2E_f - 2E_i}{q_{min}^2 - 2E_f - 2E_i}\right| + \log\left|\frac{q_{max}^2 + 2E_f - 2E_i}{q_c^2 + 2E_f - 2E_i}\right|\right\}
\end{aligned}$$

$$+\frac{2}{E_f - E_i}\log\left|\frac{q_c}{q_{max}}\right| \qquad q_{min} < q_c < q_{max}$$

$$= \frac{1}{kq_c^2}\log\left|1 - \frac{q_c}{k} - \frac{1}{k^3}\right| \log\left|1 - \frac{k}{q_c}\right| - \frac{1}{k^2 q_c} \qquad q_c > q_{max} \qquad \text{(A.3)}$$

APPENDIX B

Derivation of the Beni, Lee and Platzman Polarisation Potential from the Atomic Scattering Factor

In Chapter 5 we briefly discussed how Beni, Lee and Platzman (BLP) obtained their form for the complex correlation potential. In this appendix we outline the method in more detail.

BLP [17] define their form for the potential as the Fourier transform of the atomic scattering factor, $f(\eta)$. The scattering factor, summed to all orders of scattering, may be written in terms of the exact many body wavefunctions of the system and the interaction potential seen by the photoelectron,

$$f = -\frac{1}{2\pi}\langle \Psi_I \,|\, V_{int} \,|\, \Psi_F \rangle, \tag{B.1}$$

where Ψ_I is a many body state with the photoelectron far from the atom and the atomic electrons unperturbed, and Ψ_F is the many body final state describing the atomic electrons and the scattered photoelectron far from the atom. As we are interested only in the elastic scattering, Ψ_F must have all of the bound electrons in their initial atomic states.

V_{int}, the potential seen by the photoelectron, is given by,

$$V_{int} = -\frac{Z}{r} + \sum_i \frac{1}{|\mathbf{r} - \mathbf{r}_i|}, \tag{B.2}$$

where Z is the atomic number and the summation is over all electronic coordinates.

Equation (B.1) may also be expressed in the first Born approximation in terms of an effective scattering potential,

$$f(\boldsymbol{\eta}) = -\frac{1}{2\pi}\langle \varphi_{\mathbf{k}_i} | V_{eff} | \varphi_{\mathbf{k}_f} \rangle. \tag{B.3}$$

Equation (B.3) describes the scattering by an atom of some incident electron from wavevector $\mathbf{k}_i$ to $\mathbf{k}_f$ where the momentum transfer, $\mathbf{k}_f - \mathbf{k}_i$, is given by $\boldsymbol{\eta}$ and $\varphi_{\mathbf{k}_i}$ and $\varphi_{\mathbf{k}_f}$ are plane waves.

To obtain the BLP result we must neglect the exchange between electrons in equation (B.1) so that Ψ_I and Ψ_F become Hartree products of the photoelectron and bound state wavefunctions. We take the photoelectron initial state to be a plane wave and obtain the many electron final state using a Green function expansion.

$$\Psi_F = \Psi_K + G V_{int} \Psi_K. \tag{B.4}$$

Ψ_K is the product of all the bound atomic states and a plane wave final state of wavevector, $\mathbf{k}_f$, and the Greens function is defined as,

$$G = \sum_N \frac{\Psi_N \Psi_N^*}{E - E_N \pm \imath\delta}, \tag{B.5}$$

where Ψ_N are the Hartree wavefunctions for all of the excited states available to the system. Within the Hartree approximation only those states with at most a single excited electron are obtainable. E_N is the energy of the many electron state, Ψ_N, and $E = E_I + \frac{1}{2}k_i^2$ is the sum of the initial photoelectron energy and the energies of all the bound state electrons in the system.

Substituting for Ψ_F into equation (B.1) we have that,

$$\begin{aligned} f(\boldsymbol{\eta}) &= -\frac{1}{2\pi}\left\{\langle\Psi_I\,|\,V_{int}\,|\,\Psi_K\rangle + \sum_N \frac{\langle\Psi_I\,|\,V_{int}\,|\,\Psi_N\rangle\langle\Psi_N\,|\,V_{int}\,|\,\Psi_K\rangle}{E - E_N \pm \imath\delta}\right\} \\ &= f_1 + f_2. \end{aligned} \tag{B.6}$$

As Ψ_I is simply a product of bound atomic orbitals, $\phi_o(r_i)$, and a free electron wave, we can see that the first term in equation (B.6) is simply the Fourier transform of the Hartree potential,

$$f_1(\boldsymbol{\eta}) = -\frac{1}{2\pi}\int e^{-\imath\boldsymbol{\eta}\cdot\mathbf{r}}\left(-\frac{Z}{r} + \sum_i \int \frac{\phi_o^*(r_i)\phi_o(r_i)}{|\mathbf{r}-\mathbf{r}_i|}d\mathbf{r}_i\right)d\mathbf{r}. \tag{B.7}$$

The second term in equation (B.6) must therefore be the Fourier transform of the correction to the Hartree potential. This correction term is the polarisation potential.

In evaluating f_2 we write the excited, intermediate, state wavefunction as,

$$\Psi_N = e^{\imath(\mathbf{k}_i+\mathbf{q})\cdot\mathbf{r}}\prod_{j\neq i}\phi_j(r_j)\psi_n(r_i). \tag{B.8}$$

Within the Hartree approximation, we may choose a particular electron to be excited from a bound atomic orbital, $\phi_o(r_i)$, into an excited continuum state, $\psi_n(r_i)$. The photoelectron is excited into the intermediate state, $\exp(\imath(\mathbf{k}_i+\mathbf{q})\cdot\mathbf{r})$, thus the energy of the many electron wavefunction, Ψ_N, is given by,

$$E_N = E_I - \omega_o + \omega_n + \frac{1}{2}\,|\mathbf{k}_i+\mathbf{q}|^2, \tag{B.9}$$

where ω_o and ω_n are the energies of the single electron bound and excited states.

The integrals over the photoelectron radial coordinate are simply Fourier transforms of the $1/r$ potentials. These may be easily evaluated. Then, to obtain the BLP result for the scattering factor we must finally integrate over all the possible intermediate photoelectron states available for each of the $\psi_n(r)$ excited

atomic states.

$$f_2(\boldsymbol{\eta}) = -\frac{1}{(2\pi)^3}\sum_n \int d\mathbf{q} \frac{8\pi \langle \phi_o | e^{\imath \mathbf{q}\cdot\mathbf{r}} | \psi_n \rangle \langle \psi_n | e^{\imath(\boldsymbol{\eta}-\mathbf{q})\cdot\mathbf{r}} | \phi_o \rangle}{q^2 \, |\boldsymbol{\eta}-\mathbf{q}|^2 \, (E - E_N + \imath\delta)}$$

$$= \frac{1}{2\pi^2}\sum_n \int d\mathbf{q} \frac{\langle \phi_o | e^{\imath \mathbf{q}\cdot\mathbf{r}} | \psi_n \rangle \langle \psi_n | e^{\imath(\boldsymbol{\eta}-\mathbf{q})\cdot\mathbf{r}} | \phi_o \rangle}{q^2 \, |\boldsymbol{\eta}-\mathbf{q}|^2 \, (q^2 + 2\mathbf{q}\cdot\mathbf{k}_i + 2(\omega_n - \omega_o) - \imath\delta)}, \quad \text{(B.10)}$$

where we have taken the $+\imath\delta$ term in the denominator of the Green function as the excited states $\psi_n(r)$ must be unoccupied.

Equation (B.10) is identical to the result for the second Born approximation to the atomic scattering factor given by BLP. f_2 is just the Fourier transform of an effective scattering potential which may be added to the Hartree potential to give an approximation to the electron-electron correlation.

APPENDIX C

Calculation of a_n using a Different q Dependent Plasmon Frequency.

In chapter 7 we calculated the probability, $P(\omega)$, of exciting two electrons into the continuum following the absorption of an X-ray photon. The results obtained were strongly dependent on the form of the screening used. In Chapter 7 we calculated $P_(\omega)$ using a single plasmon pole dielectric function (eqn.(7.20)) with a simplified q dependent plasmon frequency of, $\omega_q^2 = \omega_p^2(r) + \frac{1}{4}q^4$. We can also calculate the relevant excitation probabilities using a less accurate form of the q dependent excitation frequency,

$$\omega_q = \omega_p(r) + \frac{1}{2}q^2. \tag{C.1}$$

This form of the plasmon frequency has identical large and small q limits to the q^4 plasmon frequency defined above.

The probability of secondary electron excitation is defined in terms of the expansion coefficients of the perturbed system wavefunctions. We have,

$$a_n = \frac{\imath}{(2\pi^3)} \left\langle \psi_n \left| \int d\mathbf{q} e^{\imath \mathbf{q}\cdot\mathbf{r}} V(q, -\omega_{no}) \epsilon^{-1}(q, -\omega_{no}) \right| \phi_{l_o} \right\rangle \tag{C.2}$$

Using equation (C.1) for the q dependent plasmon frequency we can, once again, evaluate the q integral in equation (C.2) directly with the help of Gradsteyn and

Ryzhik [54]. We find,

$$\begin{aligned} a_n &= \frac{it_o^{-1}}{\omega_{no}(\omega_{no}+it_o^{-1})}\left\langle \psi_n \left| \frac{1}{r} + \frac{\omega_p^2}{r\omega_{no}}\left[\frac{1}{a^2}\left(1-cos(ar)\right)+\frac{1}{b^2}\left(1-e^{-br}\right)\right]\right| \phi_o \right\rangle \\ &\quad \omega_{no} > \omega_p(r) \\ &= \frac{it_o^{-1}}{\omega_{no}(\omega_{no}+it_o^{-1})}\left\langle \psi_n \left| \frac{1}{r} + \frac{\omega_p^2}{r\omega_{no}}\left[\frac{1}{a^2}\left(1-e^{-ar}\right)+\frac{1}{b^2}\left(1-e^{-br}\right)\right]\right| \phi_o \right\rangle \\ &\quad \omega_{no} < \omega_p(r) \end{aligned} \tag{C.3}$$

where,

$$\begin{aligned} a^2 &= 2|\omega_{no}-\omega_p| \qquad \text{and,} \\ b^2 &= 2(\omega_{no}+\omega_p). \end{aligned} \tag{C.4}$$

The r integrand contains a divergence at $\omega_{no} = \omega_p(r)$. This may be dealt using a Romberg integration routine in the same way as the r integral in Chapter 7.

Bibliography

[1] R deL. Kronig, Z. Phys. **70** (1931) 317-323.

[2] D E Sayers, E A Stern and F W Lytle, Phys. Rev. Lett. **27** (1971) 1204-1207.

[3] E A Stern, Phys. Rev. B **10** (1974), 3027-3037.

[4] P A Lee and J B Pendry, Phys. Rev. B **11** (1975) 2785-2811.

[5] J J Rehr, R C Albers, submitted to, Reviews of Modern Physics.

[6] S J Gurman and R F Pettifer, Philos. Mag. B **40** (1979) 345-349.

[7] H A Bethe, R Jackiw, 'Intermediate Quantum Mechanics', (The Benjamin/Cummings Publishing Company (1986)).

[8] J B Pendry, 'Low Energy Electron Diffraction', (Academic Press, London (1974)).

[9] L Hedin and S Lundqvist, Solid State Physics, **23** (1969) 2-181.

[10] P A Lee and G Beni, Phys. Rev. B **15** (1976) 2862-2883.

[11] T A Carlson, C W Nestor, T C Tucker and F B Malik Phys. Rev. **169** (1968) 27-36.

[12] S S Hasnain (ed) 'Synchrotron Radiation and Biophysics' (Ellis Horwood, Chichester (1990)).

[13] T M Hayes and J B Boyce, Solid State Physics, **37** (1982) 173-351.

[14] N Binsted, EXCURV98: CCLRC Daresbury Laboratory computer program (1998).

[15] W Bardyszewski and L Hedin, Physica Scripta **32** (1985) 439-450.

[16] J F Hart, Ph.D. Thesis, Leicester University (1997).

[17] G Beni, P A Lee, and P M Platzman, Phys. Rev. B, **13** (1976) 5170-5178.

[18] L J Schiff, 'Quantum Mechanics' 3rd edn. (McGraw-Hill, London (1968)).

[19] J C Slater, Phys. Rev **36** (1930) 57-64.

[20] T D Thomas, Phys. Rev. Letters, **52** (1984) 417-420.

[21] C A Ashley and S Doniach, Phys. Rev. B **11** (1975) 1279-1288.

[22] S J Gurman, N Binsted, and I Ross, J. Phys. C **17** (1984) 143-151.

[23] S J Gurman, N Binsted and I Ross, J. Phys. C **19** (1986) 1845-1861.

[24] T L Loucks, 'Augmented Plane Wave Method', (W.A Benjamin inc., New York (1967)).

[25] T A Tyson, Ph.D. Thesis, Stanford University (1991).

[26] E Clementi and C Roetti, Atomic Data and Nuclear Data Tables **14** (1974) 177-478.

[27] A D McLean and R S McLean, Atomic Data and Nuclear Data Tables **26** (1981) 197-381.

[28] 'Handbook of Chemistry and Physics', (The Chemical Rubber Company, Cleveland (1970)).

[29] D M Brink and G R Satchler, 'Angular Momentum', (Clarendon Press : Oxford (1968)).

[30] A Messiah, 'Quantum Mechanics', vol. 1, (North Holland Publishing Company, Amsterdam (1961)).

[31] M Abramowitz and I A Stegun, 'Handbook of Mathematical Functions', (Dover Publications, inc., New York (1965)).

[32] See for example S J Gurman, J. Phys. C:Solid State Phys., **16** (1983), 2987-3000.

[33] M Roy and S J Gurman, J. Synchrotron Rad. **6** (1999) 228-230.

[34] A Szabo and N S Ostlund, 'Modern Quantum Chemistry: Introduction To Advanced Electronic Structure Theory', (MacMillan Publishing Co., inc. New York (1982)).

[35] F Aryasetiawan and O Gunnarson, Rep. Prog. Phys **61** (1998) 237-312.

[36] J C Slater and K H Johnson, Phys. Rev. B **5** (1972) 844-853.

[37] L Hedin, Phys. Rev. A **139** (1965) 796-823.

[38] J C Inkson, 'Many-Body Theory Of Solids. An Introduction' , (Plenum Press. New York and London. (1984)).

[39] W Jones and N H March, 'Theoretical Solid State Physics' , Volume 1, (Dover Publications, Inc. New York (1973)).

[40] D Pines, 'Elementary Excitations in Solids', (W A Benjamin, inc. New York (1964)).

[41] J M Ziman, 'Elements of Advanced Quantum Theory', (Cambridge University Press (1969)).

[42] P Nozieres, 'Theory of Interacting Fermi Systems', (W A Benjamin, inc. New York (1964)).

[43] J Lindhard kgl. Danske Videnskab, Selskab. Mat-fys, medd., **28** (1954) 8.

[44] K Schwarz, Phys. Rev. B **5** (1972) 2466-2468.

[45] W M J Veigele, Atomic Data Tables **5** (1973) 51-111.

[46] A Owens, S C Bayliss, P J Durham, S J Gurman, and G W Fraser, Astrophysical Journal **468** (1996) 451-454.

[47] J Mustre de Leon, J J Rehr, S I Zabinsky and R C Albers, Phys. Rev. B **44** (1991) 4146-4156.

[48] P A M Dirac, Proc. Cambridge Philos. Soc. **26** (1930) 376-385.

[49] S Hara, J. Phys. Soc. Japan **26** (1967) 376.

[50] M S Woolfson, S J Gurman and B W Holland, Surface Science **117** (1982) 450-458.

[51] S H Chou, J J Rehr, E A Stern and E R Davidson, Phys. Rev. B **35** (1987) 2604-2614.

[52] S J Gurman, private communication.

[53] D R Penn, Phys. Rev. B **35** (1987) 482-486.

[54] I S Gradsteyn and I M Ryzhik, 'Tables of Integrals, Series and Products', (Academic Press, New York and London (1965)).

[55] W Magnus F Oberhettinger and R P Soni, 'Formulas and Theorems for the Special Functions of Mathematical Physics', (Springer-Verlag Berlin, Heidelberg, New York (1966)).

[56] W A Harrison, 'Solid State Theory', (Tata McGraw-Hill Publishing Company (1970)).

[57] T Aberg, Phys. Rev. **156** (1967) 35-41.

[58] T A Carlson and M O Krause, Phys. Rev. **149** (1965) A1057-A1064.

[59] K G Dyall, J. Phys. B **16** (1983) 3137-3147.

[60] B K Teo 'EXAFS: Basic Principles and Data Analysis', (Springer-Verlag Berlin Heidelberg New York Tokyo (1986)).

[61] J J Rehr, E A Stern, R L Martin, E A Davidson, Phys. Rev. B **17** (1978) 560-565.

[62] G van Dorssen, private communication.

[63] J S Blakemore, 'Solid State Physics', (Cambridge University Press (1985)).

[64] N W Ashcroft and N D Mermin, 'Solid State Physics', (Saunders College (1966)).

[65] K Zhang, E A Stern, J J Rehr and F Ellis, Phys. Rev. B **44** (1991) 2030-2039.

[66] S J Schaphorst, A F Kodre, J R Rusheinski, B Crasemann, T Aberg, J T Tulkki, M H Chen, Y Azuma, and G S Brown, Phys. Rev A **47** (1993) 1953-1966.

[67] T A Carlson, Phys. Rev. **156** (1967) 142-149.

[68] T N Chang and R T Poe, Phys. Rev. A **12** (1975) 1432-1439.

[69] S L Carter and H P Kelly, Phys. Rev. A **16** (1977) 1525-1534.

[70] J W Gadzuk and M Sunjic, Phys. Rev. B **12** (1972) 524-530.

[71] E Vatai, Phys. Rev. A **38** (1988) 3777-3780.

[72] C Noguera and D Spanjaard, J. Phys. F **11** (1981) 1133-1149.

[73] D Lu and J J Rehr, Phys. Rev. B **37** (1988) 6126-6133.

[74] J Stohr, R Jaeger, and J J Rehr, Phys. Rev. Letters **51** (1983) 821-824.

[75] W H Press, B P Flannery, S A Teukolsky and W T Vetterling, 'Numerical Recipes, The Art of Scientific Computing', (Cambridge University Press (1989)).

[76] M Deutsch and M Hart, Phys. Rev. Letts. **57** (1986) 1566-1569.

[77] R J Bartlett, P J Walsh, Z X He, Y Chung, E M Lee and J A R Samson, Phys. Rev. A **46** (1992) 5574-5579.

[78] J A R Samson, R J Bartlett, and Z X He, Phys. Rev. A **46** (1992) 7277-7280.

[79] D M P Holland, K Codling, J B West and G V Marr, J. Phys. B **12** (1979) 2465-2484.

[80] G R Wight and M J Van der Viel, J. Phys. B **9** (1976) 1319-1327.

[81] U Becker, R Wehlitz, O Hemmers, B Langer and A Menzel, Phys. Rev. Letters **63** (1989) 1054-1057.

[82] G B Armen, T Aberg, Kh R Karim, J C Levin, B Crasemann, G S Brown, M H Chen and G E Ice, Phys. Rev. Letters **54** (1985) 182-185.

[83] A Kodre, J P Gomilsek, I Arcon, and R Preseren, J. Synchrotron Rad. **6** (1999) 306-307.

[84] A Filipponi, Physica B **208 & 209**, (1995) 29-32.

[85] E A Stern, S M Heald and B Bunker, Phys. Rev. Letts. **42** (1979) 1372-1375.